Image Quality of Digital Breast Tomosynthesis: Optimization in Image Acquisition and Reconstruction

by

Gang Wu

A thesis submitted in conformity with the requirements
for the degree of Doctor of Philosophy
Graduate Department of Medical Biophysics
University of Toronto

Abstract

Image Quality of Digital Breast Tomosynthesis: Optimization in Image Acquisition and Reconstruction

Gang Wu
Doctor of Philosophy
Graduate Department of Medical Biophysics
University of Toronto
2014

Breast cancer continues to be the most frequently diagnosed cancer in Canadian women. Currently, mammography is the clinically accepted best modality for breast cancer detection and the regular use of screening has been shown to contribute to reduced mortality. However, mammography suffers from several drawbacks which limit its sensitivity and specificity. As a potential solution, digital breast tomosynthesis (DBT) uses a limited number (typically 10–20) of low-dose x-ray projections to produce a three-dimensional tomographic representation of the breast. The reconstruction of DBT images is challenged by such incomplete sampling. The purpose of this thesis is to evaluate the effect of image acquisition parameters on image quality of DBT for various reconstruction techniques and to optimize these, with three specific goals: A) Develop a better power spectrum estimator for detectability calculation as a task-based image quality index; B) Develop a paired-view algorithm for artifact removal in DBT reconstruction; and C) Increase dose efficiency in DBT by reducing random noise.

A better power spectrum estimator was developed using a multitaper technique, which yields reduced bias and variance in estimation compared to the conventional moving average method. This gives us an improved detectability measurement with finer frequency steps. The paired-view scheme in DBT reconstruction provides better image quality than the commonly used sequential method. A simple ordering like the "side-to-side" method can achieve less artifact and higher image quality in reconstructed slices. The new denoising algorithm developed was applied to the projection views acquired in DBT before reconstruction. The random noise was markedly removed while the anatomic details were maintained. With the help of this artifact-removal technique used in reconstruction and the denoising method employed on the projection views, the image quality of DBT is enhanced and lesions should be more readily detectable.

Dedication

I dedicate this thesis to my parents
for their constant support and unconditional love.
I love you dearly.

Acknowledgements

I would like to thank the following people who helped, encouraged and supported me throughout my Ph.D. degree:

- My supervisor Dr. Martin Yaffe and members of my supervisory committee Dr. Anne Martel, Dr. Simon Graham and Dr. James Mainprize. Thanks for your guidance, patience and great help all these years;
- Colleagues in Dr. Yaffe's group, especially those who work on tomosynthesis, Gord Mawdsley, Aili Bloomquist, Sam Shen, Cindy Xinying Wang and Albert Tyson who give me valuable suggestions and spark new ideas in many discussions;
- My fellow graduate students Melissa Hill and Olivier Alonzo-Proulx for their help, support and useful discussions;
- All members of the Yaffe lab, past and present, who have been great colleagues and friends;
- My appreciation also goes to many scholars and friends working in Sunnybrook, Dr. Sam Shen, Dr. Wen Shi, Dr. Peizhu Sun, and Dr. Jianhua Yin. Thank you for imparting wisdoms on me, about living, loving and learning;
- Finally, I am grateful for my friends and family and I want to thank them for their continued love and support.

Contents

List of Tables

List of Figures

Glossary

2D two dimension. 1, 5, 8, 17, 29, 47

3D three dimension. 1, 4–6, 29, 47–49

ART algebraic reconstruction technique. 6, 30

ASF artifact spread function. 29, 30, 37–39, 41

CC cranial-caudal. 4

CT computerized tomography. 6, 30

DBT digital breast tomosynthesis. 10, 30, 32, 34, 35, 42, 49–51, 53, 55, 56, 65, 66, 68, 70

DCIS ductal cancer in situ. 2

del detector element. 8

DQE detective quantum efficiency. 8, 9, 11

ESF edge spread function. 8

FBP filtered backprojection. 6, 30

FFT Fast Fourier Transform. 12, 13

FOM figure of merit. 30, 37, 41, 51

FWHM full-width-half-maximum. 12, 22, 59, 61

IDC infiltrating ductal cancer. 2, 31, 50, 68

LCIS lobular cancer in situ. 2

LSAMTM local spectral adaptive multitaper method. 58–61, 63, 65

LSF line spread function. 8

MB minimum bias. 14

ML maximum likelihood. 6, 29, 30, 34, 35, 38, 39, 41, 42, 47

ML-EM maximum likelihood expectation maximization. 6

MLC maximum likelihood convex. 6

MLO mediolateral oblique. 4

MLPV maximum likelihood with paired views. 39, 41, 42, 47, 51

MRI magnetic resonance imaging. 2, 4

MSS max-scope-swing. 35, 39, 41, 42, 47

MTF modulation transfer function. 8, 9, 17

MTM multitaper method. 12, 17–20, 23, 25, 27, 28, 37, 59–61, 63, 65

NEQ noise equivalent quanta. 8, 9, 11

NPS noise power spectrum. 8, 9, 11–14, 30, 52, 53, 58, 61, 63

PSF point spread function. 8, 17, 18

RDP ray-driven projection. 31, 67, 69

ROC receiver operating characteristic. 7, 12

ROI region of interest. 13, 14, 17, 19, 20, 22, 23, 25, 28

S2S side-to-side. 29, 35, 47

SART simultaneous algebraic reconstruction technique. 6, 29, 30, 33–35, 39, 41, 42, 47, 68

SBS step-by-step. 29, 35, 39, 47

SDNR signal difference to noise ratio. 8, 29, 30, 36–39, 41, 51, 55

SID source-to-image distance. 66

SNR signal to noise ratio. 9

VDP voxel-driven projection. 67

WOAP windowed overlapping averaging periodogram. 11–14, 17–20, 22, 23, 25, 28, 59

Academic Curriculum Vitae

Peer Reviewed Publications

The work described in this thesis draws directly upon several peer reviewed manuscripts. The publications and the chapter to which they contribute are listed below:

Chapter 2

G. Wu, J. G. Mainprize, and M. J. Yaffe, "Spectral analysis of mammographic images using a multitaper method," Medical Physics, vol. 39, pp. 801–810, 2012.

Chapter 3

G. Wu, J. G. Mainprize, and M. J. Yaffe, "Characterization of a constrained paired-view technique in iterative reconstruction for breast tomosynthesis," Medical Physics, vol. 40, pp. 101901, 2013.

Conference Proceedings

The work in this thesis has also been published in several conference proceedings. The proceedings papers and the thesis chapter to which they contribute are as follows:

Chapter 3

G. Wu, J. Mainprize, and M. Yaffe, "Characterization of projection ordering in iterative reconstruction methods for breast tomosynthesis," in Digital Mammography, pp. 601–605, Springer, 2008.

Chapter 4

G. Wu, J. Mainprize, and M. Yaffe, "Dose reduction for digital breast tomosynthesis by patch-based denoising in reconstruction," in Breast Imaging, LNCS. 7361: 721–8, 2012.

Chapter 5

- G. Wu, J. Mainprize, and M. Yaffe, "Local spectral adaptive multitaper method with bilateral filtering for spectrum analysis of mammographic images," in Proc SPIE, pp. 8313:83134-N-1; 2012.
- G. Wu, J. Mainprize, and M. Yaffe, "Breast tomosynthesis reconstruction using a grid of blobs with projection matrices," in Digital Mammography, pp. 243–250, Springer, 2010.

Collaborative Work and Presentations

The research carried out as part of this thesis was extended to a number of collaborations and presentations that are out of the scope of the thesis.

- G. Wu, J. Mainprize, J. Boone, M. Yaffe, "Evaluation of scatter effects on image quality for breast tomosynthesis," Medical Physics, Vol. 36(10):4425, 2009.

- X. Wang, J. Mainprize, G. Wu, M. Yaffe, "Wiener filter for filtered back projection in digital breast tomosynthesis," in Proc SPIE. 8313:83134-Z-1; 2012.
- X. Wang, J. Mainprize, G. Wu, M. Yaffe, "Task-Based Evaluation of Image Quality of Filtered Back Projection for Breast Tomosynthesis," in Digital Mammography, pp. 106–13, Springer, 2010.
- G. Wu, J. Mainprize, M. Yaffe, "TU-A-301-05: Spectral analysis of breast images using multitaper method," Medical Physics, 38(6):3745; 2011.
- G. Wu, J. Mainprize, M. Yaffe, "Local spectral adaptive multitaper method with bilateral filtering for spectrum analysis of mammographic images," CIHR – Canadian Student Health Research Forum, Winnipeg, 2011.
- G. Wu, M. Hill, J. Mainprize, M. Yaffe, "Use of an Anti-Scatter Grid in Digital Breast Tomosynthesis," ISP: Breast Imaging, Radiological Society of North America (RSNA), Chicago, 2008.

Chapter 1

Introduction

Digital x-ray imaging has provided a platform upon which we can develop new technologies to enable earlier and more accurate detection of cancer.

In an effort to combat the significant public health risk represented by breast cancer, mammographic screening was introduced. In this technology, an x-ray beam is projected through the breast and the pattern of x-ray transmission is recorded. Until about 2005, recording was typically accomplished by a sheet of photographic film in contact with an x-ray absorbing fluorescent screen.

Screen-film mammography has been proven to be highly effective in the detection and diagnosis of breast cancer. Nevertheless, it is inherently limited for several reasons. 1) The three-dimensional arrangement of structures in the breast is obscured by the projection into a two dimension (2D) image and the superposition of these structures. 2) The film used to record the image has a fixed mapping of x-ray fluence to optical density. This creates the need to expose the image recording system to a certain amount of radiation to produce an image of acceptable brightness. 3) The film characteristic curve is nonlinear, causing the image contrast to vary with the exposure level to the film, independent of the inherent image contrast carried by the transmitted x-ray beam. 4) The film adds structural noise to the image due to its granular structure. 5) If the absorbing screen is made thick enough to absorb the incident x rays efficiently, there will be a loss of spatial resolution due to light diffusion in the phosphor material.

Most of these limitations have been at least partly overcome by the introduction, beginning in 2000, of digital mammography, a technique in which the screen-film image receptor is replaced by a precise electronic x-ray detector, providing a linear response over a wide dynamic range. Digitization of the detector signal and display on a high-resolution computer screen allows flexible manipulation of brightness and contrast characteristics of the image, as well as other image processing operations. Although digital mammography has been demonstrated to have improved performance in detecting breast cancer [1], its diagnostic sensitivity is still lower than ideal, likely because the technology does not solve the first problem described above, that of tissue superposition in the image. A new technology, breast tomosynthesis, a three dimension (3D) slicing image technique, offers the potential to dramatically improve image quality, and ultimately, breast cancer detection.

This chapter will outline the motivation for the optimization in image acquisition and reconstruction for digital breast tomosynthesis. Some of the fundamentals of image quality used in the evaluation of imaging system performance are introduced. The strength and limitations of existing mammography

systems are examined, as well as the expected advantages of breast tomosynthesis.

1.1 Breast Cancer and Mammography

1.1.1 Breast Cancer

Breast cancer is the most frequently diagnosed cancer among women, and the lifetime risk of developing breast cancer is estimated to be one in 10 women in Canada. An estimated 232,340 new cases of invasive breast cancer are expected to be diagnosed among women and 39,620 breast cancer deaths of women in the United States during 2013 [2]. Similar incidence rates are expected in Canada, with an estimated 22,700 new cases and 5100 deaths during 2012 [3]. This accounts for an estimated 25.6% of all new cancer cases in Canadian women, and breast cancer continues to be the most frequently diagnosed cancer in women and the second leading cause of cancer deaths in women, next only to lung cancer.

Breast cancer is a malignant tumour developed from glandular tissue of the breast. There are several different types of breast cancer, for example, invasive or *in situ* cancer. *In situ* is a term used for a relatively early stage of cancer, when the cancer is confined within the ducts, ductal cancer in situ (DCIS) or lobules, lobular cancer in situ (LCIS). About 20% of new breast cancer cases diagnosed in the USA are DCIS [4]. Nearly all women diagnosed at this early stage can be treated with a good prognosis; however some DCIS is considered more aggressive [5]. Other breast cancer tumours are invasive or infiltrating. These tumours start in the ducts or lobules of the breast but have broken through the ductal and lobular walls and invade the surrounding normal tissue. Infiltrating ductal cancer (IDC) is the most common breast cancer and counts for about 80% of all invasive breast cancers. The lethality of invasive cancer arises from its ability to spread (metastasize) to distant areas of the body and grow there without control.

There is strong evidence that early detection of breast cancer can significantly improve the effectiveness of treatment. For a localized stage cancer, when lesions are confined to the breast, the 5-year survival rate is 97.9%, dropping to 81.3% for regional disease (cancer is invasive and spread to nearby lymph nodes) and only 26.1% for breast cancer with distant metastases [6].

Other than physical breast exam, several imaging tests can be used to detect and diagnose breast cancer, including ultrasound, nuclear medicine [7] and magnetic resonance imaging (MRI). However, x-ray mammography is the gold standard and the most widely used method for early detection [8]. It is especially valuable as an early detection tool because it can identify breast cancer several years before physical symptoms develop, at a stage when treatment may be more effective. It is believed by many researchers that the recent decline of breast cancer mortality is attributable to the combination of early detection and the improvements in treatment [9, 10].

1.1.2 Breast Tissue

The main function of the breast is to produce and secrete milk. The breast is comprised of milk-producing glandular tissues (lobules), milk tubes (ducts), fat tissue and stroma (connective tissue surrounding the ducts and lobules, blood vessels and lymphatic vessels). The glands where the milk is made are grouped into lobules and the ducts carry the milk to the nipple. Within the breast, the glandular tissue and ducts are surrounded by fat tissue and supported by fibrous connective tissue. Because the

radiographic properties of the connective tissue and the glandular component are very similar, they are often collectively referred to as "fibroglandular" tissue.

Fibroglandular tissue is more radiographically opaque than fat. The linear x-ray attenuation coefficients [11] for adipose, fibroglandular and infiltrating ductal carcinoma are shown in Figure 1.1. These are the fundamental physical properties that give rise to the contrast in a mammographic image. Because fibroglandular tissue has similar x-ray properties to cancerous tissue, it is often difficult to identify a lesion in a denser breast which has a higher composition of fibroglandular tissue.

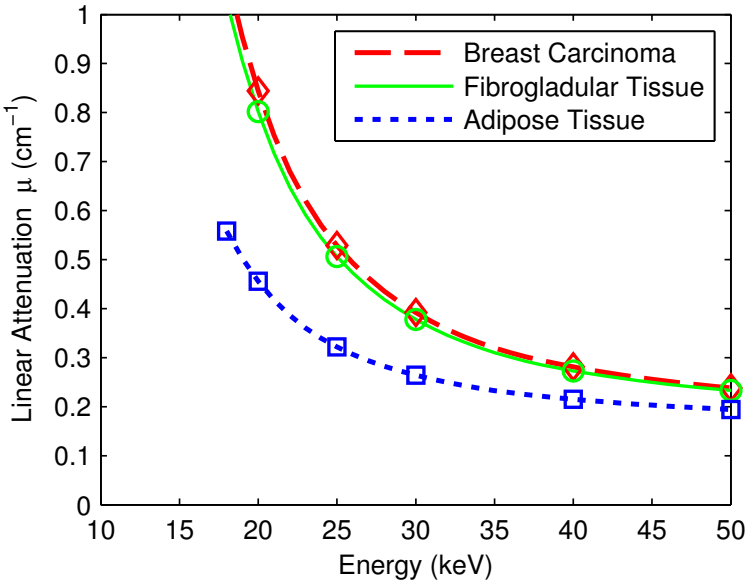

Figure 1.1: X-ray linear attenuation coefficients of normal fat and fibroglandular breast tissue and breast carcinoma tissue. Selected points are shown, measured by Johns and Yaffe [11] and fit with cubic splines.

Breast tissue composition changes with age, from mostly fibroglandular tissue during adolescence to mostly fatty tissue in older women. There is also high varability in breast density for women, irrespective of age. The concern for dense breasts in mammography is that the healthy fibroglandular tissue can obscure potential lesions, reducing sensitivity in detecting cancer. As well, there is strong evidence to suggest that women with dense breasts have an increased risk (4–6×) of developing breast cancer [12, 13] relative to women of the same age with the least dense breasts.

1.1.3 Strength and Limitation of Mammography

Mammography is a dedicated two-dimensional projection technique optimized for low dose, high contrast and high resolution imaging. The typical specification of a modern mammographic unit includes: a molybdenum anode operated at a low peak voltage (kV: 24–35), a small focal spot with a nominal size of 0.1–0.3 mm, and an added molybdenum filter at the thickness of 30–60 μm. The output x-ray spectrum provides close to optimum subject contrast for breast tissue. The molybdenum filter removes much of the higher energy radiation to enhance contrast, while it filters out the very low energy x-rays to minimize patient dose. An anti-scatter grid is commonly placed between the breast and the detector to remove preferentially scattered radiation and therefore maximize image quality. The breast is also compressed to spread out superimposed tissue, and to reduce scatter and dose. All modern systems are

equipped with automatic exposure control to produce consistent exposures to the screen-film or digital detector over a range of breast thicknesses and breast densities [14].

Generally in U.S. and Canada, two views are acquired for each breast during a screening exam, the cranial-caudal (CC) and the mediolateral oblique (MLO) view. Additional views may be taken for diagnosis purposes and follow-up imaging.

In North America, screening mammography is used for asymptomatic women annually or every two (2) years after the age of 40 or 50 (depending on policy). The effectiveness of screening mammography in detecting breast cancer can be described by the sensitivity and the specificity. Sensitivity is defined as the probability of a test giving a correct positive answer when a person has the disease and specificity is the probability of the test giving a correct negative answer when a person does not have the disease. The sensitivity of screening mammography varies depending on age group, breast density and the type and size of the cancer. Sensitivity for women over 50 can range from 40–95% depending on tumour size and type [15]. Screening mammography generally gives a specificity of 90–95%; this does lead to fairly high recall cases (5–10%) from false positives in screening [16].

A major factor contributing to this limitation of mammography is the "anatomic noise" that is created by the overlapping of normal structures within the breast, which are superimposed on each other in a standard two-dimensional mammogram. These overlapping structures can obscure a lesion, making it impossible for the radiologist to perceive it on a mammogram, and this effect becomes more pronounced as the density of the breast increases. It is this recognition that a significant percentage of breast cancers are not detected by screening mammography that has prompted recent interest in looking to other modalities as possible adjunctive screening tools. In particular, MRI and whole breast screening ultrasound have shown promise in detecting mammographically occult cancers, and the incremental benefit over screening mammography has been most pronounced in the radiographically dense breast. However, while interest in both MRI and screening breast ultrasound continues to grow, unlike mammography, neither of these techniques has yet been shown to contribute to decreasing the mortality rate from breast cancer. Tomosynthesis, on the other hand, capitalizes on the strengths and proven abilities of mammography; indeed, tomosynthesis is an extension of mammography with 3D slice imaging ability.

1.2 Digital Breast Tomosynthesis (DBT)

Application of tomosynthesis to medical imaging has been studied for more than 30 years. With the recent advances in digital flat-panel detectors [17], interest in tomosynthesis has been revived. Tomosynthesis is an x-ray acquisition and processing technique which takes a series of projection images at different angles about the body part of interest and then reconstructs multiple sectional images of the subject. These sections can be combined to produce a 3D image volume, with high spatial resolution in the reconstructed image plane and reduced resolution in the direction perpendicular to the imaging plane. Therefore, tomosynthesis provides the ability to reduce overlapping of anatomic structures and enhance the conspicuity of the tumour. In addition, the cross-sectional planes produced allow spatial localization of the tumour within the breast. It also has the potential to require less breast compression, which is one of the major complaints deterring women from mammography. Being able to provide these advantages at equivalent mammographic dose level has generated interest in the application of tomosynthesis for breast imaging.

1.2.1 Tomosynthesis Geometry for Image Acquisition

Digital tomosynthesis is based on the acquisition of multiple x-ray pictures of each breast from several ($\approx$ 10) angles. There are several possible geometric configurations for tomosynthesis. However, two particular geometries have been implemented in pre-clinical prototype systems for breast imaging. Following the terminology used by Dobbins [17], these are referred to as "complete isocentric" and "partial isocentric" geometries. Complete isocentric geometries involve rotation of both the x-ray source and detector about a fixed pivot point, as shown in Figure 1.2a. For a partial isocentric geometry, the detector remains stationary (or translated along a straight path) as the x-ray source rotates about the pivot. This geometry requires little modification to the table-top of the digital mammography system, but the angular extent for rotation is limited by the detector field of view and angular response of the detector. The breast is positioned the same way as in a standard mammography examination, with potentially less pressure applied to immobilize the breast during the procedure. The x-ray tube moves in an arc around the breast while the set of projection images is taken over about 10 seconds as shown in Figure 1.2b. Then the acquired images are sent to a computer, where they are reconstructed to produce a set of clear and focused cross-sectional slices throughout the breast resulting in a three-dimensional volume dataset.

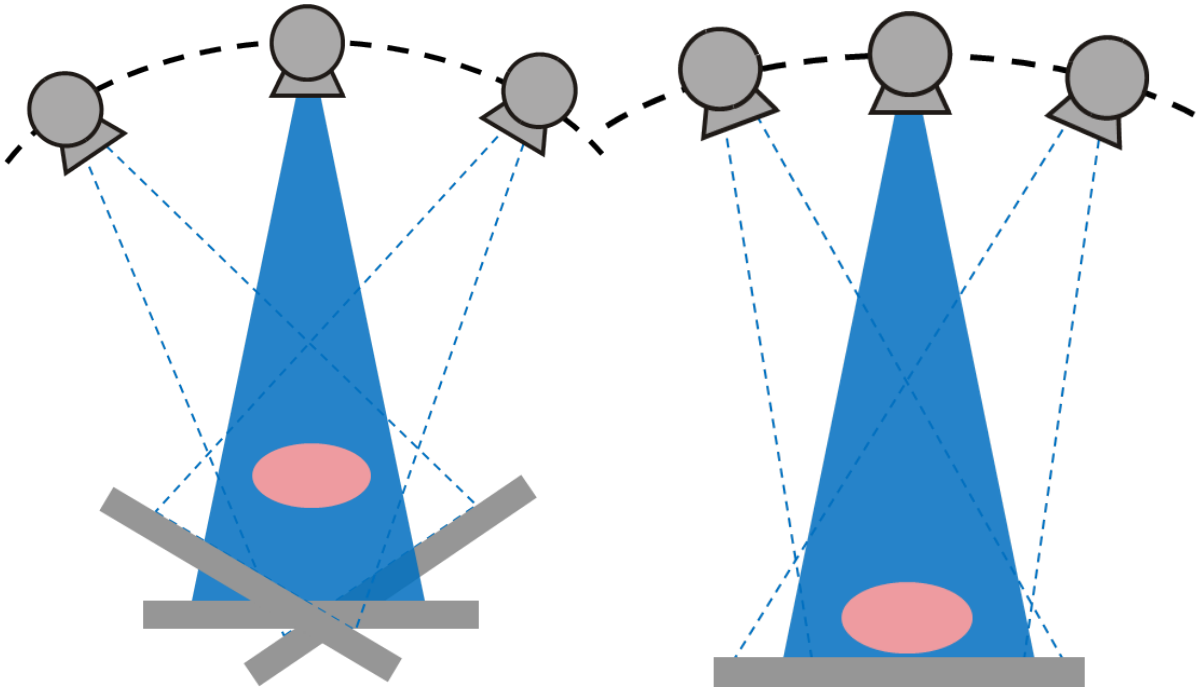

(a) (b)

Figure 1.2: Image acquisition positions for tomosynthesis: (a) Complete isocentric geometry, in which the detector rotates with the x-ray tube about a fixed pivot point; (b) Partial isocentric geometry, in which the detector remains stationary and the x-ray tube moves around some centre of rotation.

1.2.2 Reconstruction Techniques

There are families of techniques which have been described in the literature for the reconstruction of a 3D object from 2D projection images. An excellent review of methods specifically for tomosynthesis is provided by Dobbins [17]. Three basic approaches are currently in use or under development for

reconstruction of typical 3D data: (1) Fourier techniques [18, 19, 20, 21, 22, 23], which make use of the central-slice Fourier projection theorem. An example is the conventional filtered backprojection (FBP) method commonly used for computerized tomography (CT) image reconstruction. However for limited-angle tomographic applications like tomosynthesis, the frequency space of the subject is grossly under-sampled, therefore, the reconstruction result is more problematic. (2) Algebraic methods [24, 25, 26, 27, 28], which attempt to solve a series of simultaneous equations linking each voxel to projected pixel values in a number of projection images. Initially investigated in nuclear medicine, algebraic reconstruction technique (ART) proceeds iteratively by making an estimate of the subject image volume, generating a new set of projection images from the estimate, comparing the simulated images to actual measured projection data, then smearing the difference back through the subject volume to generate a new estimate. (3) Statistical methods describe the image acquisition process with a statistical model, and maximize the probability of producing the projection images to converge on a solution. These statistical methods provide more accurate system modeling than analytical FBP and ART, and, therefore, have possible advantages in terms of flexibility, resolution, and contrast and image noise.

Considerable effort has been put into the development of statistical methods for tomographic reconstruction, such as maximum likelihood expectation maximization (ML-EM) [29, 30], or the convex algorithm [31] which takes into account the statistical noise in the projection data, so that noise can be reduced in the reconstructed image. In addition, these methods can incorporate accurately the precise details of the photon transport process in the image acquisition model. Statistical reconstruction is also flexible enough to be applied to a large variety of image acquisition geometries, since it requires no explicit expressions for inverse transforms. Consequently, statistical methods for image reconstruction are attractive for tomosynthesis, despite being more computationally intensive. With the recent improvements in the capacity and speed of computers, statistical techniques are becoming popular [31, 32, 33, 34].

In this thesis, two iterative algorithms, the simultaneous algebraic reconstruction technique (SART) and the maximum likelihood convex (MLC) algorithm are mainly used in tomosynthesis reconstruction. Currently MLC has not been optimized for speed of convergence or computation cost, but, in its present form it is adequate to demonstrate the method and interpret results of this thesis.

In Chapter 3, the effects of ordering schemes on image quality for breast tomosynthesis reconstruction are characterized and evaluated. The order in which the projection views are employed in the reconstruction of tomosynthesis by iterative algorithms, such as SART and maximum likelihood (ML) has a strong influence on the rate of convergence, accuracy and the edge-blurring artifacts in the reconstructed image. Several different ordering schemes are compared, and the image quality and the formation of out-of-plane artifacts are evaluated. A new regularization method is presented that produces more accurate reconstructions with reduced artifacts comparing to the standard method of sequential ordering.

1.3 Image Quality

The quality of a medical image refers to its capacity to convey clinically relevant information. Image quality measurements are very important and necessary tools in many situations, for example, equipment design, performance specification, acceptance and constancy testing in quality assurance or quality control, and in optimization of image technique.

In medical imaging, information regarding possible abnormalities is obtained and presented to the radiologist through two major steps: (a) data acquisition and image formation, and (b) processing and

display. The former mainly relies on technical and physical characteristics of the equipment, and the latter includes the performance of the radiologist, who detects and interprets the structures in the image. The image quality of a radiographical procedure must therefore consider both these steps. In digital breast tomosynthesis (DBT) the two steps are effectively separated because the image detector is no longer also the main display medium, as was the case in film imaging.

Objective physical methods are essential in describing the quality of the equipment itself and are always used, for example, in designing new detectors. To know the quality of certain equipment in the clinic, evaluation methods for observer or diagnostic performance are adopted. In medical imaging, it is necessary to define image quality with respect to what information is retrieved from the image, i.e. as a task-based quantity. There are three different tasks in a radiologist's examination of an image [35]: (1) Detection or classification: decision about the presence of an, as yet unspecified, abnormality; (2) Estimation: quantification of, e.g., size and shape of a detected abnormality; (3) Identification: decision about likely disease patterns that correspond to the detected and recognized abnormality.

The "detection or classification" step is a prerequisite for "estimation" and "identification", and the whole image process is dependent on the "data acquisition and image formation step". Thus the quality of the physical step determines the possible quality of the observer step. Also, physical measurements of image quality are more amenable than processes involving human behavior for practical reasons. Physical measurements are objective and can be performed fairly quickly. They are generally precise and require few replications. Diagnostic performance of the system including the observer can be measured by the receiver operating characteristic (ROC) methodology in principal. In practice, however, ROC methods are too expensive and time-consuming for routine evaluation purposes, partly because multiple observers, each making many readings are required to obtain a precise result.

1.3.1 Contrast

In addition to the visual measurements, there are many physical and objective measurements that can be used to describe image quality; three principal components are contrast, spatial resolution and noise.

Contrast refers to the relative difference of signal intensity between an object (of interest) and its closely adjacent (background) region. One normalized form of contrast is defined here as:

$$C = \frac{S_{\text{obj}} - S_{\text{bg}}}{S_{\text{obj}} + S_{\text{bg}}}, \tag{1.1}$$

where S_{obj} is the average signal intensity of the object, and S_{bg} is the average signal intensity of the background. Different definitions of contrast are used at different steps during image acquisition, processing, and display. Subject contrast represents the intrinsic contrast of the image pattern prior to its being recorded; it is a theoretic contrast that can only be achieved with a perfect detector. The detector contrast refers to the relative signal difference recorded by the detector, and depends on the response of detector to different input energy. Finally the displayed contrast can be adjusted depending on the display hardware and software.

1.3.2 Spatial Resolution

Spatial resolution of an imaging system refers to the ability to discriminate two objects accurately as they become smaller and closer together. The ultimate resolution of an imaging system is dependent on the smallest recording element of the device. Nevertheless, there are many mechanisms inherent in the

imaging process that can spread out or blur the image signal, reducing the resolution further. Systematic image degradation due to spatial resolution can be characterized by observing the response of a system to known objects. For example, the point spread function (PSF), line spread function (LSF) and edge spread function (ESF) are the response of a system to point, line and step-edge objects, respectively. The modulation transfer function (MTF) of a system is defined as its response to various sinusoidal inputs; it specifies the relative amplitude of the output signal as a function of the spatial frequency of "input" sinusoids of constant amplitude at each spatial frequency. In general, the response will decrease as the frequency increases. The MTF can be derived simply by computing the two-dimensional Fourier transform of the PSF or, more commonly, by the one-dimensional transform of the LSF.

1.3.3 Noise

Noise is the random fluctuation of image signal about some mean value. It degrades image quality and limits the ability to visualize low-contrast objects. The source of noise in digital mammography may come from the variation of the x-ray tube working parameters, the electronic noise of the detector and the anatomic structures of breast tissue. The fundamental noise source is due to the discrete nature of x-ray photons and is known as quantum noise. For a uniform x-ray exposure pattern, adjacent detector elements (dels) register numbers of quanta that randomly differ from the mean value N. The distribution of the number of photons in each del is described by Poisson statistics. Therefore, the standard deviation is given by $\sigma = \sqrt{N}$. Another figure of merit, signal difference to noise ratio (SDNR) is often used to describe the relative magnitudes of useful information (*e.g.*, the difference in signal between a lesion and the surrounding background tissue) and the noise that impairs the detection of this difference. The SDNR is defined as:

$$\mathrm{SDNR} = \frac{S_{\mathrm{obj}} - S_{\mathrm{bg}}}{\sigma_{\mathrm{bg}}}, \tag{1.2}$$

where σ_{bg} is the noise of the background.

Quantum noise and other random noise sources propagated through the image acquisition are the main concerns to be suppressed by denoising algorithms discussed in Chapter 4, and they are highly correlated with the dose efficiency in X-ray imaging.

Anatomical noise refers to the normal structures in the image that can prevent an observer from detecting a potential abnormality. The anatomic noise in mammograms is an important factor in determining image quality, because the detectability of fine and low-contrast lesions can be strongly affected by the magnitude and spatial frequency content of stochastic variations in the image. Therefore, quantitative measurement of image noise characteristics is an important aspect of the assessment of imaging technologies. For example, spectral analysis of mammograms by Burgess [36] demonstrated that mammograms have an approximately isotropic 2D power law spectrum of the form, $P(f) = K_b/f^{\beta}$, with β in the range of 2 to 4 (mean about 3), where f is the 2D radial spatial frequency. The parameter K_b controls the amplitude.

The noise power spectrum (NPS) quantifies the fluctuations of signal in the spatial frequency domain and is dependent upon many of the physical factors involved in image acquisition, such as gain, spatial resolution and additive noise. It plays a central role in some figures of merit for image performance analysis, such as detective quantum efficiency (DQE) and noise equivalent quanta (NEQ), which, in turn, are related to task-based measures such as detectability index (d') [37, 38]. The measurement of NPS is elaborated in Chapter 2.

1.3.4 NEQ, DQE and Ideal Observer

The quantity NEQ is formed by the combination of the three components introduced in previous sections: a large-area signal transfer (K), image sharpness (MTF) and NPS. The signal transfer (K) is the mean pixel value defined in the same region where NPS is calculated.

$$\text{NEQ(u,v)} = \frac{MTF^2(u,v)}{NPS(u,v)/K^2}, \tag{1.3}$$

As the name suggests, the NEQ can be interpreted as the number of quanta impinging on the input surface of a perfect detector which would yield the same output noise at various spatial frequencies (u, v) as what has been measured for the actual system. The image was actually made with Q exposure quanta but it is as if only NEQ of them show up in the image [39]. The ratio between NEQ and the actual fluence Q is referred to as the DQE of the imaging system:

$$\text{DQE(u,v)} = \frac{NEQ(u,v)}{Q}, \tag{1.4}$$

DQE expresses the efficiency with which the imaging system uses the information carried by the quanta impinging on it. Both NEQ and DQE are intended for evaluating the efficiency and performance of the image system, primarily for the detector. However they are not appropriate detectability indices, because they neither contain details of the actual object to be observed nor take into account all factors influencing the detectability.

If the noise in the image is normally distributed and signal independent (additive Gaussian noise), and the imaging system is linear and shift-invariant (stationary), the best possible mathematic observer can detect a detail object $\Delta S(u,v)$ with the signal to noise ratio (SNR) or denoted as d'

$$\begin{aligned} d'^2 &= \int\int \frac{K^2 MTF^2(u,v)|\Delta S(u,v)|^2}{NPS(u,v)} \mathrm{d}u\mathrm{d}v \\ &= \int\int \frac{|\Delta I(u,v)|^2}{NPS(u,v)} \mathrm{d}u\mathrm{d}v, \end{aligned} \tag{1.5}$$

where the expected (noiseless) image of the detail has been denoted by $\Delta I(u,v)$. This d' specifies the ideal observer's detection performance of the given detail completely; therefore, it's a task-dependent image quality index. It also takes account of all important factors, including the subject contrast.

The ideal observer uses all image information in an optimal manner for its decision, therefore, d' can be interpreted as the measure of the image information with respect to the specified detection task $\Delta S(u,v)$. In this thesis, the calculation of d' is carried out using the second part of Equation 1.5 for its simplicity. The main challenge of the calculation is the accurate estimation of the power spectrum for noise (NPS) and expected signal (ΔI), which is covered in Chapter 2.

1.4 Hypothesis and Outline of the Thesis

Given the limitations of conventional mammography, especially those related to "anatomic noise", the benefits of digital breast tomosynthesis are appealing. This suggests the following hypothesis:

The image quality of digital breast tomosynthesis slices will be improved with artifact-reduction technique applied in reconstruction and denoising methods in projection and reconstruction.

The goals for this thesis are to optimize the acquisition of breast tomosynthesis and improve the reconstruction technique, under x-ray technique factors similar to conventional mammography.

The current chapter, Chapter 1, gives the motivation for this work and provides background information for the analysis of image quality of projection views and reconstructed slices in tomosynthesis.

For the assessment of image quality and measurement of detectability index, it is important to have an accurate estimate for the power spectrum of image signal and background noise. The development of a better power spectrum estimator using a multitaper technique is detailed in Chapter 2. Examination of spectrum variance versus frequency resolution and bias indicates that the multitaper approach is superior to the conventional single taper methods in the prevention of spectrum leakage and variance reduction. More than 4 times finer frequency precision can be achieved with equivalent or less variance and bias.

Chapter 3 describes how a paired-view algorithm is incorporated with iterative reconstruction techniques for DBT and helps in the reduction of artifacts spreading to out-of-plane slices. Therefore, the conspicuity of potential lesions is enhanced with improved detectability. The proposed method provides better performance for all of the metrics tested (contrast, d' and the level of artifacts) both for the uniform phantom case and in the presence of anatomical structure.

Chapter 4 deals with the random noise in DBT image acquisition and reconstruction. With the application of a patch-based denoising algorithm on projection views acquired before reconstruction and DBT slices after reconstruction, random noise was suppressed substantially while the anatomic details which contain relevant information were maintained.

Summary of the work and some future directions for related research are discussed in Chapter 5, such as the improvement of spectral precision in power spectrum estimation, and the use of an alternative voxel basis function in reconstruction.

Chapter 2

Spectral Analysis of Mammographic Images Using a Multitaper Method

Power spectral analysis in radiographic images is conventionally performed using a windowed overlapping averaging periodogram (WOAP). This Chapter describes an alternative approach using a multitaper technique and compares its performance to that of the standard method. This tool will be valuable in power spectrum estimation of images whose content deviates significantly from uniform white noise. The performance of the multitaper approach will be evaluated in terms of spectral stability, variance reduction, bias and frequency precision. The ultimate goal is the development of a useful tool for image quality assurance (QA).

A multitaper approach uses successive data windows of increasing order. This mitigates spectral leakage allowing one to calculate a reduced-variance power spectrum. The multitaper approach will be compared to the conventional power spectrum method in several typical situations, including the NPS measurements of simulated projection images of a uniform phantom, NPS measurement of real detector images of a uniform phantom for two clinical digital mammography systems, and the estimation of the anatomic noise in mammographic images (simulated images and clinical mammograms).

Without any shortening of the image data length, the bias is smaller and the frequency resolution is higher with the multitaper method, and the need to compromise in the choice of ROI size to balance between the reduction of variance and the loss of frequency resolution is largely eliminated. This part of work has been published in the journal Medical Physics [40].

2.1 Introduction

The noise in mammograms is an important factor in determining image quality, because the detectability of fine and low-contrast lesions can be strongly affected by the magnitude and spatial frequency content of stochastic variations in the image. Therefore, quantitative measurement of image noise characteristics is an important aspect of the development and assessment of imaging technologies. The NPS quantifies the fluctuations of signal in the spatial frequency domain and is dependent upon many of the physical factors involved in image acquisition, such as gain, spatial resolution and additive noise. It plays a central role in some figures of merit for image performance analysis, such as DQE and NEQ, which, in turn, are related to task-based and observer-dependent measures such as the detectability index (d') [37, 38]

and the ROC [41]. Because any error in NPS estimation will propagate directly to errors in those other metrics of performance, it is important to have an accurate estimation of NPS.

The typical technique for estimating the NPS for real images is based on averaging the power of the Fourier transform of noisy image samples taken from several images, or more routinely from smaller regions of a single noise image. Generally, the NPS is estimated from the Fast Fourier Transform (FFT) of these data records. However, the application of FFT to a finite length data gives raise to spectral leakage, which distorts the spectrum [42]. Spectral leakage, also called spectral broadening, refers to the misrepresentation of components other than integer multiples of the fundamental frequency (which equals the frequency increment in the calculated spectrum). This effect is inevitable for images with limited length and limited pixel size, but can be reduced by weighting the data with a suitable window function, which tapers the signal level at the edge of the image to zero such that when the FFT is evaluated, the edge discontinuities are minimized. These window functions do not substantially change the spectrum, but they tend to minimize some inevitable broadening of line width. However, the use of the data window functions (also called tapers) affects the bias, variance and frequency resolution of the spectral estimates [43].

Bias refers to the error caused by the mean of the estimated power spectra $E[\hat{\phi}]$ of sample images differing from the true mean (ϕ) of the stochastic process, as shown in the following equation.

$$\text{Bias} \equiv \Delta\phi = E[\hat{\phi}] - \phi. \tag{2.1}$$

A smooth and stable result with low bias is desirable in power spectrum estimation. However the stability is closely related to the variance of the estimate, and is attained by averaging over many periodograms. The variance of estimation is defined as:

$$\text{Var}(\hat{\phi}) = E\left[(\hat{\phi} - E[\hat{\phi}])^2\right]. \tag{2.2}$$

The frequency bandwidth measures the ability of the spectrum to represent the fine structure of the frequency property of the image. This can be characterized in terms of the full-width-half-maximum (FWHM) of a certain peak, also referred to as the 3dB bandwidth of the given frequency in the spectrum.

In general, single taper spectral estimates (periodograms) have relatively large variance. The variance of these estimates originates from the fact that data records are of limited size and sample spacing. To counteract this, it is conventional to smooth the single taper method by subdividing the image. Original image data are broken into overlapping segments and the power spectrum is estimated for each segment and then averaged over the segments to reduce variance. This conventional power spectrum estimation technique is sometimes called the windowed overlapping averaging periodogram (WOAP) method.

There are many available alternative methods to WOAP for spectral analysis, such as the Blackman-Tukey method [44], the maximum entropy method [45, 46] and the wavelets method [47, 48]. Each has its own advantages and disadvantages [49]; a brief summary is given in Table 2.1. Most of these methods address limitations of WOAP with improved spectral smoothness, spectral concentration (reduced spectral leakage) and bandwidth (improved frequency resolution). A popular spectral analysis alternative is the multitaper method (MTM), developed in other fields, including geophysics [50], neurosciences [48, 51], and signal processing [52, 53, 54].

Table 2.1: Alternative methods for spectrum estimation

Method	Summary	Pros and Cons
Blackman-Tukey	Fourier transformation of smoothed truncated autocovariance function	Reduced variance, low bias, poor frequency resolution
Smoothed periodogram	Smoothed periodogram estimated by DFT with modified Daniell filter	Small frequency steps and reduced variance by smoothing, but with increased bias
Maximum entropy	Parametric method: estimate autocovariance function and solve for autoregressive model parameters	Better estimation at lower frequency, low variance with high bias, unstable estimate at high frequency
Wavelets	Spectrum estimation by wavelet functions, better spatial frequency precision for higher frequencies, sensitive to weak signals	More susceptible to spurious peaks

2.2 Methods

2.2.1 Noise-power spectrum (NPS) Estimation Technique

The conventional NPS measurement technique for radiographs [37, 55] is essentially a WOAP method which can generally be summarized as follows:

1. From image, I, subtract the mean or optionally detrend the image for large scale variations of higher order (*e.g.* subtract a polynomial surface)

2. Divide the detrended image, ΔI, into small regions of interest (ROIs), $\Delta\mathrm{ROI}_i(x,y)$ where $i = 1,\ldots,N_{\mathrm{ROI}}$ is the ROI index number and N_{ROI} is the total number of ROIs. To increase the number of ROIs, the ROIs may be overlapped by some fraction, usually 50% by sidelength. The ROIs are of size $N_{rx} \times N_{ry}$ pixels.

3. Multiply each ROI by a taper function, $w(x,y)$ to reduce spectral leakage.

4. Compute the FFT for each ROI

5. Compute the raw periodogram for each ROI

6. Average the periodograms to get the estimated spectrum

This algorithm is summarized mathematically as,

$$\hat{S}(u,v) = \frac{\Delta x \Delta y}{N_{\mathrm{ROI}} N_{rx} N_{ry}} \sum_{i=1}^{N_{\mathrm{ROI}}} \Big| FFT\big\{ w(x,y) \cdot \Delta\mathrm{ROI}_i(x,y) \big\} \Big|^2, \tag{2.3}$$

where Δx, Δy are the pixel sizes of the image in x and y directions and (u,v) are the spatial frequencies along the x and y-axes. Specific protocols for NPS analysis such as the one proposed by the International Electrotechnical Commission (IEC 62220-1, 2003) [56] further address issues related to image non-uniformity and spectral contamination at low spatial frequencies.

The Hanning window is a frequently used taper, which is defined in one dimension as:

$$w(n) = 0.5\Big(1 - \cos\big(\frac{2\pi n}{N_k - 1}\big)\Big), \tag{2.4}$$

where $k = x$ or y and n is the pixel index. Other type of windows could also be used, such as the Hamming window and the Tukey windows [43] with various tapering ratios. In an informal evaluation, we tested the variance reduction in power spectrum estimation with various tapers, the Hamming and Tukey window appeared to have performance that was either equivalent to or worse than that of the Hanning window in terms of variance reduction and spectral resolution, due to their limited ability to suppress the side-lobes in their frequency responses. In this study, therefore, we limited our analysis to using only the Hanning window for all WOAP experiments.

Variance reduction in the WOAP method is generally achieved by subdividing the image into several ROIs. However, this reduction comes at the expense of increased step size in the spatial frequency domain (*e.g.* $\Delta u = 1/L_x$ where the ROI sidelength is $L_x = N_{rx}\Delta x$), and a loss of measurement accuracy at low spatial frequencies (The lowest spatial frequency variation is limited by the frequency precision $1/L_k$). Selection of the ROI size is often arbitrary: a smaller ROI may inappropriately delete or mask low spatial frequency effects and one that is too large will result in highly fluctuating estimates of the NPS.

The comparison of NPS with various ROI sizes is shown in Figure 2.1. Examples of use of 1, 9 and 49 ROIs with a 50% sidelength overlap for a native 1024×1024 pixel image are illustrated in Figures 2.1a–2.1c. The resulting NPS estimates for each case are plotted in Figure 2.1d. The WOAP technique reduces the variance of the estimate but results in a loss of frequency resolution, as shown in Figure 2.1d, and therefore an increase in the bias of the estimate.

As an alternative, we consider the multitaper spectral analysis method introduced by Thomson [44]. In this approach the image data are multiplied not by one but several "leakage-resistant" tapers, which are orthogonal basis functions and each one provides a good protection against leakage. There are a number of multitapers that have been proposed, such as discrete prolate spheroidal sequences [57], the minimum bias (MB) tapers [58] and sinusoidal tapers. Here we have selected the minimum bias tapers for multitaper spectrum estimation, because of their reported superior bias reduction [49, 58].

To explain the minimum bias multitaper approach for power spectrum estimation, we start with a one-dimensional analysis of signal $s(n)$. Discrete orthogonal sinusoidal tapers, $\{v^{(j)}\}$, form the set of tapers, where the j^{th} order taper is $\{v_n^{(j)} = \sqrt{\frac{2}{N+1}}\sin\frac{\pi jn}{N+1}\}$, and N is the number of data points. The resulting multitaper spectral estimate $\hat{S}(f)$ of the signal $s(n)$ is:

$$\begin{aligned}
\hat{S}(f) &= \frac{1}{K}\sum_{j=1}^{K}\left|FFT\Big\{v_n^{(j)}\cdot s(n)\Big\}\right|^2 \\
&= \frac{2}{K(N+1)}\sum_{j=1}^{K}\left|FFT\Big\{\sin\frac{\pi jn}{N+1}\cdot s(n)\Big\}\right|^2 \\
&= \frac{1}{2K(N+1)}\sum_{j=1}^{K}\left|y(f-\frac{j}{2N+2}) - y(f+\frac{j}{2N+2})\right|^2,
\end{aligned} \tag{2.5}$$

where $y(f)$ is the Fourier transform of $s(n)$, N is the length of the data record and K is the number (maximum order) of tapers used. These MB tapers have a much narrower main lobe, and they have no additional parameter for the spectral bandwidth. A low bias is achieved in spectral estimate because

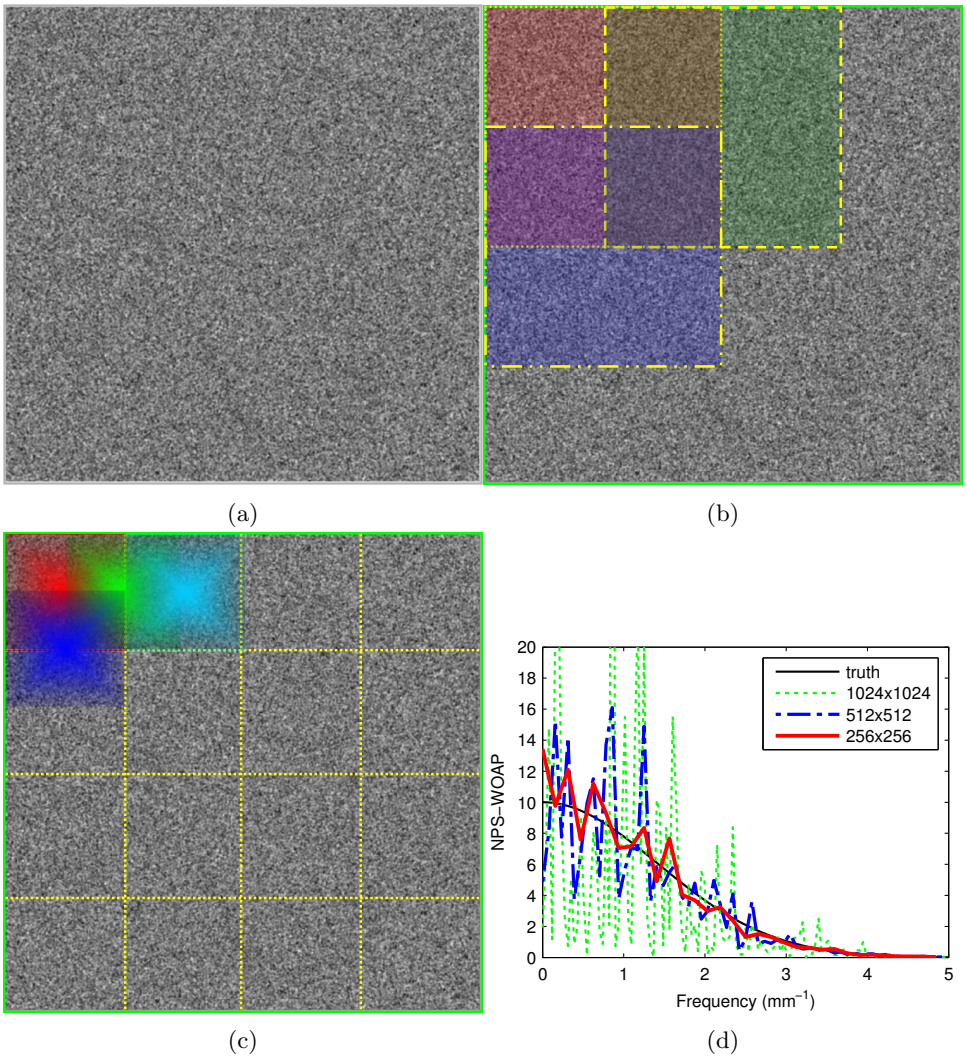

Figure 2.1: The effect of ROI size in the windowed overlapping NPS measurement method, (a) A 1024×1024 pixel uniform noisy image. (b) The image subdivided into 50% overlapping 512×512 pixel regions. Only three regions are shown. (c) The image re-divided into 256×256 50% overlapping regions. (d) The calculated NPS profile versus spatial frequency for truth (solid line) for a single image (dotted line), 512×512 ROIs (dash line), and ROIs 256×256 pixels inside (bold line).

the frequency sidelobe from $y(f + j/(2N + 2))$ cancels the sidelobe of $y(f - j/(2N + 2))$. The resultant sidelobe is suppressed after subtraction, and it is much smaller than that of the periodogram $y(f)$. It has been shown in Riedel's paper [58], that the band limited spectral concentration, $\int_{-\omega}^{\omega} |V(f)|^2 df$ of both the minimum bias and sinusoidal tapers is very close to the optimal concentration.

Extension to two-dimensional and higher dimension images is straight forward: the 2D window function is simply the outer product of two one-dimensional sinusoidal tapers. Therefore the multitaper method is suggested as follows:

$$\hat{S}(u,v) = \frac{\Delta x \Delta y}{K_x K_y} \sum_{i=1}^{K_x} \sum_{j=1}^{K_y} \left| FFT\{w_{ij}(x,y) \cdot \Delta I(x,y)\} \right|^2, \tag{2.6}$$

where K_x and K_y are the number of tapers used in each direction of the detrended image ΔI. The entire image is multiplied by each taper function, $w_{ij}(x,y)$ to reduce spectral leakage. The pictorial workflow of this multitaper approach is illustrated in Figure 2.2. This yields several tapered datasets from one full-size image that are averaged together to provide the final power spectrum estimate.

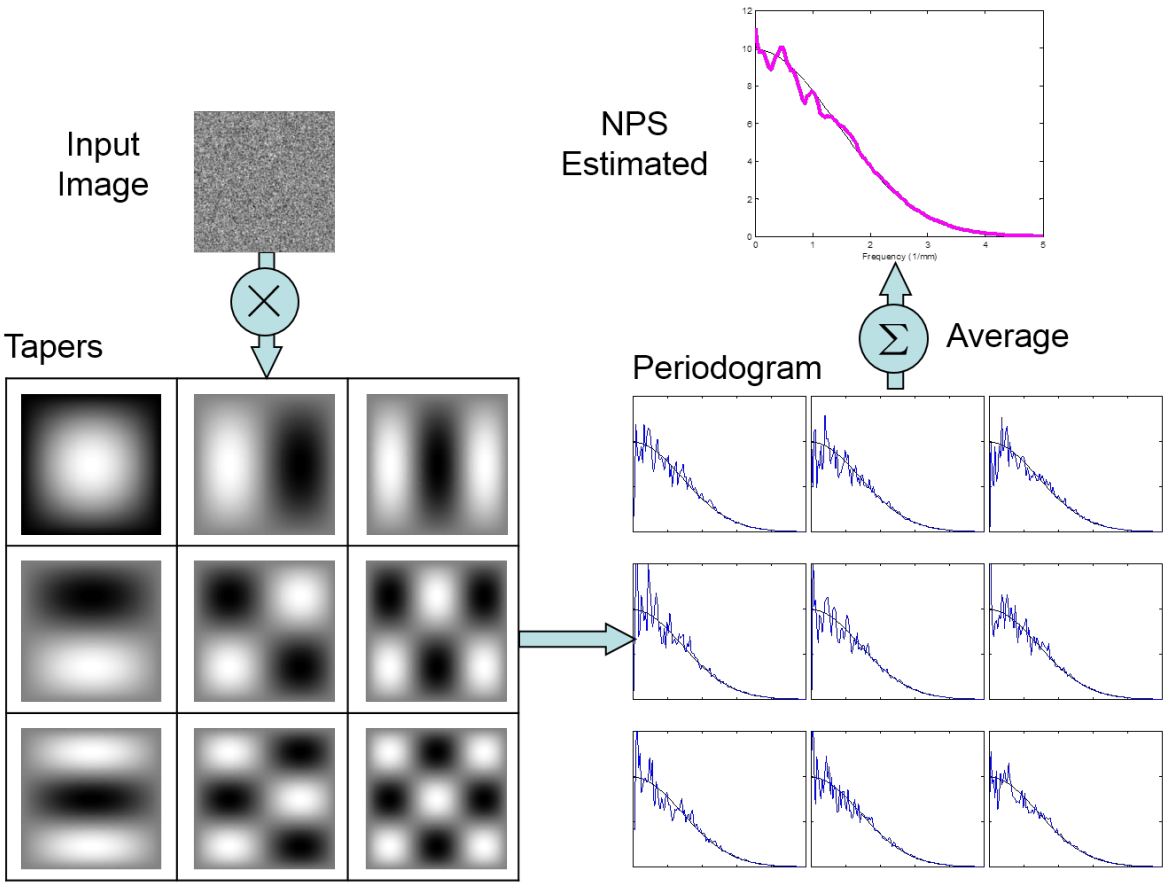

Figure 2.2: Flow chart of multitaper method. The full-size image was weighted with a series of 2D taper functions, which have the same size as the original dataset. Periodograms were produced by computing the FFT of the weighted image, and the final NPS estimation was made by the averaging of those periodograms.

Taking the Discrete Fourier Transform of each of these tapered datasets, several periodograms are produced which are properly weighted and averaged to form a final single spectral estimate (Equation 2.6). In the simplest approach a uniform weighting factor equal to $1/K_x/K_y$ is used to combine the spectral traces together to obtain the spectral estimate $\hat{S}(f)$.

2.2.2 Figures of Merit for Comparison

Several figures of merit for describing the estimator performance will be used for comparison. They are: bias (Equation 2.1), variability (Equation 2.2) and frequency bandwidth (or frequency resolution).

For the WOAP technique, the variance is reduced by increasing the number of ROIs used with the variance improving by $1/N_{\text{ROI}}$, Similarly, for the MTM technique, the variance improves with increased number of tapers ($K_x \times K_y$). The expected variance reduction should be improved as $1/K_x/K_y$. Because of this equivalence, improvements in Bias($\hat{\phi}$) and Var($\hat{\phi}$) for both techniques will be assessed in terms of N_{AVG} equal to N_{ROI} for WOAP and $K_x \times K_y$ for MTM.

2.2.3 Power Spectrum Applications

To evaluate the performance of the MTM technique, several conditions typical of applications where power spectrum would be determined are created here including simulated x-ray images from a Monte Carlo model, quality control images from a digital mammography system, simulated anatomic images and clinical mammograms.

A. Simulated x-ray images

A Monte Carlo model, running in MATLAB R2010b, was used to generate realizations of uniform images for NPS measurement. In the study of variance and bias described in subsection 2.3.1, for each number of small ROIs evaluated in the WOAP method and each number of tapers considered in the MTM method, 100 trials were simulated for the measurement of the standard deviation of the errors of the power spectrum estimation. The number of images does not affect the results. The number of images was from 20 to 100 with no significant changes in standard deviation. The system model includes a mono-energetic x-ray source, and a 2D phosphor-based flat panel detector with detector element sidelength of p. The detector was assumed to be a phosphor screen with a quantum efficiency of η and a conversion gain of g. The phosphor screen has light blurring with an isotropic MTF of $T(f)$ or PSF of $h(r)$. The detector has an added electronic noise of σ_{elec} expressed in the same units as the signal. The photon detector was assumed to have an optical quantum efficiency of 100%.

The Monte Carlo algorithm used to generate images was as follows:

a) X-ray Absorption

A uniform x-ray fluence was generated using a Poisson distribution with an average fluence of $\eta\Phi_0$ where Φ_0 is the incident fluence. Positions were recorded on a grid with spacing p.

b) Conversion Gain

For simplicity a noise free gain was used to convert the x-rays to light photons.

c) Light blur

For every light photon created, the new position was calculated by two random numbers: a number

extracted from a uniform distribution between 0 and 2π for the polar angle and a radial position extracted from the $h(r)$ using the transformation method to convert a uniform deviate to a deviate with distribution corresponding to the PSF of the phosphor.

d) Electronic detector noise

All photons were assumed to be measured by the detector and converted to charge carriers. To simulate electronic noise, an additional random Gaussian deviate with mean 0 and variance σ^2_{elec} was added to each detector element.

The NPS for this can be predicted by a simple cascaded model [59, 60], expressed in (carriers)·mm^2:

$$S(u,v) = (g^2 - g)\eta\Phi_0 p^4 T^2(u,v) + g\Phi_0 p^4 + \sigma^2_{\text{elec}} p^2. \tag{2.7}$$

To simulate spatial variations (*e.g.* "grid artifacts") of clinical QC images (described in the following section), two images I_1 and I_2 were generated after step a) of the above method. The image I_g with grid lines was composed of interlacing the weighted I_1 and I_2 as following: The first two columns of every four columns of I_g originates from an image, I_1, which has mean x-ray fluence $(1+\alpha)\eta\Phi_0$, the second two columns of every four columns of I_g is $(1-\alpha)\eta\Phi_0$, where α is a grid artifact weighting factor. The composed image I_g went through the rest steps of the above algorithm. For an image with a pixel length $p = 0.1$ mm, those simulated grid lines resulted in a peak at 2.5 mm^{-1} in the power spectrum of the image, with the magnitude

$$S(u,v) = 0.5N_x N_y \alpha^2 \eta^2 \Phi_0^2 p^2 T^2(u,v)\delta(u - 0.25/p)\delta(v) + (g^2 - g)\eta\Phi_0 p^4 T^2(u,v) + g\Phi_0 p^4 + \sigma^2_{\text{elec}} p^2. \tag{2.8}$$

Here, a number of images were simulated, the NPS was estimated by the WOAP (at 1024, 512, 256, ...) and MTM techniques. Comparison of the NPS estimates to truth was evaluated by the methods described in subsection 2.2.2.

B. Clinical QC images

Quality control images were taken from two digital mammography units, one Senographe DS (GE Healthcare, Chalfont St. Giles, UK) system and one Nuance Excel (Planmed Oy, Helsinki, Finland) system, for testing the multitaper method in NPS measurement. The "for processing" (*i.e.* unprocessed) images were used in all cases. For both machines, a 4.4 cm thick uniform PMMA slab was imaged. Ten successive images were taken on the GE system with anode/filter combination of Rh/Rh, potential at 29 kV and 80 mAs. Another ten images were acquired on the Planmed unit with the W/Ag combination, peak voltage at 30 kV and 80 mAs.

C. Inverse power-law noise and simulated anatomic background

Spectral analysis of mammograms by Burgess [36] demonstrated that mammograms have an approximately isotropic 2D power law spectrum of the form, $P(f) = K_b/f^\beta$, with β in the range of 2 to 4 (mean about 3), where f is the 2D radial spatial frequency. The parameter K_b controls the amplitude. To compare the performance of the conventional spectrum analysis technique and the multitaper method, a variety of projection views of *in silico* breast phantoms with various amount of anatomic structures were simulated such that their Fourier content follows such an isotropic inverse power-law spectrum.

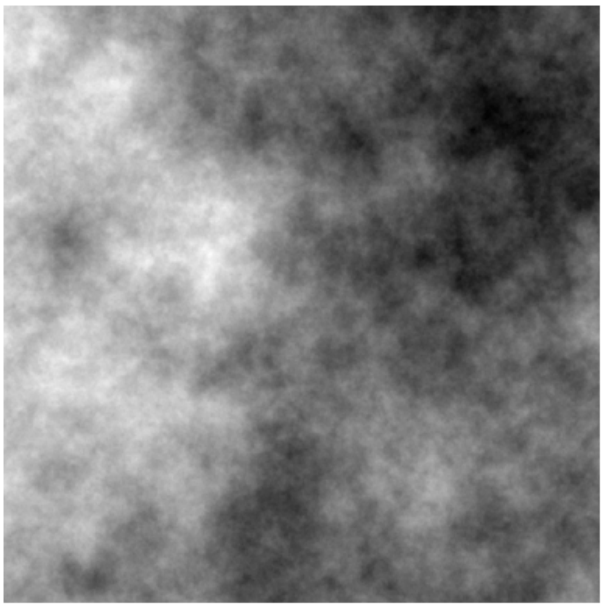

Figure 2.3: A 2D projection view of a simulated breast phantom, with 1024×1024 pixels, with a pixel side length of 0.1 mm.

For example, a 2D projection view of a breast phantom was simulated using $\beta = 3$, with no x-ray quantum noise and no other additive noise (shown in Figure 2.3). The power spectrum was estimated both by the conventional technique and the multitaper method. A first order polynomial linear fit between log-spectral density and the log spatial frequency was used to determine the estimates of the magnitude ($\hat{K}_b$) and slope ($-\hat{\beta}$) of the power spectrum. Because of the known effect of tapers at low frequency [61], the spectral density values were considered to be reliable above spatial frequency of 0.1 mm^{-1}, and the frequency range for linear fitting was chosen to be [0.1, 5].

A total of 140 breast images were simulated for seven values of β from 0.5 to 3, with 20 images for each value of β. The power spectra of these simulated breast images were estimated by both conventional periodogram and multitaper methods. The performance was assessed in terms of spectrum variance, as well as the estimation of $\hat{K}_b$ and $\hat{\beta}$.

2.3 Results

2.3.1 Projection Image with Uniform Phantom

The comparison of NPS measurement in simulated images with coloured noise is shown in Figure 2.4. WOAP results are shown as the dashed line, and those for the multitaper method using minimum bias are presented as the solid line. It is obvious that the single taper method with the full size image (1024×1024) will result in a wildly fluctuating estimation. When the original image was divided into nine overlapping ROIs (512×512), the resulting NPS has less variance. However, the minimum bias method with 5×5 tapers resulted in an even better estimation while keeping the original image intact.

As discussed in subsection 2.2.2, the improvements in Bias(ϕ) and Var(ϕ) for the WOAP and MTM techniques will be assessed in terms of number of averages (N_{AVG}), which is equal to the number of small ROIs (N_{ROI}) used for WOAP (Equation 2.3) and the number of tapers ($K_x \times K_y$) for MTM (Equation 2.6). For each number of averages (N_{AVG}), 100 trials were simulated to allow estimation of the standard deviation. The ROI size and frequency-step size of the two methods are compared in

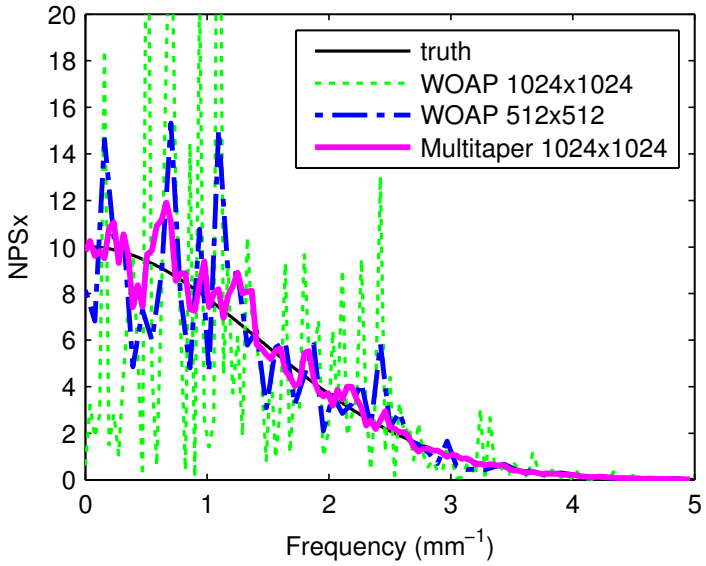

Figure 2.4: Comparison of NPS measurement in simulated images with coloured noise. WOAP results are shown as the dashed line, and the multitaper method using minimum bias is presented as the solid line.

Table 2.2. The ROI side-length decreases and the frequency-step size increases with increasing number of ROIs used in the WOAP method, however, the ROI size and the frequency-step size are independent of the number of tapers used in the MTM technique, therefore the multitaper method always has a finer frequency-step size than the WOAP method when more than one ROI is used.

Table 2.2: Comparison of WOAP and MB performance in power spectrum estimation

Number of Averages	4	9	16	49	81
ROI sidelength WOAP (pixels)	614	512	408	256	204
ROI sidelength MB (pixels)	1024	1024	1024	1024	1024
Frequency step-size WOAP (mm^{-1})	0.0163	0.0195	0.0245	0.0391	0.0490
Frequency step-size MB (mm^{-1})	0.0098	0.0098	0.0098	0.0098	0.0098

The bias and variance measured in NPS estimation by WOAP and multitaper methods are plotted in Figure 2.5 and Figure 2.6, respectively, where the conventional method is plotted as a dashed line with squares and the minimum bias method as a solid line. For a given degree of overlap (50%) in WOAP, as the original image is divided into more and more small ROIs, the averaged NPS estimation becomes smoother, and both the bias and the variance is reduced accordingly. Similarly in the multitaper results, as an increasing number of tapers are employed, the variance of the final NPS estimation decreases and the estimate becomes more stable.

To compare the two approaches, a paired t-test was made between WOAP and MTM with same number of averages, as reported in Table 2.3. For most cases, at a significance level of $\alpha = 0.01$, the null hypothesis that the WOAP and MTM result in same bias and variance reduction is rejected, except for the case where 9 ROIs are used in WOAP and 3×3 tapers are used in MTM. When the same number of ROIs or tapers is applied in the two methods, the multitaper method tends to always have less bias and variance than the WOAP method. In a second comparison, the 5×5 taper MTM measure was compared in terms of Bias(ϕ) and Var(ϕ) to results from WOAP using different number of ROIs. The 5×5 taper MTM had a bias of $(0.23 \pm 0.16)\%$ and a variance of 0.08 ± 0.05 in the power spectrum estimation. As expected the MTM with 5×5 MTM tapers performed better than WOAP for 4, 9 and 16 averages. For

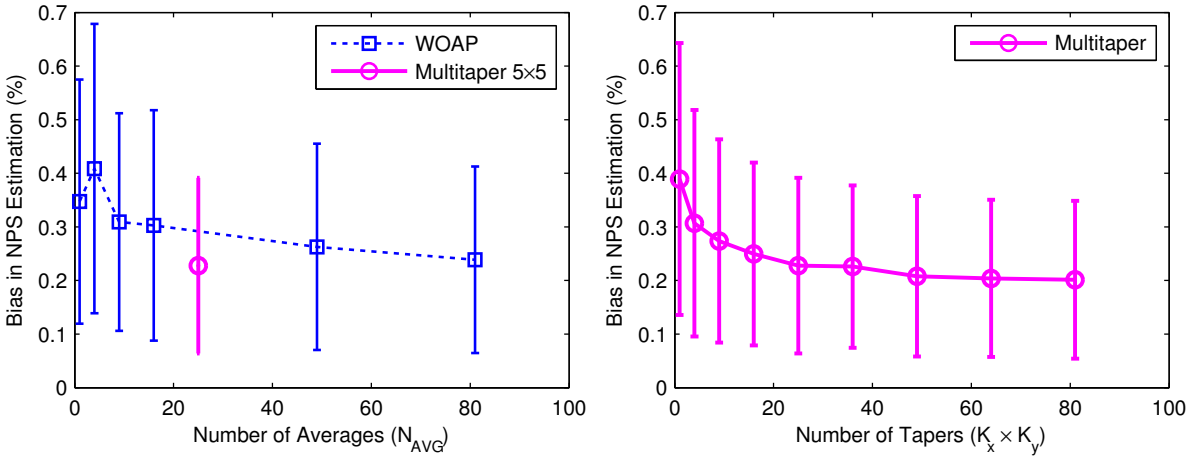

(a) (b)

Figure 2.5: Comparison of the bias in NPS measurement by WOAP and multitaper methods. The conventional method plotted as the dashed line, the MB method as the solid line.

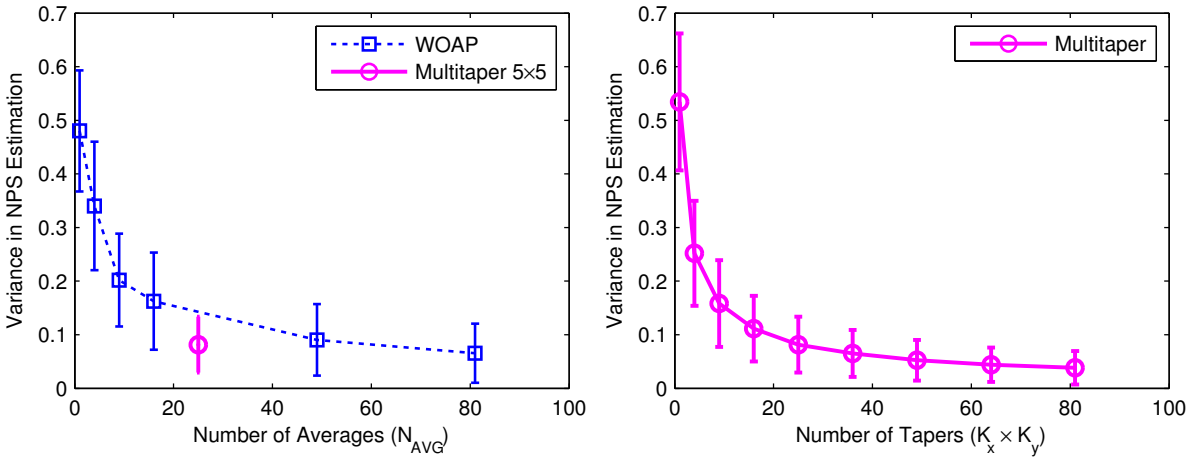

(a) (b)

Figure 2.6: Comparison of the variance in NPS measurement by WOAP and multitaper methods. The conventional method plotted as the dashed line, the MB method as the solid line.

Table 2.3: Paired t-test of WOAP and MB estimation in Bias and Variance

Number of averages	4	9	16	49	81
Bias (%), WOAP	0.41 ± 0.27	0.31 ± 0.20	0.30 ± 0.21	0.26 ± 0.19	0.24 ± 0.17
Bias (%), MB	0.31 ± 0.21	0.27 ± 0.19	0.25 ± 0.17	0.21 ± 0.15	0.20 ± 0.15
Paired t-test of bias (p-Value)	< 0.0001	0.033	< 0.001	< 0.001	< 0.001
Variance, WOAP	0.34 ± 0.12	0.20 ± 0.09	0.16 ± 0.09	0.09 ± 0.07	0.07 ± 0.06
Variance, MB	0.25 ± 0.09	0.16 ± 0.08	0.11 ± 0.06	0.05 ± 0.04	0.04 ± 0.03
Paired t-test of variance (p-Value)	$< 10^{-10}$	$< 10^{-7}$	$< 10^{-10}$	$< 10^{-10}$	$< 10^{-10}$
WOAP vs. MB (5×5 tapers), paired t-test of bias (p-Value)	$< 10^{-8}$	$< 10^{-5}$	$< 10^{-5}$	0.012	0.367
WOAP vs. MB (5×5 tapers), paired t-test of variance (p-Value)	$< 10^{-10}$	$< 10^{-10}$	$< 10^{-10}$	0.021	$< 10^{-8}$

49 and for 81 averages, however, the WOAP method showed a similar bias and variance reduction, but at the price of coarser frequency steps.

To compare the spectral resolution for the conventional and multitaper methods, grid lines in projection images were simulated with coloured noise. Those grid lines will result in a peak at 2.5 mm^{-1} in the power spectrum of the simulated image. The comparison of NPS measurement in simulated images is depicted in Figure 2.7. The single taper and full size (1024×1024) results are shown as the dotted line, the WOAP method with 49 overlapping ROIs (256×256) as the dashed line, and the multitaper method using 5×5 minimum bias tapers presented as a solid line. Compared to the first two estimations, the multitaper method resulted in smoother results of NPS, better restoration of the peak value and narrower bandwidth at the FWHM of the peak.

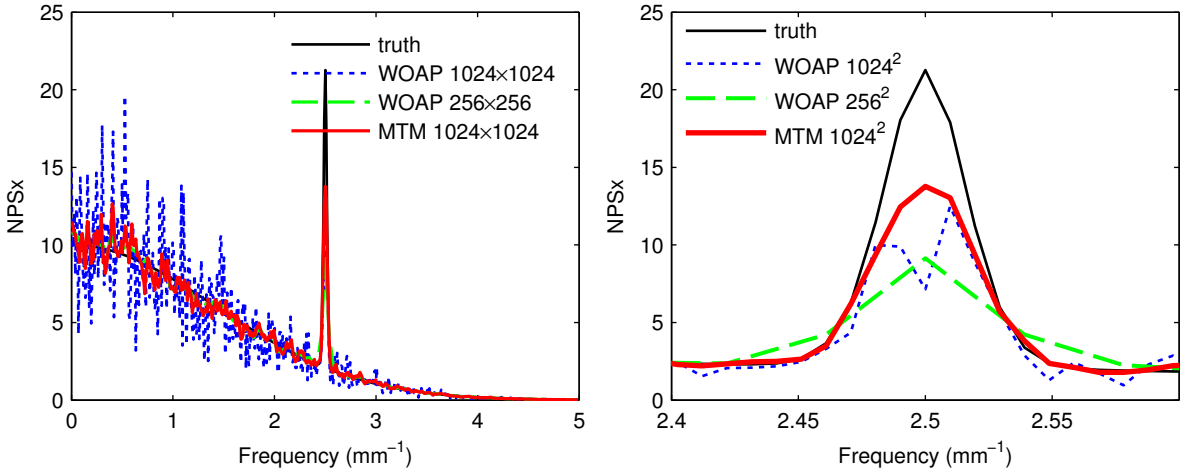

(a) (b)

Figure 2.7: Comparison of NPS measurement in simulated images, with a peak at 2.5 mm^{-1} in coloured noise. WOAP results are shown as the dotted and dashed lines, and multitaper method using minimum bias is presented as a solid line. (a) Plot of the NPS in f_x direction, (b) Zoomed view of the peak in Figure 2.7a.

In Figure 2.8, the performance of spectral resolution is illustrated by the measured bandwidth in the NPS estimation as a function of the number of ROIs/tapers, which was used for averaging in WOAP and multitaper methods respectively. In WOAP, small ROIs overlap each other by 50%. When fewer than 5×5 tapers were used, the multitaper method had a similar bandwidth with WOAP. It is obvious

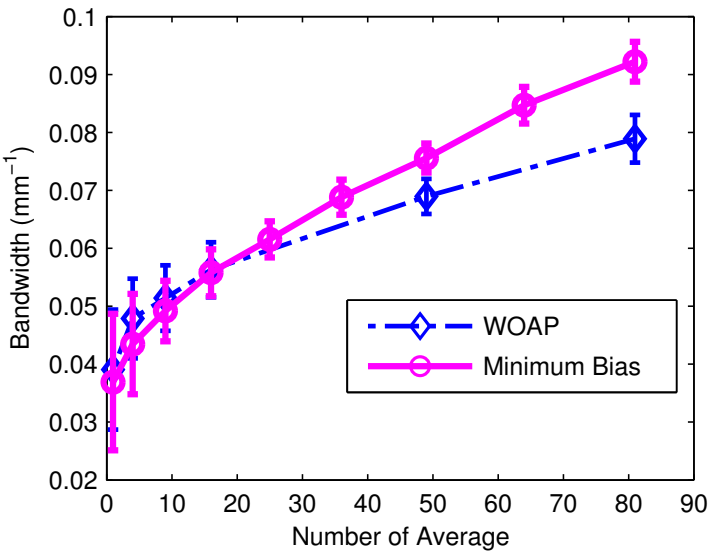

Figure 2.8: Comparison of the bandwidth performance in NPS estimation by WOAP and multitaper methods. The conventional method is plotted as a dashed line, the minimum bias method as a solid line.

that when fewer ROIs or tapers were used, the final estimation had higher spectral precision and less broadening of the peak. To balance the performance of variance reduction and spectral resolution, more tapers or ROIs should be used for a flat or smoothly changing spectrum while fewer tapers or ROIs should be used to measure a spectrum that is expected to contain sharp peaks. Hereafter, we will use 5×5 tapers for MTM if not specified explicitly.

2.3.2 QC Images from a Clinical System

The multitaper method was used to measure the NPS of a clinical system. The NPS from unprocessed images (DICOM "for processing") of a uniform phantom imaged on the Senographe DS unit is plotted in Figure 2.9a, and for the Planmed unit in Figure 2.9b. A 5×5 taper for the multitaper method was selected to balance the tradeoff between variance reduction and spectral resolution in estimation. The original image was divided into 49 overlapping ROIs (256×256) in the WOAP method ($N_{\text{ROI}} = 49$).

The images were detrended to yield the NPS in Figure 2.9 by subtraction from each image of the average of the ten images in the series. The effect of incomplete detrending is illustrated in Figure 2.10a along the f_x-axis in a comparison of the MTM and WOAP methods. In power spectrum analysis, detrending is a very important operation for removing any low-frequency or gradual changes (trends) in images. If a trend is not removed properly, it will leave a high spike in the spectrum at or near zero-frequency. This is illustrated in Figure 2.10a, where the data have been detrended by second-order polynomial data-fitting on the raw projection images from the DS system. Figure 2.10b shows the NPS resulting from the difference-image approach as used in Figure 2.9.

All images prepared for Figures 2.9, 2.10b and 2.11 have been detrended by subtracting, from each image, the average of the ten images in the series. Consequently, the estimated NPS has been properly rescaled by a factor of 10/9 according to the mean subtraction. We notice that the MTM estimation has less broadening of the peak and higher recovery of the peak value. The spikes are believed to be a result of incomplete suppression of grid lines by the flat-fielding algorithm (possibly related to timing).

Similarly for images taken from the Planmed system, the multitaper estimation is more sensitive for the spike, which has small bandwidth and higher peak value, shown in Figure 2.11.

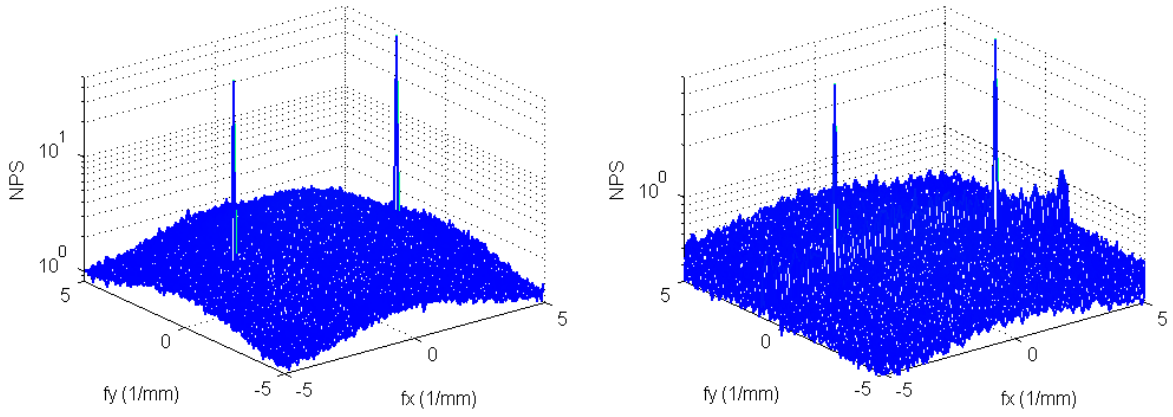

(a) (b)

Figure 2.9: Measured NPS by multitaper in projection images of a uniform phantom: (a) projection images acquired on the DS unit, (b) projection images acquired on the Planmed system.

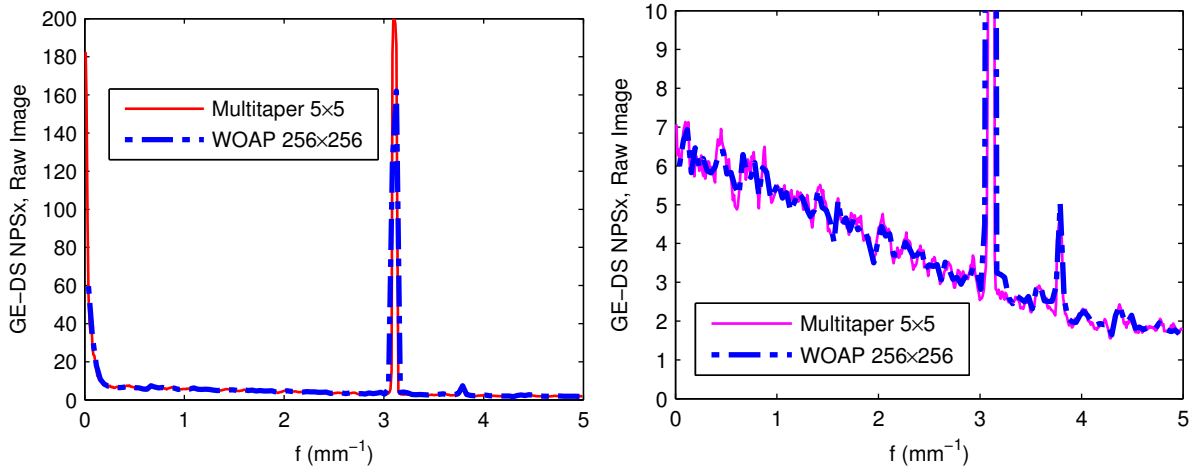

(a) (b)

Figure 2.10: Comparison of NPS measurement in projection images (raw images) acquired on the DS system with a uniform phantom, WOAP results are shown as a dashed line, and those for the multitaper method using minimum bias are presented as a solid line. (a) Polynomial fitting was used for detrending, (b) Zoomed view of NPS measurement, detrending was implemented by mean subtraction.

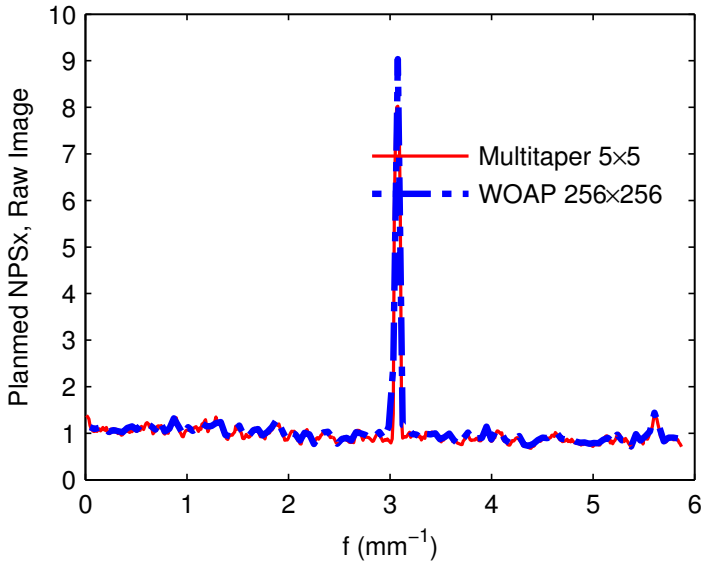

Figure 2.11: Comparison of NPS measurement in projection images (raw images) acquired on the Planmed with a uniform phantom. WOAP results are shown as a dashed line, and those for the multitaper method using minimum bias is presented as a solid line.

2.3.3 Projection Image with Anatomic Noise

An example of the estimation of the power spectrum is shown in Figure 2.12, using the WOAP method with 9 overlapping ROIs of size 512×512 and 5×5 tapers for the MTM technique. The conventional technique and multitaper method both gave a result very close to the truth value; however the latter has less variance over the entire range of frequency. A similar level of variance could be achieved with overlapping smaller ROIs, but at the cost of frequency resolution. A linear fit on the log-log curve is shown in Figure 2.12 for the MTM method with the WOAP method having a very similar curve (not shown). The parameters $\hat{K}_b$ and $\hat{\beta}$ are extracted from the fits for a range of β values, and the results of the fits are shown Figure 2.13 and Figure 2.14. For each known input β (truth), 20 trials are generated for statistics. For the estimation of β, both methods agree with the truth very well. For the measurement of K_b, the multitaper method has a better agreement with the truth value. However, if more small ROIs are used in WOAP, it will bring the curve closer to the truth.

2.3.4 Clinical Images with Anatomic Noise

Two hundred clinical mammography projections were used for the comparison of β measurement by the multitaper method and the conventional WOAP method. The digital images were first converted and normalized to log-compressed image, in which the intensity of each pixel is basically the sum of x-ray attenuation coefficients along the x-ray path. Regions of constant breast thickness, where the breast is in contact with the compression plates and detector were segmented by the breast density analysis software "Cumulus V" [62] developed in our lab. The pectoralis muscle of the chest wall was removed from the region of analysis if apparent in the image. Following the study of Burgess on mammographic structure [63], the remaining area was redivided into ROIs with a side length of 25.6 mm (256 pixels), at a degree of 50% overlap. All ROIs were within the boundary of the segmented region with constant breast thickness. Any of those containing either background (air), chest wall muscle, microcalcifications, mass lesions, or artifacts were excluded. The windowed periodogram was calculated for each ROI by both WOAP with full-size (256×256) and by MTM with 5×5 tapers. A final spectral estimate of the

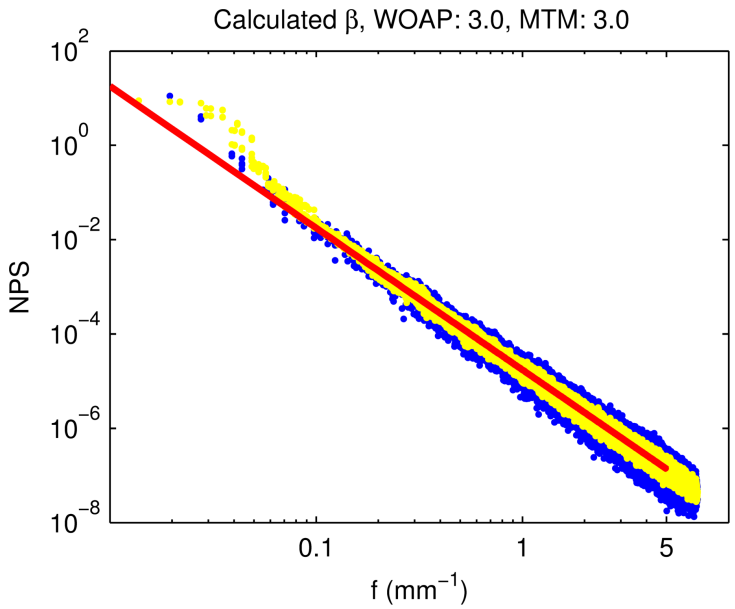

Figure 2.12: NPS estimate of a simulated breast texture image. The conventional method for nine overlapping ROIs is plotted as blue dots. The multitaper method as yellow dots and the linear fit result shown as the red solid line.

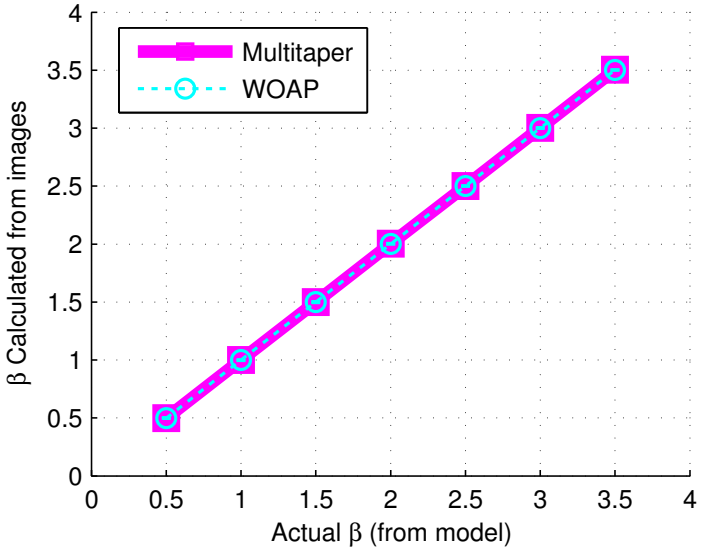

Figure 2.13: Comparison of β measurement in simulated images with anatomic noise. WOAP results are shown as a dashed line, and the multitaper method using minimum bias is presented as a solid line.

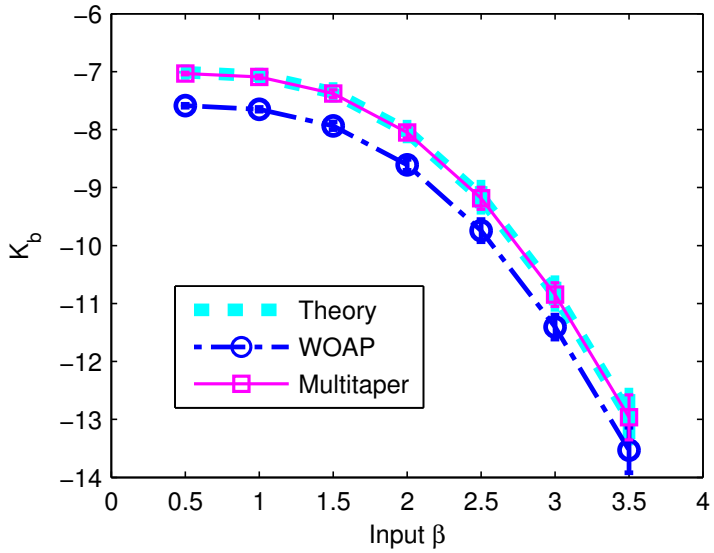

Figure 2.14: Comparison of K_b measurement in simulated images with anatomic noise. The conventional method plotted as a dashed line with error bars, the multitaper method as a solid line and the truth shown as a dotted line.

breast image was generated by averaging the periodograms for all of the small ROIs within the segmented region of each breast image. From this power spectrum, the region of constant slope in a log-log plot was determined in the range of [0.15, 0.70] cycles/mm, to reject the effect of taper performance near low-frequency and to discard the stochastic noise at higher frequencies [61]. The power spectrum of one mammogram is shown in Figure 2.15. It is obvious that the MTM results have less variance around the first order polynomial data fitting.

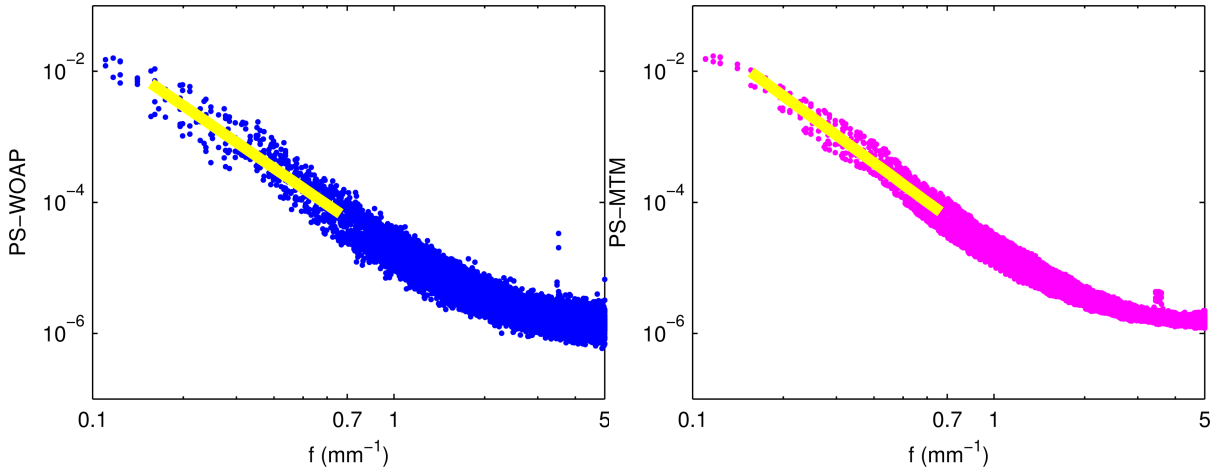

Figure 2.15: Comparison of the NPS estimate of a clinical breast image. The solid line is the linear fit for β measurement in the range of [0.15, 0.70] mm^{-1}. (a) NPS estimate of a clinical breast image using WOAP (dots). (b) NPS estimate of a clinical breast image using MTM (dots).

2.4 Disscussion and Conclusions

This work indicates the potential of using a multitaper method in spectral analysis of breast images. Without any shortening of the image data length, the bias is smaller, the frequency resolution is higher and the need to compromise in the choice of ROI size to balance between the reduction of variance and the loss of frequency resolution is largely eliminated.

In the multitaper method, the image data information downweighted by one taper is partially reclaimed by the others. Without any shortening of the image data length, the bias is smaller and the frequency precision is higher compared to the WOAP method. Variance reduction is achieved by averaging periodograms of the tapered image in full size by various window functions, rather than those of the tapered small ROIs by a single taper. To balance the performance of variance reduction and spectral resolution, more tapers or ROIs should be used for a flat or smoothly changing spectrum while fewer tapers or ROIs should be used for a spectrum with sharp peaks. For minimum bias tapers, the bandwidth of the j^{th} taper is simply $1/N$ centred about the frequencies $\pm j/(2N+2)$ [58]. Thus, the bandwidth of the multitaper spectral estimate can be adjusted locally by simply using more or fewer tapers. As an extension of the current method, this will be addressed in our further work, described in subsection 5.3.2. Also because of the mechanism of variance reduction by averaging used both in MTM and WOAP, the multitaper method is less sensitive to weak signals but less susceptible to presenting spurious peaks compared to the wavelets method [48]. The spectral sensitivity and specificity properties of the multitaper estimator haven't been investigated in this study.

Examination of spectrum variance versus frequency resolution (and bias) indicates that the multitaper approach is superior to the single taper methods in the prevention of spectrum leakage and variance reduction. For all breast image cases studied, the multitaper method gave a better estimation of K_b and β.

Because of certain heterogeneity of the breast tissue, it is very likely that clinical mammograms are not isotropic in properties, such as the orientation of structures, as shown recently in Reiser's work [64]. However, in the current literature [36, 65, 66], the reported β is the result of the radial averaged power spectrum by WOAP with many small ROIs. This may be problematic if the assumption of an isotropic mammogram is not sufficiently valid. It is unnecessary to have such an assumption for the multitaper method, because it uses the full size of the original image. Therefore, the multitaper method makes it possible to estimate the mammogram power spectrum more accurately for more comprehensive study. This is not within the scope of this thesis but could be continued in future work.

Chapter 3

Constrained Paired-View Technique for Tomosynthesis Reconstruction

The order in which the projection views are employed in the reconstruction of tomosynthesis by iterative algorithms, such as SART and ML, has a strong effect on the rate of convergence, accuracy and the edge-blurring artifacts in the reconstructed image. The purpose of Chapter 3 was to characterize and evaluate the effects of ordering schemes on image quality for breast tomosynthesis reconstruction and to explore a new constrained paired-view technique that could reduce reconstruction artifacts. Several different ordering schemes are compared, and evaluated based on the image quality and the formation of out-of-plane artifacts. A new normalization method is presented that produces more accurate reconstructions with reduced artifacts, compared to the standard method of sequential ordering.

In addition to visual assessment of image quality, several indices such as the SDNR, the artifact spread function (ASF) and the lesion detectability (d') were computed to evaluate the effect of ordering scheme quantitatively. The analysis was based on three sets of breast tomosynthesis projection images simulated for reconstruction: one set had uniform background (white noise only), and the other two contained both anatomic background and quantum noise. Clinical breast images were also studied for comparison.

The paired-view normalization provides better performance in the image quality of the reconstructed slices, and results in a lower level of artifacts in the Z direction. This implies that even a relatively simple method like the "side-to-side (S2S)" sequence, which pairs two symmetrical projections with equal angular distance from the central projection, would achieve better reconstructed image quality than the conventional "step-by-step (SBS)" method, which uses sequential projections one after another. This part of work has been published in the journal of Medical Physics [67].

3.1 Introduction

The imaging performance of tomosynthesis is complicated by physical factors such as the detector efficiency, the need for precise geometrical alignment, and the detection of x-ray scatter. One of the challenges in attempting to reconstruct a 3D breast volume from several 2D projection images is the problem of undersampling, *i.e.*, only a limited number (typically 10–20) of low-dose projections are acquired over a limited angular range (usually around $40^\circ - 50^\circ$). As a consequence of this extremely

insufficient sampling, the spatial resolution perpendicular to the plane of the x-ray detector is sacrificed, even though high resolution is maintained for slices parallel to the detector.

Two general categories of image reconstruction techniques are commonly used for tomosynthesis, iterative algorithms [17], and one-shot algorithms like Fourier transform-based filtered back-projection (FBP) [20]. It has been shown in comparison studies [68, 69] that iterative methods, including the family of algebraic reconstruction techniques (ART), and statistical algorithms like the ML method are preferred over FBP when the projections are sparse, noisy, or non-uniformly distributed. This is due to the observation that iterative methods have inherent noise reduction properties, and provide the ability to impose regularizing constraints, such as object shape and non-negativity on the reconstruction. In addition, iterative reconstructions are also flexible enough to be applied to a large variety of image acquisition geometries, because iterative algorithms require no analytic expressions for inverse transforms.

For computed tomography (CT) reconstructions using iterative reconstruction procedures, it is well known that the order in which the projections are selected for back projection has a great influence on both the quality of the approximation and the rate of convergence [70, 71, 72]. In our preliminary study, it has been showed that projection sequence also has a strong effect on DBT reconstruction for both accuracy and artifacts [73]. Here the effect of projection ordering is investigated in a limited view, limited angular range cone-beam reconstruction with a modified ML-convex reconstruction algorithm, in which pairs of projection views are used for normalization and for constraining the update of the volume. To evaluate the reconstructed image quality and artifacts quantitatively, several figures of merit (FOMs) were employed including contrast, signal difference-to-noise ratio (SDNR), noise power spectrum (NPS), artifact spread function (ASF), and task-based detectability (d').

The remainder of this Chapter is organized as follows. In section 3.2, the DBT system, data acquisition and image simulation is discussed. In section 3.3, reconstruction algorithms are described, including SART and ML-convex and the proposed constrained paired-view technique. In section 3.4, the quantitative FOMs for image quality are detailed, and in section 3.5, we compare the performance of different ordering approaches for simulated reconstructions and clinical examples.

3.2 Materials and Methods

3.2.1 Simulation of Breast Tomosynthesis System

Various configurations of DBT have been implemented, such as the complete isocentric geometry and the partial isocentric geometry [17]. In the present work, the acquisition of DBT projections was simulated in a manner similar to the way they are acquired for a tomosynthesis prototype based on a modified Senographe DS digital mammography system (GE Healthcare, Chalfont St. Giles, UK) and illustrated in Figure 1.2b. The detector remains stationary while the x-ray tube revolves about a fixed pivot point. Nine (9) projections were acquired over the angular range from $-20°$ to $20°$, with $5°$ increments. To represent the compressed breast, two types of mathematical phantoms with designs similar to that illustrated in Figure 3.1 were created. Phantom A has a uniform distribution of 50% fibroglandular and 50% adipose tissue as background. While phantom A provides a basis for understanding the artifacts of reconstruction in breast tomosynthesis, its uniform background does not represent the complex detection task typical of clinical breast screening and diagnosis. Anatomic structures in the normal breast and especially those in a dense breast (*i.e.*, where there is a high proportion of fibroglandular tissue) present a

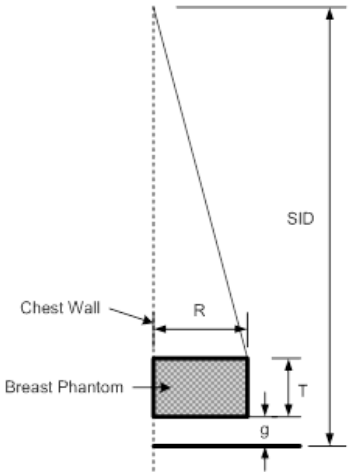

Figure 3.1: Imaging geometry for simulated phantoms, R-breast radius, T-breast thickness, g-gap between the bottom of the phantom and the top of the detector.

cluttered background and may confound interpretation of the image. Phantom B incorporates volumetric tissue attenuation information by mimicking anatomic structure using an inverse power-law model [36], while Phantom C utilizes an actual clinical tomosynthesis dataset. Phantoms B and C are described in more detail in subsection 3.2.2.

All mathematical phantoms were rectangular solids in shape and each contains a centrally-located simulated spherical tumour, with attenuation coefficients equivalent to those for infiltrating ductal carcinoma (IDC) [11]. Various diameters of this lesion between 0.6 mm and 8 mm were considered.

A simple ray-driven projection (RDP) model was applied to create projection images [74, 75]. Monoenergetic x-rays (20 keV) were used along with an assumed ideal detector and point source. For each projection angle, the primary x-ray fluence reaching the detector was calculated directly based on the path length traveled by each ray through the phantom, considering the process of both attenuation and the inverse square law. The total entrance exposure arising from the 9 projections for tomosynthesis was set to 0.9 R (air kerma 7.88 mGy), at 20 keV for a 5 cm thick breast phantom. Using normalized glandular dose (DgN) coefficients calculated by Boone [76], the mean glandular dose is estimated to be 2.7 mGy.

3.2.2 Incorporation of Background Structure

In Phantom B, the background structure was incorporated into the phantom simulation in a manner similar to those methods used by Reiser and Nishikawa, and Sechopoulos and Ghetti [77, 78, 40], using a 3D isotropic inverse power-law spectrum, $P(f) = K_b/f^{\beta}$, with β in the range of 2 to 4 (mean about 3) [36], where f is the radial spatial frequency. The parameter K_b controls the amplitude of the power spectrum. To ensure that each simulated volume provided different appearance of tissue patterns, the volume was initialized with random white noise, and then filtered with a power-law (in the spatial frequency domain) magnitude filter. To prevent a singularity at $f = 0$, the lowest nonzero f value (which is also the frequency resolution $\Delta f = 10/1024$ mm^{-1}) is used instead of zero. Next, the voxel value can be normalized to the glandularity scale from pure adipose (0%) to pure fibroglandular (100%) tissue [11]. To acquire a more realistic projection image of the simulated breast volume, further binarization was

implemented by applying a threshold in the voxel value according to the glandularity desired [77]. For the sake of simplicity in this work, the breast volume is segmented to 50% adipose and 50% fibroglandular tissue (a very dense breast).

In Phantom C, a typical fibroglandular structure was incorporated into the phantom simulation as background structure. The background structure was obtained from the patterns seen in a de-identified breast tomosynthesis dataset from a patient imaged at our institution (courtesy Dr. R. Jong), using the prototype breast tomosynthesis system (GE Healthcare, Chalfont St. Giles, UK). A volume of the size $512 \times 512 \times 74$ from a reconstructed clinical DBT image set (voxel size: 0.1 mm $\times$ 0.1 mm $\times$ 1 mm) was used as background without any segmentation of specific structures. The volume was rescaled to match the minimum and maximum values to that of the 0% and 100% fibroglandular tissue. These slices are further linearly interpolated into a $512 \times 512 \times 256$ volume with slice thickness of 0.2 mm. To minimize the effect of artifact, the volume was carefully selected such that it did not contain any obvious micro-calcifications or mass lesion in Phantom C. Due to the limited resolution of reconstruction in the Z direction, the anatomic structures spread into out-of-focus layers and the artifacts present in clinical DBT make Phantom C denser than the actual breast.

For both Phantom B and C, the pixel size in the original projection view was 0.1 mm $\times$ 0.1 mm. From these data, voxels of dimensions, 0.1 mm $\times$ 0.1 mm $\times$ 0.2 mm were reconstructed and the voxel values were arbitrarily rescaled to range from 100% adipose to 100% fibroglandular tissue.

3.2.3 Simulation of Microcalcification Array

To evaluate the performance of reconstruction algorithms on a cluster of microcalcifications and characterize any potential artifacts, an array of $3 \times 3 \times 3$ (27 in total) microcalcifications are simulated in Phantoms A, B and C. Each of these microcalcifications has a size of 0.4 mm $\times$ 0.4 mm $\times$ 0.4 mm, and it is separated from the nearest neighbour by a distance of 1.2 mm. The relative location of these simulated microcalcifications is illustrated in Figure 3.2, which are slices from Phantom C.

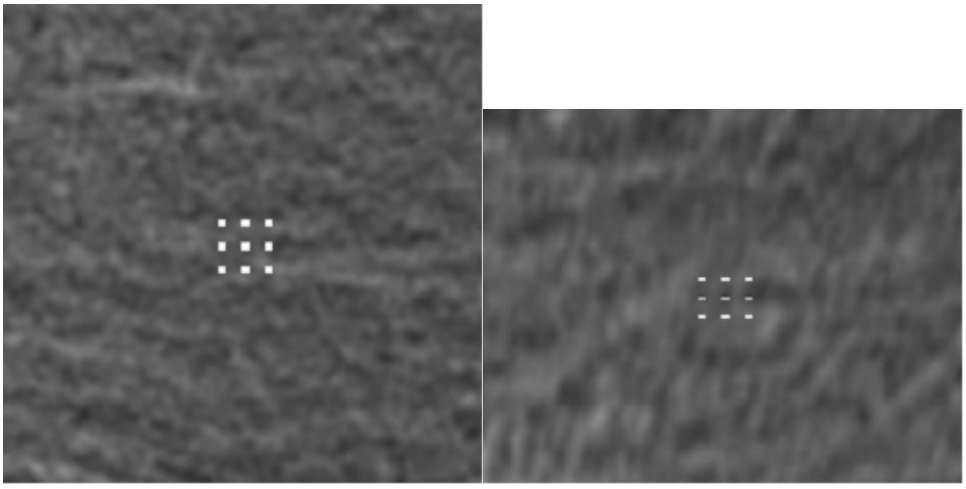

(a) (b)

Figure 3.2: Central slices of Phantom C with simulated array of microcalcifications: (a) X-Y plane, (b) X-Z plane.

3.3 Reconstruction of Tomosynthesis

The goal of tomosynthesis reconstruction is to obtain an image as the spatial distribution of the attenuation coefficient, $\vec{\mu}$, for the object. The specific data model for our DBT imaging is simplified as a discrete linear system providing projections: $p = \mathbf{H}\vec{\mu} + \vec{n}$, where $p = (p_1, p_2, \cdots, p_M)^{\mathrm{T}}$ is a vector of length M, which represents the logarithmic transformed projection data; $\vec{\mu} = (\mu_1, \mu_2, \cdots, \mu_N)^{\mathrm{T}}$ is a vector of the voxel values with length N; and $\mathbf{H}$ is the $M \times N$ system matrix in a ray-driven model for the cone-beam x-ray transform, where each element $\mathbf{H}_{ij}$ is the intersection length of a given ray r_i through a given voxel j and $\vec{n}$ is a noise vector that is representative as additive, but it may be dependent on the signal. M is the effective number of pixels in the projection images and N is the total number of voxels in the reconstructed volume. Given the projection data, tomosynthesis image reconstruction is an inverse problem which in practice cannot be simply solved by inverting the system matrix $\mathbf{H}$ due to its tremendous size and the under-sampling nature of DBT acquisition (*i.e.* $M << N$.) For example, in this study $M \approx 600 \times 300 \times 9 = 2,880,000$, $N = 256^3 = 16,777,216$, which means $M/N < 9.7\%$. Nevertheless, multiple solutions are allowed by this under-determined linear system. A particular solution of $\vec{\mu}$ depends on the choice of voxel basis; for example "blob functions" can be utilized [79]. Here the regular cubic voxel is used. More details about using blobs as an alternative voxel basis are described in section 5.4.

In iterative reconstruction, the goal is to reach a solution by successive estimates of $\vec{\mu}$. The theory of iterative reconstruction has been well described by others [68, 80]. Briefly, the process is initiated by an arbitrary first estimate of the image, usually a uniform value for all the voxels. The projections calculated from this (current) estimate are compared with the measured radiographic projection data. The result of comparison is to provide feedback that can be used to modify the current estimate, thereby creating a new estimate. This process is repeated until a satisfactory estimate is reached according to a certain stopping criterion. The algorithms differ in the way the measured and estimated projections are compared and the method in which correction is applied to the current estimate.

3.3.1 Simultaneous Algebraic Reconstruction Technique (SART)

SART is a block-iterative algebraic method developed by Andersen [26] in 1984. Closely related to simple ART, the iterative scheme consists of three phases: a projection step $\mathbf{H}\vec{\mu}^{(n)}$, a comparison step $p - \mathbf{H}\vec{\mu}^{(n)}$, and a correction step to refine the voxel values in the estimate $\mu_j^{(n+1)} = \mu_j^{(n)} + \lambda\Delta\mu_j$. SART was designed to solve the following constrained minimization: $\mu^* = argmin||p - \mathbf{H}\vec{\mu}||^2$ and subject to the non-negative constraint: $\mu \geq 0$. The correction process for one voxel in SART can be expressed by:

$$\Delta\mu_j = \frac{\sum_{i\in P_\phi}\left[\frac{\mathbf{H}_{ij}}{\sum_j \mathbf{H}_{ij}}\left(p - \mathbf{H}\vec{\mu}^{(n)}\right)_i\right]}{\sum_{i\in P_\phi}\mathbf{H}_{ij}} = \frac{\mathrm{Fid}^{(P_\phi)}}{\mathrm{NF}^{(P_\phi)}}, \tag{3.1}$$

where λ is the relaxation factor to regulate the convergence speed, $\vec{\mu}^{(n)}$ is the reconstruction volume after n^{th} correction and $\vec{\mu}^{(0)}$ is the initial guess, p is a logarithmic transformed projection image, which is performed on the collected data to convert the transmission values along a given ray to a line integral of attenuation coefficients of the voxels along the ray path. The cumulative of the geometric shadow for the grid j, which is also called the "footprint" of voxel j, at angle ϕ, is $\sum_{i\in P_\phi}\mathbf{H}_{ij}$. And $\sum_j \mathbf{H}_{ij}$ is the total intersection length of ray r_i with the whole volume. The numerator can be thought of as mainly describing the fidelity (Fid) of the match of the estimate and the projection data while the denominator

is more related to the normalization (NF) of the update step length.

This technique of normalization by the footprint showed great effectiveness in anti-aliasing [80]. Instead of updating the volume on a ray-basis, SART corrects the voxels on an image-basis. That is to say, in this method, grid correction is not performed for each single pixel separately. Instead, it is adjusted by an accumulated correction term due to all pixels in one projection P_ϕ (acquired at the orientation of angle ϕ). It has been shown that SART significantly reduces the noise and streak artifacts observed in ray-iterative ART. Also SART has demonstrated excellent performance in the limited views problem [81], which can be properly adapted for breast tomosynthesis.

Notice that in SART, the volume to be reconstructed is updated after all rays in each projection view P_ϕ have been processed. Each time all acquired projection data in the set of angles have been used at least once is referred to as an iteration. The number of updates in one iteration of SART is the same as the number of projection views.

3.3.2 Maximum Likelihood (ML) Algorithm

Maximum likelihood is another family of iterative methods. It is a statistical technique based on the photon detection problem and it can incorporate some physical modeling of the transport process. Similar to SART, the ML algorithm is an image-based iterative method for all pixels. It also has three phases in its iterative scheme: projection, comparison and correction. However, different from SART, those three phases of the ML method are defined in terms of photon intensity. The expected intensity $y(\vec{\mu}^n)$ is based on the incident photon count, d_i. In the imaging system, the number of incident x-ray photons varies with acquisition geometry (such as relative detector position and projection angle) due to the inverse-square law. The Poisson statistical model is used to describe the acquired DBT data, *i.e.* y is modeled by: Poisson$\{d \cdot \exp(-\mathbf{H}\vec{\mu}) + \text{noise}\}$ with the physical constraint $\mu \geq 0$.

In our implementation of the ML method, the convex algorithm of Lange and Fessler [31] was used. The voxel value μ was updated as follows:

$$\Delta\mu_j = \mu_j^n \frac{\sum_i \mathbf{H}_{ij}\left[y_i(\vec{\mu}^n) - Y_i\right]}{\sum_i \mathbf{H}_{ij} p_i(\vec{\mu}^n) y_i(\vec{\mu}^n)} = \frac{\text{Fid}^{(\text{all } P_\phi)}}{\text{NF}^{(\text{all } P_\phi)}}, \tag{3.2}$$

where $p(\vec{\mu}^n) = \mathbf{H}\vec{\mu}^{(n)}$, $y(\vec{\mu}^n) = d_i e^{-p(\vec{\mu}^n)}$, Y_i is the mean photon count detected by pixel i. The ML-convex algorithm was applied to breast tomosynthesis reconstruction in work by Wu *et. al.* [68, 82]. Comparing with SART, the update of each voxel in ML is averaged over all rays in all projections, which results in a relatively slower convergence speed.

3.3.3 Paired-view Normalization and Projection Sequences

A new method for the correction process and normalization step is proposed as follows:

$$\mu_j^{(n+1)} = \mu_j^{(n)} + \frac{b_1 \text{Fid}^{(P_{\phi 1})} + b_2 \text{Fid}^{(P_{\phi 2})}}{a_1 \text{NF}^{(P_{\phi 1})} + a_2 \text{NF}^{(P_{\phi 2})}}, \tag{3.3}$$

Instead of using only one projection view (P_ϕ) to update the reconstruction volume as done in SART (correction steps of Equation 3.1) or using all projection views as done with ML (Equation 3.2), two views of projection data at different angles ($P_{\phi 1}$ and $P_{\phi 2}$) are weighted and employed to perform the update.

The shared information between the two views helps to improve the resolution in the Z-direction (slice-thickness) and to reduce the artifacts in the X-Y plane of DBT. Similar to the voting strategy used in artifact reduction [82], in which projection(s) which would contribute abnormally to the reconstruction of a specific voxel are skipped, properly selected weighting factors (a_1, a_2, b_1 and b_2) can also help mitigate the out-of-plane artifacts. Two simple methods are used here to determine these weighting factors. The first is analogous to the max-deduction method [82]: compare the contributions from the two projection views; if they are the same, set all weighting factors equal one. Otherwise, simply discard the larger one. For example, if the contribution from $P_{\phi 2}$ is greater than that of $P_{\phi 1}$, then set $a_1 = b_1 = 1$, $a_2 = b_2 = 0$, and vice visa. Although this helps reduce the streak artifacts generated by high contrast objects, it will induce some artifacts in normal voxels because one or the other of the two projections will be inappropriately rejected. A reasonable compromise is to set a threshold ratio between the two contributions:

$$R_{21} = \frac{\max(\Delta\mu_j^{(P_{\phi 1})}, \Delta\mu_j^{(P_{\phi 2})})}{\min(\Delta\mu_j^{(P_{\phi 1})}, \Delta\mu_j^{(P_{\phi 2})})}, \tag{3.4}$$

For example, if the larger contribution from $P_{\phi 2}$ is more than R_{21} times that of $P_{\phi 1}$ then the projection, $P_{\phi 2}$, is ignored. Otherwise, a weighted contribution from both projections is employed. Specifically, we set $a_1 = b_1 = a_2 = 1$, $b_2 = 0.6$. In this work, we use $R_{21} = 1.5$ and $b2 = 0.6$ to limit the effect of the larger contribution and therefore diminish any potential artifacts. These parameters have important roles in the trade-off of the convergence speed and artifacts reduction. Instead of being predefined arbitrarily or computed "on the fly", these parameters can be predicted alternatively by a statistical regression model learned from a set of training projection data, which is proposed in the work of Abdurahman *et. al.* [83].

When $P_{\phi 2}$ is ignored, the update in Equation 3.3 reduces to the conventional method as shown in Equation 3.1. Otherwise, the update is essentially an ordered-subset SART or ML with two projections [84]. Under the condition when $P_{\phi 2}$ is ignored, the motivation is to mitigate the artifacts from higher intensity objects, while the weighted update using both projections accelerates the reconstruction. The algorithm convergence under these two scenarios has been studied thoroughly for SART by Jiang [85] and for ML by Lange and Fessler [86, 31]. Our study focuses on the application of this technique in DBT reconstruction and its performance of artifact reduction for high intensity objects such as micro-calcifications.

Three different sequences are investigated in this work, as listed in Table 3.1. The projection views are numbered according to their acquisition order. In the sequential, or "Step-by-step (SBS)" sequence, they are utilized in the same sequence as they were acquired. "Side-to-side (S2S)" uses left-right pairs of projections starting with the outermost pair and gradually moves inward. A significantly more complicated ordering is used for the "max-scope-swing (MSS)" scheme, which pairs each projection on one side of the normal with the projection acquired at the greatest angle on the opposite side (either view #1 or #9). For this technique, the extreme views are repeatedly used more than once in each sequence. One potential advantage of this approach is that the normalization effect of using these angles is expected to dramatically reduce out-of-plane artifacts. It is obvious that the total number of views used in these paired-view sequences is twice as many as the total images acquired, and some views are repeatedly used more than once. For a fair comparison, we also employed the projection images twice as defined in the conventional sequence shown in Table 3.1. We defined one iteration as the complete cycle of each sequence as listed in Table 3.1 during reconstruction.

Table 3.1: Sequence of projection views applied in reconstruction

Sequence name	Projection ID
Regular sequential	1,2,3,4,5,6,7,8,9,1,2,3,4,5,6,7,8,9 (each view used twice here)
Step-by-step (SBS)	(1,2),(3,4),(5,6),(7,8),(9,1),(2,3),(4,5),(6,7),(8,9)
Side-to-side (S2S)	(1,9),(2,8),(3,7),(4,6),(5,1),(6,4),(7,3),(8,2),(9,1)
Max-scope-swing (MSS)	(1,9),(2,9),(3,9),(4,9),(5,9),(6,1),(7,1),(8,1),(9,1)

3.4 Figures of Merit (FOM)

3.4.1 Contrast of Attenuation Coefficient

The image quality in terms of contrast, noise, and SDNR in reconstructed tomosynthesis images was calculated versus tumour size. Here, the normalized contrast of apparent attenuation coefficient, very similar to Equation 1.1, is defined as:

$$C = \frac{u_{\text{obj}} - u_{\text{bg}}}{u_{\text{obj}} + u_{\text{bg}}} \times 100\%, \tag{3.5}$$

where u_{obj} is the mean estimated linear attenuation coefficient in the region of interest (ROI), within the dashed circle, A, in Figure 3.3a and u_{bg} is the mean attenuation coefficient in the adjacent background region, B.

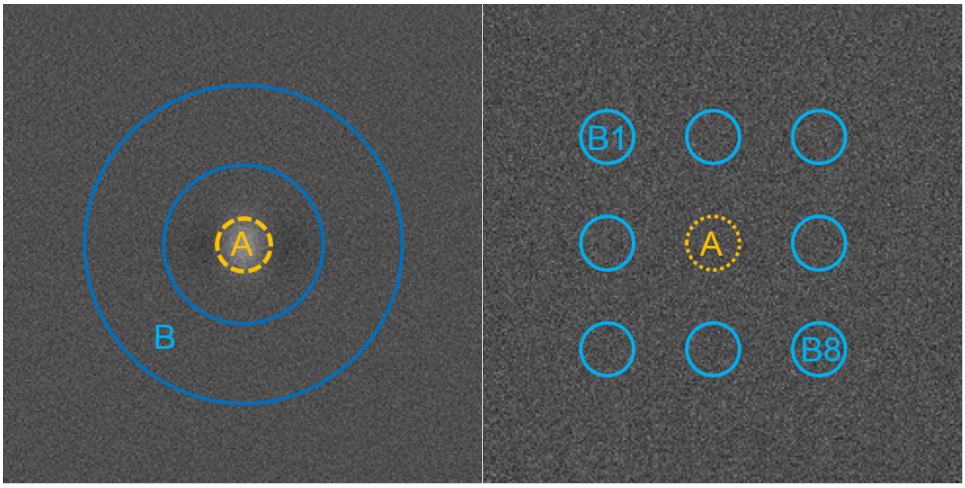

(a) (b)

Figure 3.3: Illustration of ROIs for the calculation of contrast and SDNR on the transaxial central slice of a tomosynthesis reconstruction for a breast Phantom A: (a) with a tumour in the centre, (b) with tumour absent.

3.4.2 SDNR

Another figure of merit, signal difference to noise ratio (SDNR), is used to describe the relative magnitudes of useful information and the noise that impairs the detection of this difference. It is defined in Equation 1.2, where σ_{bg} is the standard deviation of pixel values in the background region. The ROI, A, and the background region, B, are depicted in Figure 3.3a.

The expression for SDNR in Equation 1.2 is based on individual voxel statistics and thus tends to underestimate the detectability of mass lesions consisting of many voxels [87, 88]. A more relevant metric is the "lesion SDNR" [89], where the computation is performed at the relevant detail (size) of the lesion. In this application, where images are likely to be viewed slice by slice, we have chosen to compute the lesion SDNR in individual slices as follows:

$$\mathrm{SDNR} = \frac{\bar{u}_{\mathrm{obj}} - \bar{\bar{u}}_{\mathrm{bg}}}{\sqrt{\frac{1}{N-1}\sum_{i=1}^{N}\left[(\bar{u}_{\mathrm{bg}})_i - \bar{\bar{u}}_{\mathrm{bg}}\right]^2}}. \tag{3.6}$$

An ROI, A, is defined as before, inside the lesion, to yield the average lesion signal ($\bar{u}_{\mathrm{obj}}$), in an identical reconstruction with the lesion absent. $N = 8$ ROIs (B1–B8) are arranged around where A would be if the lesion were present. In these ROIs, there are no streak artifacts of reconstruction near the edge of the lesion, therefore, the effect of reconstruction artifacts on the detectability of lesions is not evaluated. The average value in each ROI was recorded $(\bar{u}_{\mathrm{bg}})_i$. The standard deviation is calculated over the eight ($\bar{u}_{\mathrm{bg}}$) values. This yields the contrast and noise characteristics at a detail size equal to that of the lesion. This is similar to the Rose definition of SNR for a disc of a given size [87]. The ROI, A, and the background regions, B, are depicted in Figure 3.3b. Background ROIs (B1-B8) are arranged such that they are separated by a distance equal to the diameter of the lesion. The same spacing is used for the lesion-present and lesion-absent images. All SDNR results presented hereafter will be "lesion SDNR" rather than the voxel-by-voxel SDNR of Equation 1.2.

3.4.3 Model Observer and Detectability Index

Considerable research has been undertaken in the development of model observers [90, 38], which provide important absolute scale for evaluating human performance, depending on the characteristics of the image and the imaging task. For a range of signal size with various acquisition and reconstruction parameters, a signal-known-exactly (SKE) detection task (also referred as detectability) was estimated by utilizing an ideal prewhitening (PW) observer model instead of human observers.

The ideal observer SNR or the in-plane detectability index (d') is a task-based image quality FOM expressed in the spatial frequencies of interest [91],

$$d'^2 = \int\int \frac{(MTF \cdot \Delta H)^2}{P_B(f_x, f_y)} \mathrm{d}f_x \mathrm{d}f_y = \int \frac{|S(f)|^2}{P_B(f)} \mathrm{d}f, \tag{3.7}$$

where MTF is the modulation transfer function, ΔH is the task function given by the difference of the Fourier transform of the two hypotheses (signal present and signal absent). As a detection task in the present study, ΔH is the Fourier transform of the signal-only profile in the phantom. f is the spatial frequency and $|S(f)|^2$ is the power spectrum of the reconstructed signal, which is generated by subtracting the uniform background from the signal-plus-background image, using a reconstructed uniform background to obtain the spectrum of the reconstructed signal. Both the power spectrum of the signal and that of the background $P_B(f)$ are estimated by the minimum bias multitaper method MTM [40] described in Chapter 2.

3.4.4 Artifact Spread Function (ASF)

Reconstruction artifacts are inevitable in tomosynthesis slices because of under-sampling of the 3D space due to the limited angular range and limited views. Artifacts appear as streaks or blurred representation of off-focus objects in cross-sectional planes that are parallel to the detector. The ASF [68] is employed to quantify this type of artifact, which is the distribution of the blurred object in adjacent slices along the Z direction. As a function of distance, the ASF measures the quality of vertical resolution, and is defined as:

$$\mathrm{ASF}(z) = \frac{\bar{u}_{\mathrm{blur}}(z) - \bar{u}_{\mathrm{bg}}(z)}{\bar{u}_{\mathrm{obj}}(z_0) - \bar{u}_{\mathrm{bg}}(z_0)}, \tag{3.8}$$

where z_0 is the location of the in-focus plane of the feature, $\bar{u}_{\mathrm{obj}}(z_0)$ is the mean reconstructed voxel value of the object in focus plane, and $\bar{u}_{\mathrm{blur}}(z)$ is that of its blurred version at other planes. $\bar{u}_{\mathrm{bg}}(z_0)$ and $\bar{u}_{\mathrm{bg}}(z)$ are the mean values of the background respectively. The regions of interest for analysis of lesion and the image background are the same as those described above for the SDNR calculation.

3.5 Results

3.5.1 Results of Phantom A with Uniform Background

For Phantom A with uniform background, central orthogonal slices of the reconstructed images using ML algorithm with step-by-step sequence are shown in Figure 3.4. We observed the overshoot in the horizontal direction around the lesion in X-Y plane and the spread of artifacts into out-of-focus planes in the X-Z plane.

The contrast results for Phantom A are shown in Figure 3.5. The comparison of contrast results for various sequences in ML with paired views (MLPV) method are shown in Figure 3.5a, the "max-scope-swing" (MLPV-MSS) scheme performs best in contrast restoration and "side-to-side" (MLPV-S2S) the next. The simplest "step-by-step" (MLPV-SBS) method tends to be equivalent to the regular ML in the performance of contrast. Compared to the regular ML algorithm, the contrast achieved in MLPV-MSS technique is improved by 12.6% on average for each number of iterations.

The comparison of contrast versus lesion size for various sequences of the maximum likelihood with paired views (MLPV) and SART methods is shown in Figure 3.5b. For lesions larger than 2 mm in diameters, the MSS scheme performs better than the other two sequences in contrast restoration and SBS the worst. Compared to SART results, the contrast achieved in MLPV with MSS is enhanced more than 44.3% for lesions of 4 mm in diameter, and more than 60.1% for those lesions of 8 mm in diameter.

The comparison of lesion SDNR results for various sequences in ML methods is shown in Figure 3.6 for phantom A: the "side-to-side" scheme achieves the highest SDNR and the "max-scope-swing" method the next. Even the simplest "step-by-step" paired-views ML method has better performance in SDNR than the regular ML.

The ASF results measured in the reconstructed volumes of the uniform phantoms using Equation 3.8 are demonstrated in Figure 3.7. The "max-scope-swing" has the narrowest ASF curve compared to all other schemes which means a better resolution of the object of interest in the Z direction, and better suppression of the artifacts among slices.

The detectability, d', results were extremely high (> 100) for lesions larger than 1 mm of diameter in Phantom A, even under reasonably low dose conditions.

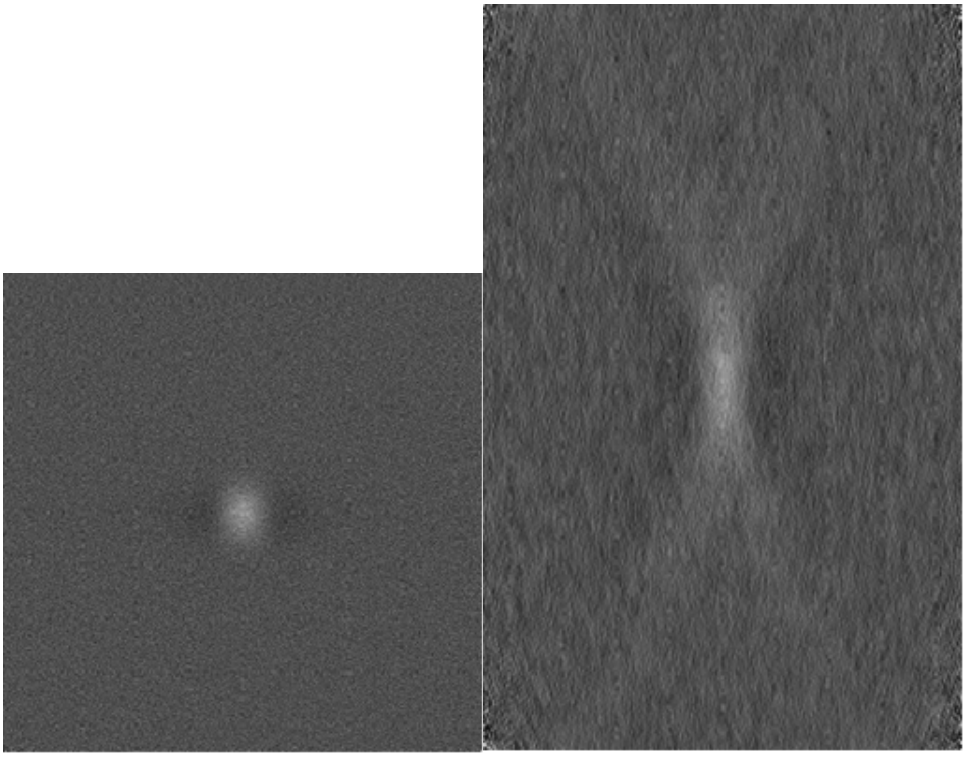

(a) (b)

Figure 3.4: Central slices of the reconstructed image with a 2 mm diameter lesion in Phantom A: (a) in the X-Y plane, (b) in the X-Z plane.

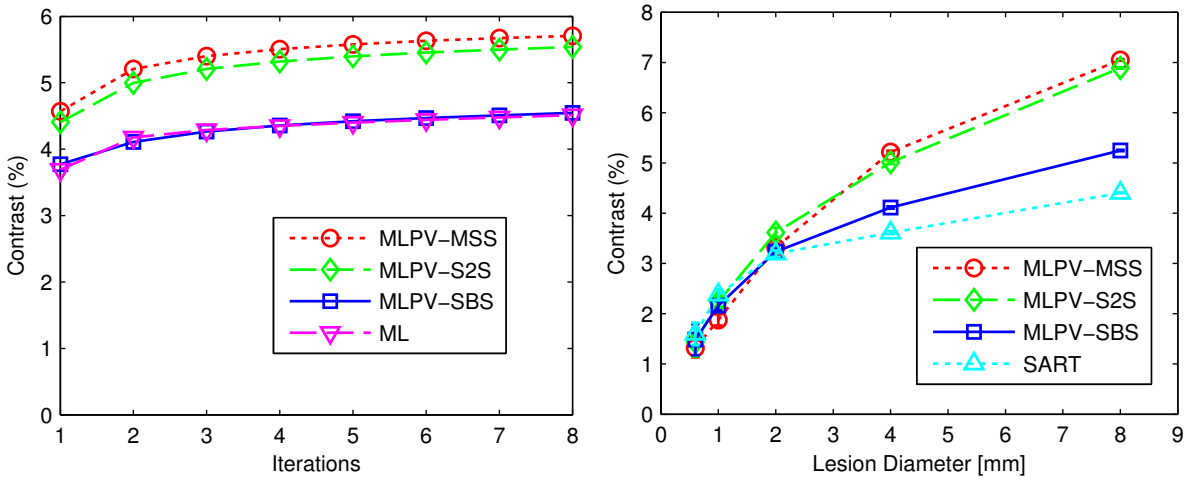

(a) (b)

Figure 3.5: Comparison of the contrast in the Phantom A reconstruction: (a) contrast as a function of number of iterations for ML reconstruction method with various sequences, (b) contrast as a function of lesion sizes for various reconstruction algorithms.

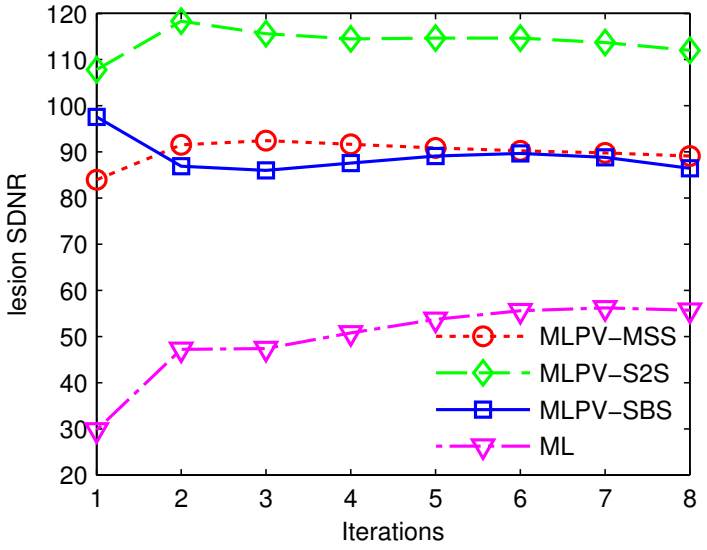

Figure 3.6: Comparison of the lesion S-DNR as a function of iteration numbers in Phantom A for various sequences in MLPV method. Results for SART (not shown) are similar to ML.

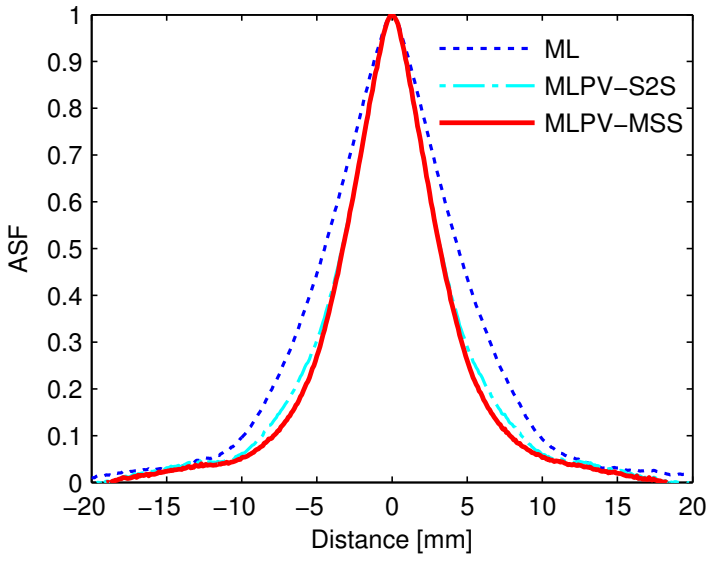

Figure 3.7: Comparison of the ASF in Z direction for Phantom A with various reconstruction methods.

3.5.2 Results of Phantom B and C with Simulated Background

The contrast results for Phantom B and C are shown in Figure 3.8a and Figure 3.8b, respectively. The comparison of contrast in Phantom B showed small but not significant difference between the three sequences for MLPV method. Comparing to Phantom C, the high breast density (50%) in Phantom B makes it difficult to restore the lesion intensity, and therefore lower conspicuity was achieved in the reconstructed slices of Phantom B by all algorithms. The contrast result of Phantom C demonstrated that the MLPV with MSS scheme has better performance than other sequences for lesions larger than 2 mm in diameter.

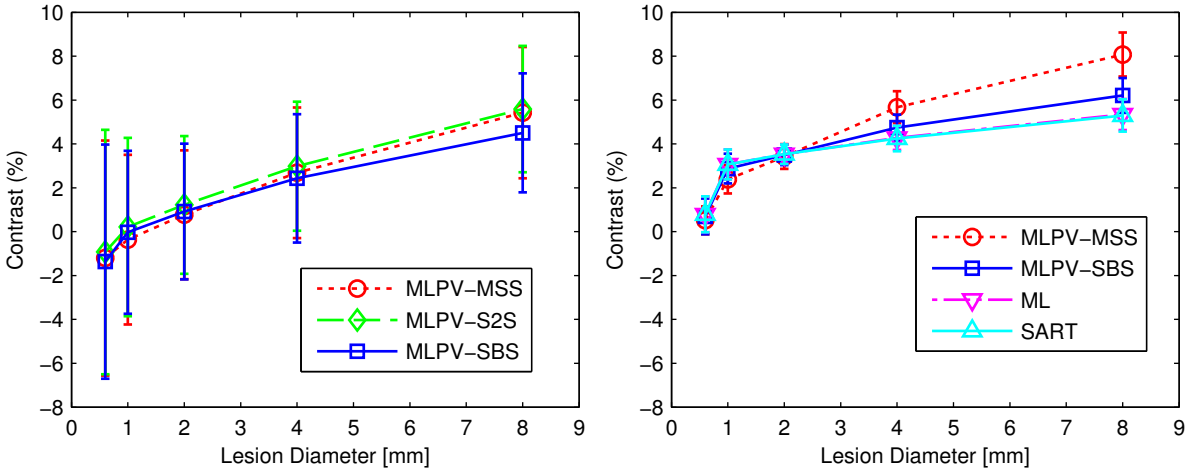

Figure 3.8: Comparison of the contrast as a function of lesion sizes: (a) in Phantom B for ML reconstruction algorithms, (b) in Phantom C for various reconstruction methods.

Because lesion SDNR is very sensitive to the choice of background regions, it is not a particularly useful FOM for any images with anatomic structures. Therefore, it was not used to evaluate the reconstructed slices in Phantom B or C. The ASF results measured in the reconstructed volumes of Phantom C are plotted in Figure 3.9. The "max-scope-swing" has the narrowest ASF curve compared to all other schemes which means a better resolution of the object of interest in the Z direction, and better suppression of the artifacts among slices.

We also measured the detectability of low-contrast lesions by the ideal observer in the reconstructed slices of the Phantom B with simulated tissue background, as demonstrated in Figure 3.10. The results suggest that the MLPV algorithm with MSS scheme yields a higher detectability than other sequences.

The detectability results in Phantom C were shown in Figure 3.11, as expected, the MLPV technique has better performance than the ML and SART for various lesion sizes.

3.5.3 Results of Microcalcification Array

Reconstructed central slices from Phantom C with the simulated cluster of microcalcifications are shown in Figure 3.12. Artifacts from the out-of-focus planes are smeared horizontally according to the direction of X-ray tube travel.

A regular array of high contrast signals is generally problematic for tomosynthesis reconstruction

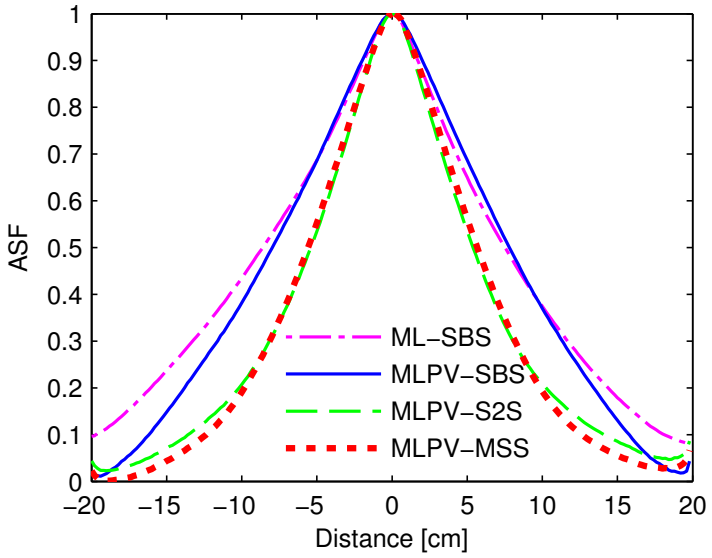

Figure 3.9: Comparison of the ASF in the Z direction for Phantom C with various reconstruction algorithms.

algorithms, especially when one of the axes is aligned perpendicular to the rotation axis as was done in this test. For all algorithms, we found false positive microcalcifications in reconstructed images. When those x-rays intersecting such voxels happen to go through two or more different microcalcifications, they created a false microcalcification image that looks more conspicuous than the usual streaks. Nevertheless, compared to a standard view (ML-SBS) reconstruction as seen in Figure 3.12a and 3.12c, the constrained paired-view (MLPV-MSS) algorithm exhibits less ringing artifact along the X direction (Figure 3.12b) and less out-of-plane spreading (*i.e.* streaks) along the Z direction (Figure 3.12d).

3.5.4 Results of Clinical Examples

Calcifications are usually found in breast images. Whether small or large in size, the shape and distribution provide important information for diagnosis. DBT reconstruction with artifacts from calcifications are shown in Figure 3.13. These are the reconstructed slices after eight iterartions. In the first row (Figure 3.13a and Figure 3.13b) are the results from SART with conventional step-by-step showing, a large calcification in slice (Z = 20 mm) and its multiple replicates in upper slice (Z = 28 mm). The middle row (Figure 3.13c and Figure 3.13d) shows the results from ML with step-by-step sequence. Less overshoot is observed around the large calcification and the microcalcification in the upper slice (Z = 28 mm) has higher contrast and is easier to discriminate. The reconstructed slices from MLPV with max-scope-swing are depicted in the third row (Figure 3.13e and Figure 3.13f), in which both the large and small calcifications have sharp edges and higher contrast, and less overshoot artifacts in the horizontal direction. Replication of the large calcification in the upper slice was markedly reduced although not totally eliminated by the MLPV algorithm. We also observed that overall anatomic features appear sharper in the ML reconstruction.

Performance of the artifact reduction methods by constrained paired-view is further demonstrated in Figure 3.14, which shows the distribution of artifacts from a large calcification in the X-Z plane perpendicular to the detector. All images are displayed with the same window and level of intensity. In

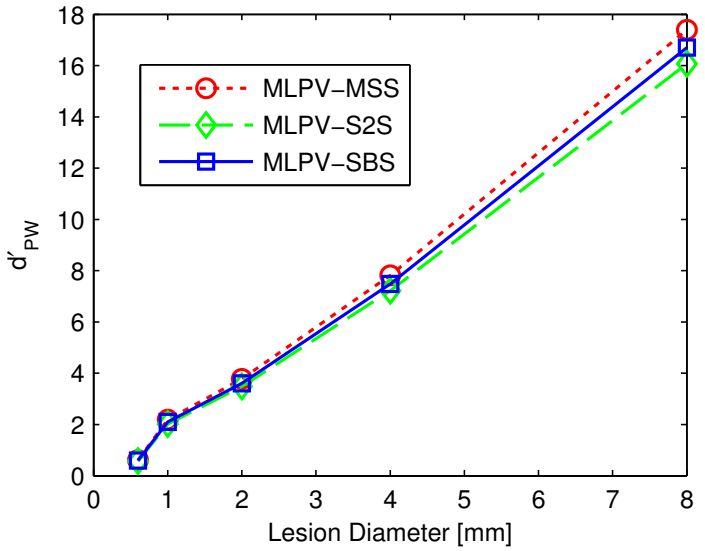

(a)

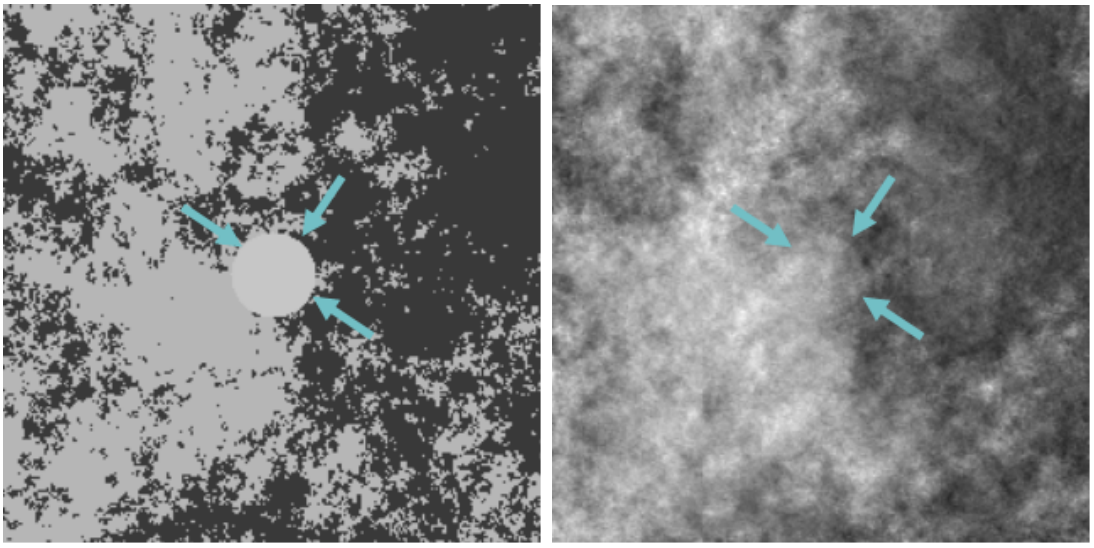

(b) (c)

Figure 3.10: Lesion detectability in the reconstructed central slices of Phantom B: (a) Comparison of the detectability as a function of lesion size in Phantom B for various sequences in MLPV method. (b) Central slice of Phantom B with lesion diameter in 4 mm, displayed in the same window and level with the right figure. (c) Reconstructed central slice of Phantom B with lesion diameter in 4 mm, which has margin marked by arrows.

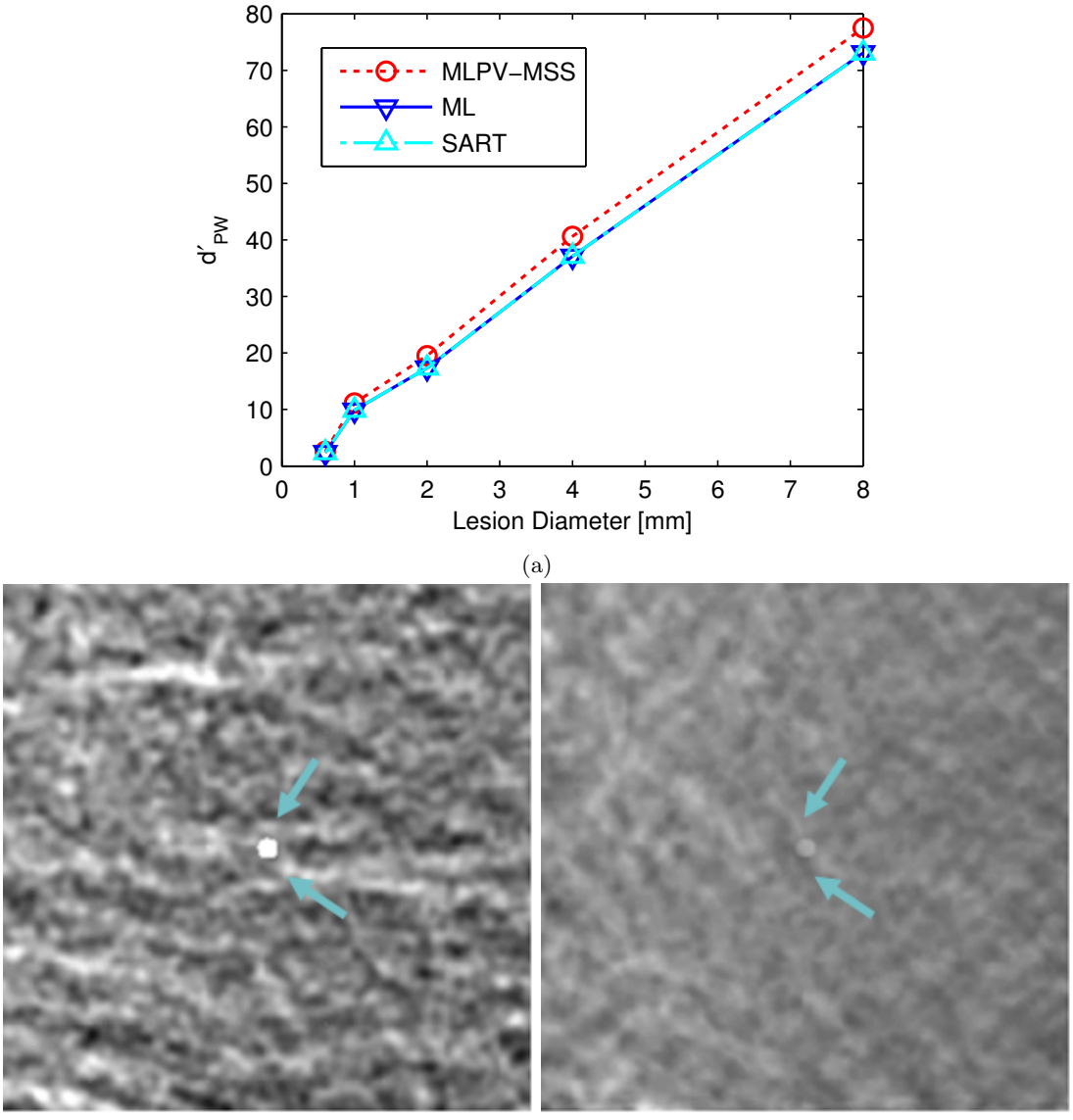

(a)

(b) (c)

Figure 3.11: Lesion detectability in the reconstructed central slices of Phantom C: (a) Comparison of the detectability as a function of lesion size in Phantom C for various reconstruction algorithms. (b) Central slice of Phantom C with lesion diameter of 1 mm, displayed in the same window and level with the right figure. (c) Reconstructed central slice of Phantom C with lesion diameter of 1 mm.

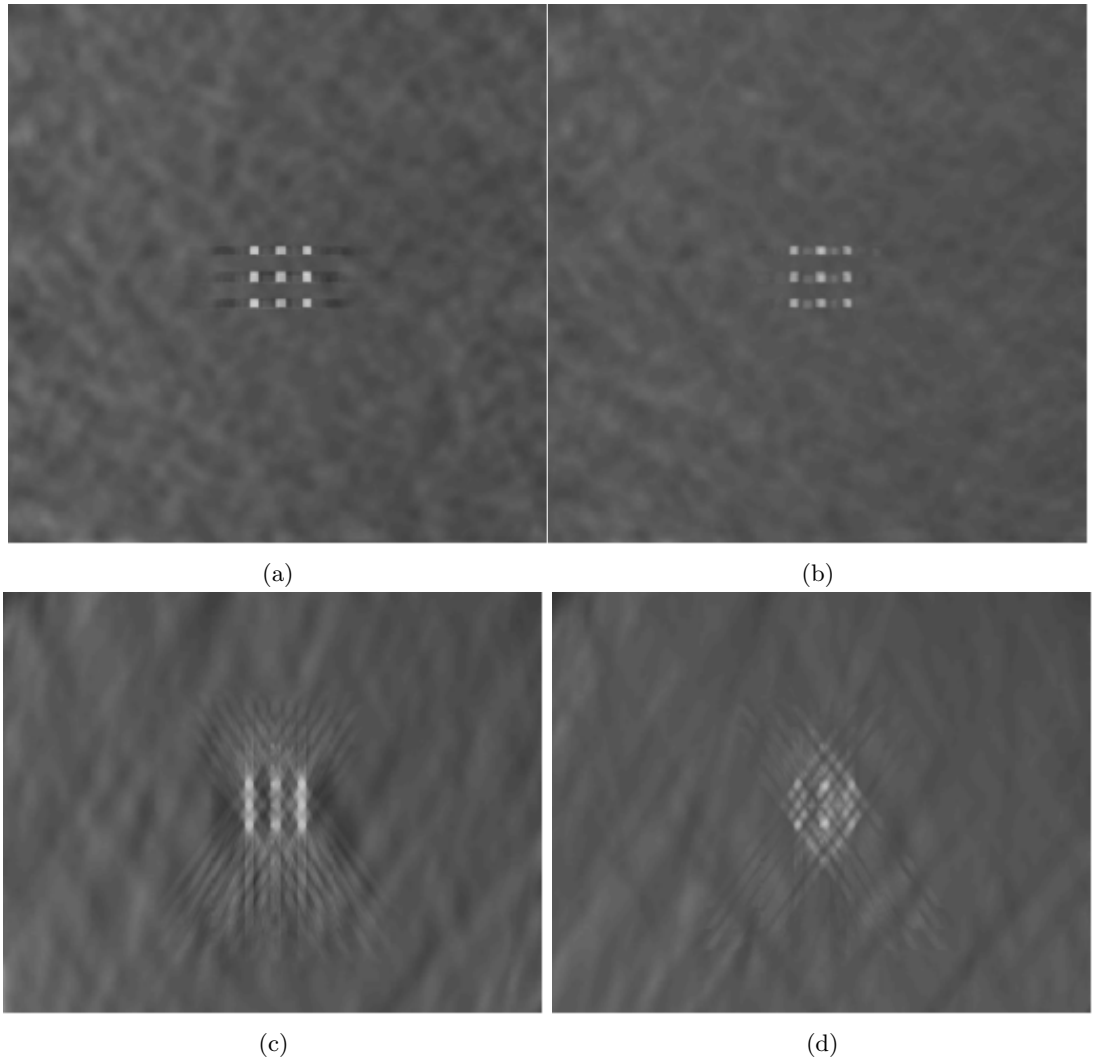

(a) (b)

(c) (d)

Figure 3.12: Reconstructed central slices of Phantom C with simulated cluster of microcalcifications: (a) central slice in X-Y plane, reconstructed with ML-SBS, (b) central slice in X-Y plane, results of MLPV-MSS, (c) central slice in X-Z plane, reconstructed with ML-SBS, (d) central slice in X-Z plane, results of MLPV-MSS. Window and level settings are the same on all views.

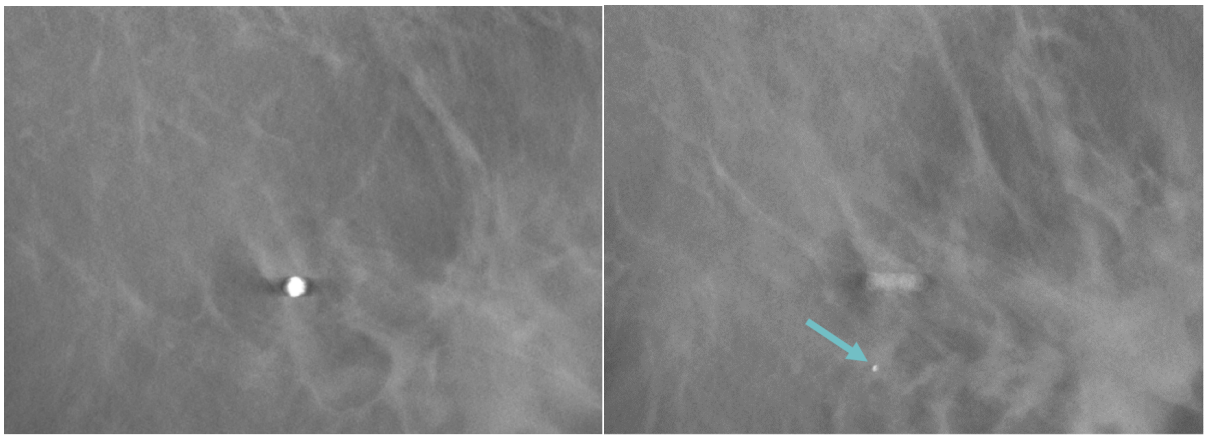

(a) SART, Z = 20 mm

(b) SART, Z = 28 mm

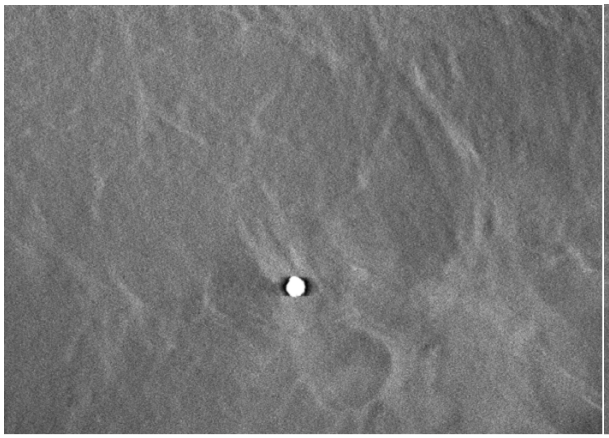

(c) ML, Z = 20 mm

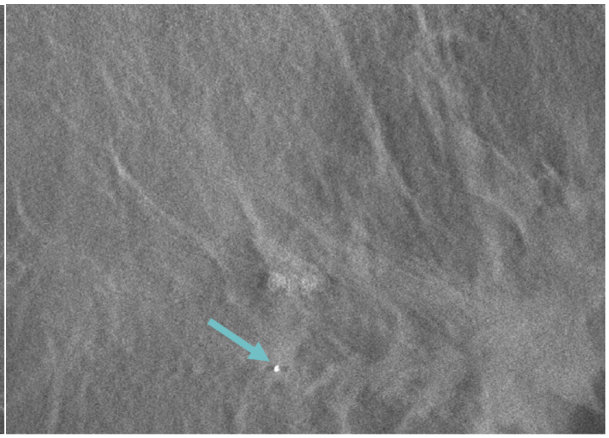

(d) ML, Z = 28 mm

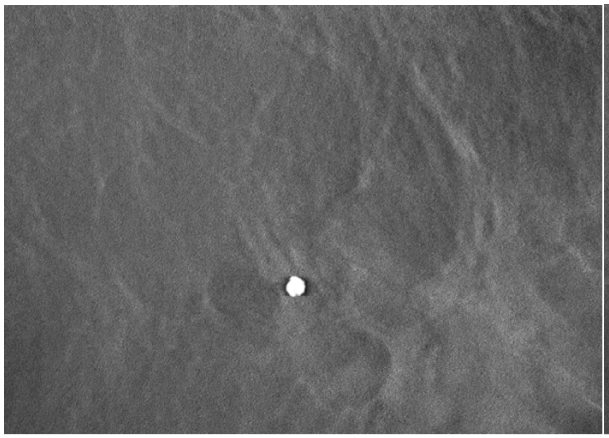

(e) MLPV, Z = 20 mm

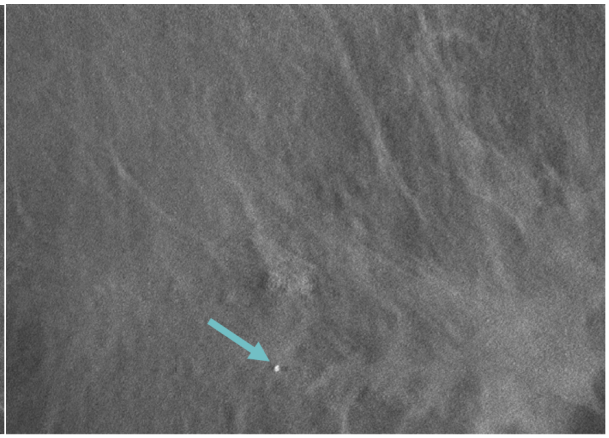

(f) MLPV, Z = 28 mm

Figure 3.13: DBT slices of a clinical case showing reconstruction artifacts caused by calcifications at various depth, reconstructed by various algorithm: (a, b) SART, step-by-step, (c, d) ML, step-by-step, (e, f) MLPV, max-scope-swing. Images at left show a large calcification at 20 mm depth, while images at right show out of plane artifacts at 28 mm depth as well as a microcalcification (arrow) in that plane.

the SART and ML algorithm with step-by-step sequence (Figure 3.14a and Figure 3.14b), the blurred structure was spread to out-of-focus planes along the line made by the x-ray source and the high intensity calcification for each projection angle. These replications were mainly suppressed in the MLPV with the side-to-side sequence (Figure 3.14c) or with the max-scope-swing (Figure 3.14d) scheme, however the repeated usage of the two projections in the MSS scheme at the extreme angles inevitably brings artifacts at these two angles.

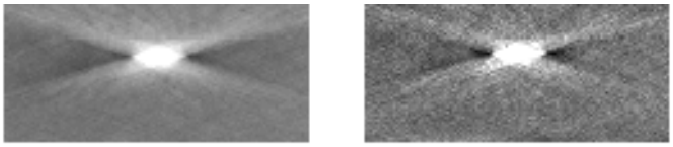

(a) SART, SBS

(b) ML, SBS

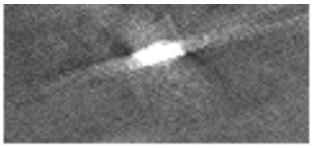

(c) MLPV, S2S

(d) MLPV, MSS

Figure 3.14: Artifacts in X-Z plane (large calcification from Figure 3.13) for various algorithms: (a) SART, step-by-step, (b) ML, step-by-step, (c) MLPV, side-to-side, (d) MLPV, max-scope-swing.

3.6 Discussion

Iterative reconstruction algorithms, such as SART and ML can be proven to converge and this has been done by Jiang [85] and Lange [86, 31]. Our reconstruction method is essentially an adaptive hybrid of a simple SART or ML reconstruction and a more complex algorithm incorporating ordered subset pairs. Rigorous proof of convergence for our approach is challenging, however, empirically, as seen in Figure 3.5a, we have consistently found that the reconstructions converge. This behavior has persisted over thousands of simulated images. Clearly, we have not explored the entire image space and it is possible that extreme cases may exist where convergence would not occur.

3.7 Conclusions

The conventional step-by-step method provided the lowest performance in contrast, distribution of artifacts and lesion detectability in reconstruction. The image quality index for the side-to-side scheme progressively increased after more iterations (shown in Figure 3.5), however it produces obvious artifacts in the X-Z plane (illustrated in Figure 3.14), and leads to less depth resolution in the Z direction. The max-scope-swing (MSS) sequence is the best of those paired schemes in central slice image quality and the spread of the artifacts in slices. It also provides a clearer edge of the object in the reconstruction (Figure 3.14). For lesions larger than 2 mm of diameter in Phantom A, the MSS scheme performs better than the other two sequences in contrast restoration and SBS the worst. Comparing to SART results, the contrast achieved in MLPV with MSS is higher for lesions of 4 mm in diameter and improved even more for larger lesions. Similar behavior has been observed in more realistic phantoms B and C which incorporated complex anatomic background, as well as in clinical cases. The ordered sequences

have better image quality of the reconstructed slices, and have fewer artifacts spread in the Z direction. A simple sequence like "side-to-side (S2S)" would achieve better reconstructed image quality than the conventional "step-by-step (SBS)" method. The constrained paired-view scheme can be easily combined and incorporated with other iterative algorithms such as the ASD-POCS step in the total p variation (TpV) method used in Sidky's work [92]. One of the limitations of this work is that the image quality indices studied in this work, especially the detectability, are all based on 2D images. Considering the slices reconstructed in tomosynthesis and the way these images are read by radiologist, a 3D image quality metric might be more relevant and further investigation is required. However the non-uniform resolution of the thick slices makes it more complicated for such a 3D detectability index calculation. The detectability test is also limited in this work because only a single spherical lesion and some idealized microcalcifications were simulated, and the detection task is a simple signal-known-exactly, location-know-exactly imaging task, which makes the finding less clinically relevant for diagnosis and detection tasks. However, the artifact-removal technique could be very useful in situations with the presence of high attenuation objects such as biopsy needles.

Chapter 4

Dose Reduction by Patch-based Denoising in Tomosynthesis Reconstruction

4.1 Introduction

As described in section 1.2, digital breast tomosynthesis (DBT) is an x-ray acquisition and processing technique which is based on a set of projection images acquired over a range of angles. From the reconstruction of the projection images a series of cross-sectional images or slices is obtained. The advantage of DBT over conventional mammography is that much of the effect of superposition of the anatomic structures that occurs over the thickness of the breast is suppressed in the slice images. Resolving the depth in the image to a selected slice eliminates some of the image complexity caused by structures at other depths and can, therefore, enhance the conspicuity of a tumour as well as facilitate spatial localization within the breast. Moreover, the systems are designed to operate such that the patient does not incur additional radiation dose compared to mammography. In current DBT imaging, one acquires data with a small number of projection views with approximately the equivalent total radiation dose of a standard two-view mammography exam.

However, the reconstruction of a 3D breast volume is challenging in DBT (discussed in section 3.1), because the dataset is sparse and/or noisy; only a limited number of low-dose projections are acquired over an arc. Consequently, spatial resolution through the thickness of the breast (z-direction) is typically inferior to the resolution within the plane of the detector (xy plane). Iterative methods for calculating the reconstruction are preferred when projections are sparse, noisy, or when sampling is nonuniform. Progress has recently been made on image reconstruction from limited-view data, which can potentially allow reduction of the radiation dose [92]. For cases where data are highly sparse, such as when only a few (*e.g.* < 10) projections are available, accurate image reconstruction becomes more difficult.

It is desirable to achieve an appropriate level of image quality while keeping the radiation dose as low as reasonably achievable in DBT. The purpose of this Chapter is to examine the effectiveness of a patch-based denoising algorithm in reducing noise while preserving details in DBT reconstruction. Low-dose DBT projection images were simulated with various levels of entrance exposure, based on the

stochastic property of incident photons from the X-ray source. The patch-based algorithm estimates the true value of a pixel as a weighted average of all pixels in the projection image, where the weights depend on the similarity between the patches.

4.2 Methods

Following the same method described in subsection 3.2.1, the acquisition of the digital breast tomosynthesis was simulated for a partial-isocentric geometry. In the simulation, the detector remains stationary while the x-ray tube rotates around a pivot point. Nine (9) projections are taken over an angular range of $-20°$ to 20, at $5°$ increments, using monoenergetic (20 keV) x-rays. A series of mathematical phantoms representing the compressed breast was created with a uniform compositional distribution of 50% fibroglandular and 50% adipose tissue as back-ground. These phantoms are rectangular prisms in shape and each contains a simulated small tumour with various diameters (from 0.6 mm to 8 mm) at the centre. The attenuation coefficients of the simulated tumours are equivalent to those measured for infiltrating ductal carcinoma (IDC) by Johns and Yaffe [11]. We investigated performance at three levels of entrance air KERMA per projection (corresponding to entrance exposures of 0.1 R, 1 R). In addition, a quantum noise-free condition was modeled (implying infinite dose). In each case, the radiation was evenly distributed among the projections in the DBT simulation.

4.2.1 Patch-based Denoising Algorithm

A patch-based algorithm was used to suppress the random variations of pixel intensity in the projection views before reconstruction. Patches of an image are simple objects defined as local square neighborhood regions of image pixels. Compared to pixel-based algorithms, patch-based methods are more powerful because, unlike individual pixels, image patches can contain relatively large-scale structures and textures present in natural images. The patch $P^I_{(x,y)}$ located at pixel $p(x,y)$ on the grey image I is defined as the set of image intensities belonging to a spatially discretized local $m \times m$ neighborhood region of I centered at pixel (x,y). The size m is usually chosen to be an odd number, *i.e.* $m = 2n+1$ (n is a natural number). Therefore, a patch $P^I_{(x,y)}$ can be ordered in an m^2-dimensional vector as:

$$P^I_{(x,y)} = \Big(I_{(x-n,y-n)}, \cdots, I_{(x+n,y+n)}\Big)^T. \tag{4.1}$$

Similar to the Non-Local Means scheme [93], our denoising algorithm estimates the true intensity value of a pixel p as a weighted average of all patches in the projection image, where the weights depend on the similarity (both structural and intensity-based) between the patches. A mathematical form of the weighting factor is given as following,

$$w(p,q) = \frac{1}{W_p}\sum_{q\in S} exp\Big(-\frac{\|p-q\|^2}{2\sigma_s^2}\Big) exp\left(-\frac{\left\|P_p^{I_{noisy}} - P_q^{I_{noisy}}\right\|^2}{2\sigma_r^2}\right), \tag{4.2}$$

where p and q are the coordinates of any pixel located within the noisy image S and $\|\cdot\|$ indicates the L_2 norm. Compared with the local smoothing or filtering methods, patch-based techniques can reduce noise while preserving details.

4.2.2 Image Acquisition and Reconstruction

An iterative reconstruction method, the paired-view maximum likelihood convex (MLPV) described in subsection 3.3.3, has been implemented for image reconstruction. The contrast (Equation 3.5), lesion signal-difference-to-noise ratio (SDNR, Equation 3.6) and detectability (Equation 3.7) were used as FOMs to evaluate the image quality in the reconstructed slices.

Images were acquired on a digital mammography unit Senographe DS (GE Healthcare, Chalfont St. Giles, UK) system for testing the denoising algorithm in projection views. In addition, a 5-cm-thick biopsy phantom was imaged with anode/filter combination of Rh/Rh, at 29 kV and 4 mAs to produce a noisy image. The proposed method has been also tested on the projection images for a clinical DBT exam.

4.3 Results

4.3.1 Biopsy Phantom

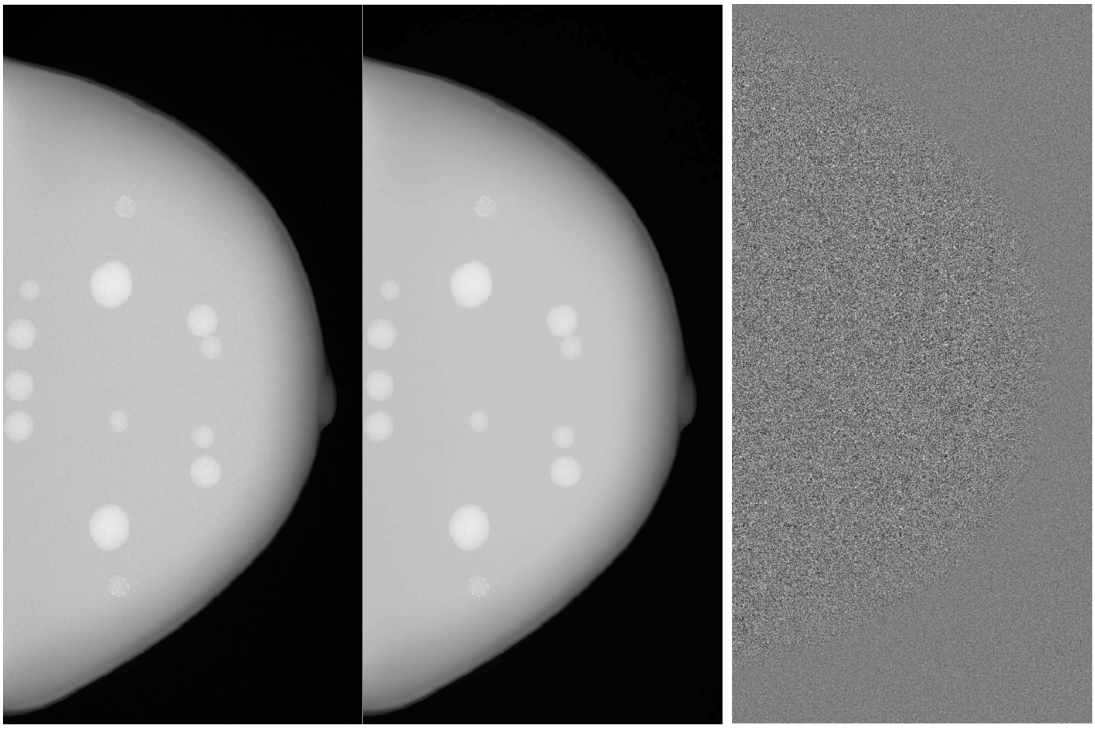

(a) (b) (c)

Figure 4.1: Projection image of a biopsy phantom before and after denoising: (a) Original projection image of a biopsy phantom, (b) Projection image of the phantom denoised by the patch-based technique, (c) Difference image displayed in the gray scale window of [-0.1, 0.1].

Digital images of the biopsy phantom, acquired at a very low exposure (4 mAs), were first converted and normalized to a log-compressed image, in which the intensity of each pixel is the sum of x-ray attenuation coefficients along the x-ray path, shown in Figure 4.1a. The denoised version of the projection image by the patch-based algorithm is shown in Figure 4.1b and the difference between the original and

the denoised projection is shown in Figure 4.1c. The suppressed noise appears like white noise with different intensities in the phantom area and the background, consistent with the quantum noise in mammography being content dependent.

A profile of the image of the biopsy phantom along one column is plotted in Figure 4.2a. As expected, the fine details in the image were preserved while random noise was removed. The noise power spectrum (NPS) measured by the multitaper method (Equation 2.6)[40] for the difference image (Figure 4.1c) between the original and the denoised projection view of the biopsy phantom is shown in Figure 4.2b. The NPS of the difference image approaches that of the noisy projection above 2 mm^{-1}, suggesting that the original projection of the phantom was dominated by quantum noise for higher frequencies. The suppressed noise resembled white noise for a wide range of frequencies while, as desired, the lower frequencies (< 2 mm^{-1}), which contain more information about the main structures of the phantom are removed to a much lesser extent.

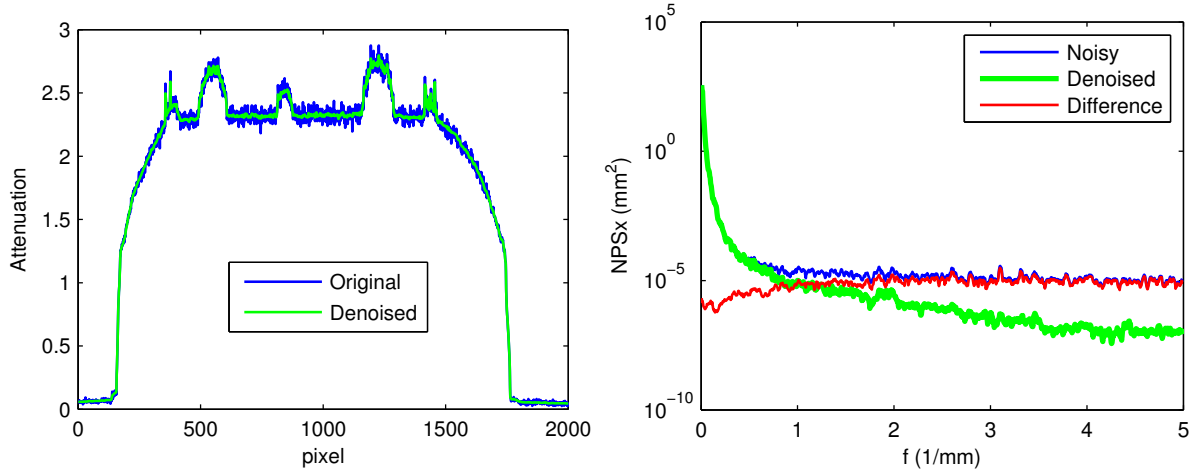

(a) (b)

Figure 4.2: (a) Profiles of the original and denoised projection image of a biopsy phantom, (b) Power spectra of the projection, the denoised image and the difference.

4.3.2 Clinical Mammograms

The proposed method was also applied to de-identified screening mammograms (courtesy Dr. Roberta Jong, Sunnybrook Health Sciences Centre), as in Figure 4.3a. The denoised projection image by the patch-based algorithm is shown in Figure 4.3b and the difference between the original and the denoised projection is shown in Figure 4.3c. The suppressed noise appears like white noise. Neither anatomic details nor any microcalcifications were observed in the difference image.

A profile of the mammogram along one column through several microcalcifications is plotted in Figure 4.4a. As expected, the fine details in the image were preserved while random noise was removed. The power spectra of the difference image (Figure 4.3c) between the original and the denoised projection view of the breast are shown in Figure 4.4b. The NPS of the difference image approaches that of the noisy projection above 3 mm^{-1}, indicating that the original mammogram was dominated by quantum noise for higher frequencies. The suppressed noise is essentially white for a wide range of frequencies and, the lower frequencies (< 3 mm^{-1}), which contain most of the information about the anatomic

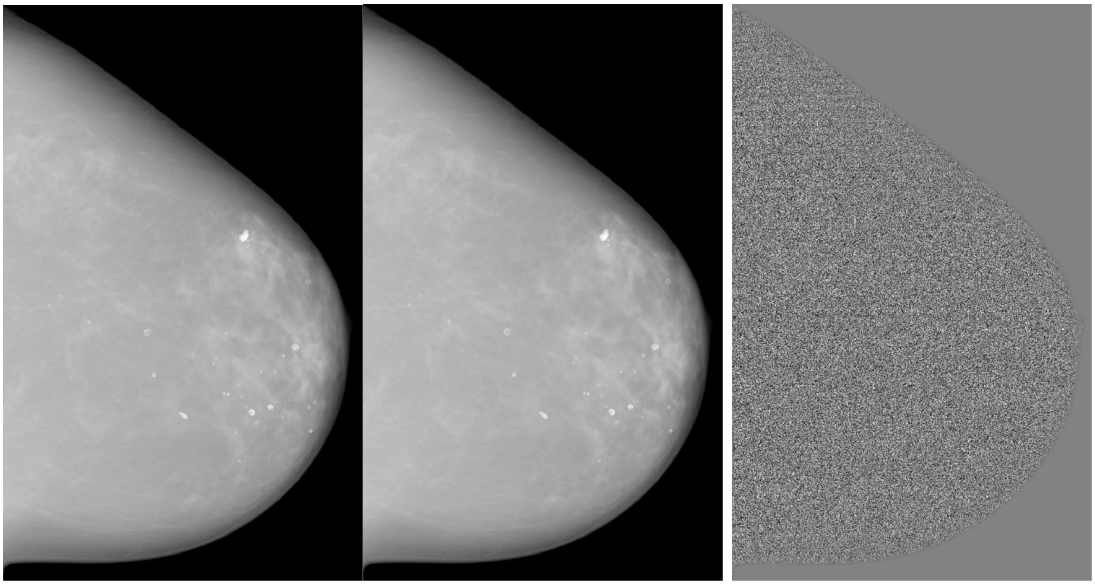

(a) (b) (c)

Figure 4.3: Mammogram before and after denoising: (a) Original screening mammogram, (b) Mammogram denoised by the patch-based technique, (c) Difference image displayed in the gray scale window of [-0.02, 0.02].

structures of the breast are removed to a much less extent. The cause of the peak near the frequency of 3.5 mm^{-1} in the NPS of the original mammogram is believed to be the improper cancellation of the anti-scatter grid during flat-fielding [40], which can be completely eliminated by our denoising algorithm as demonstrated in the noise component of the difference image shown in Figure 4.4b (arrow). The removal of the anti-scatter grid effect is also obvious in Figure 4.3c. This implies that our proposed patch-based denoising method could also be a powerful candidate for flat-fielding and pre-processing for projection images.

4.3.3 Clinical DBT Exam, Projection Image

The proposed method was also applied to the projection views of a clinical DBT exam, one of which was shown in Figure 4.5a. The denoised version of the projection image by the patch-based algorithm was shown in Figure 4.5b and the difference between the original and the denoised projection was shown in Figure 4.5c. The suppressed noise appears like white noise with different intensities in the breast area and the air region in background, which agrees with the fact that the quantum noise in mammography is content dependent. Virtually no anatomic detail was observed in the difference image.

A profile of the DBT projection along one column is plotted in Figure 4.6a. As expected, the fine details in the image were preserved while random noise was removed. The power spectra of the noisy projection, the denoised version and the difference image (Figure 4.5c) between the two of the DBT projection is shown in Figure 4.6b. The NPS of the difference image approaches that of the noisy projection after the frequency of 2.5 mm^{-1}, which indicates that the original DBT projection was dominated by quantum noise for higher frequencies. Comparing to the NPS of the mammogram shown in Figure 4.4b, more random noise appeared in the DBT projection image because less radiation dose was employed to each view to keep the total dose at the same level of one mammography exam. The

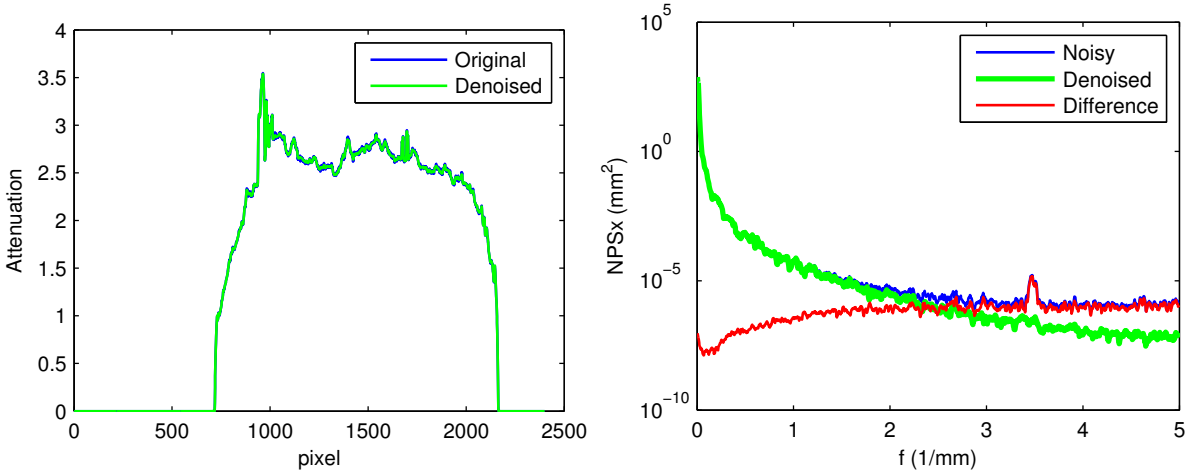

(a) (b)

Figure 4.4: (a) Profiles of the original and denoised mammogram, (b) Power spectra of the mammogram, the denoised image and the difference.

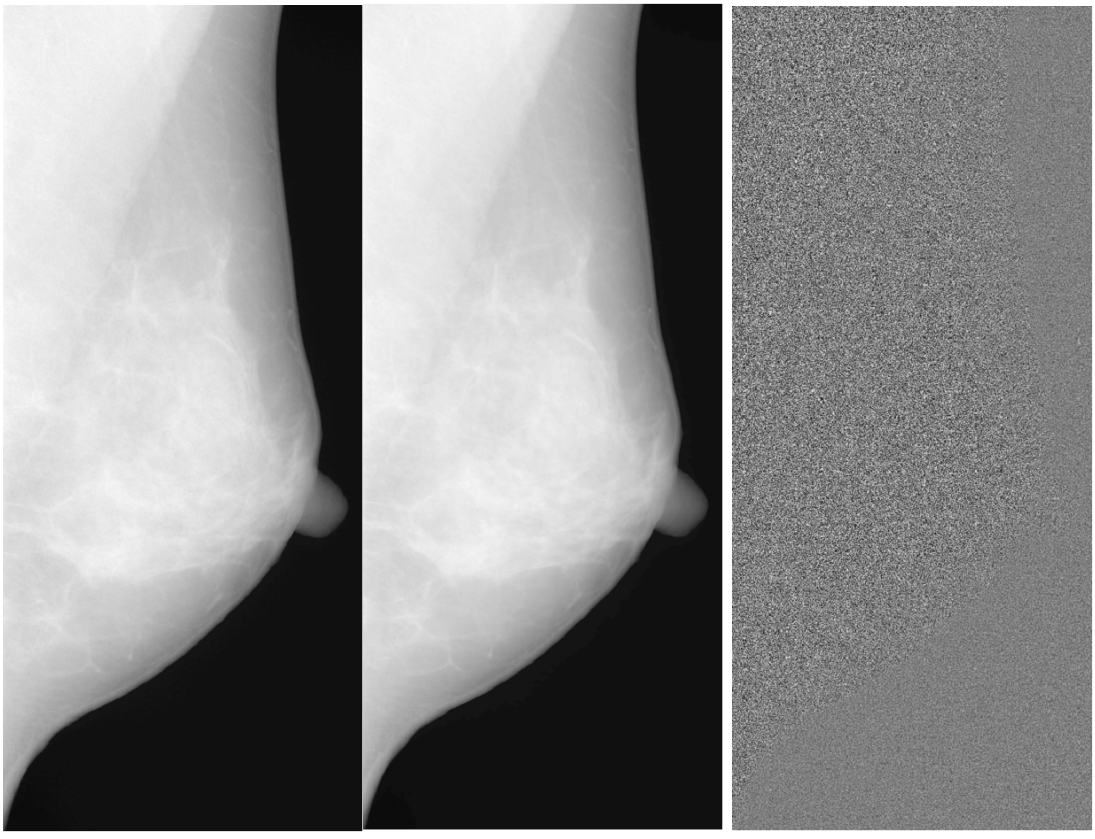

(a) (b) (c)

Figure 4.5: Projection view of a clinical DBT exam before and after denoising: (a) Original projection view of a clinical DBT exam, (b) Projection view of the DBT exam denoised by the patch-based technique, (c) Noise component, displayed in the gray scale window of [-0.05, 0.05].

suppressed noise resembled the white noise for higher frequencies and, as desired, the lower frequencies (< 2.5 mm^{-1}), which contain most information about the anatomic structures of the DBT projection are removed to a much lesser extent.

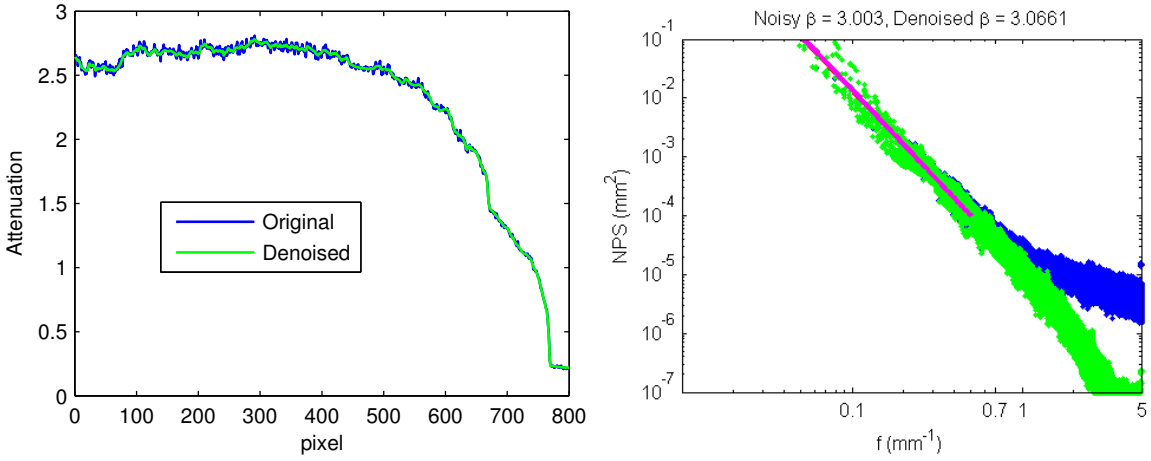

(a) (b)

Figure 4.6: (a) Profiles of the original and denoised projection image of a DBT exam, (b) Power spectra of the ROI in the DBT projection and the denoised image, β is maintained by denoising.

4.3.4 Simulation of Uniform Phantoms

The image quality was evaluated in terms of the contrast and the lesion SDNR in the reconstructed central slices in the simulated phantoms with uniform background. For example, results for a 2 mm diameter lesion are shown as a function of reconstruction iteration numbers in Figure 4.7a and Figure 4.7b. Both the contrast and lesion SDNR were enhanced by the denoising technique for the two levels of the entrance exposure simulated in the DBT projections. On average, the contrast is increased by 16.6% and 12.2% for 0.1 R and 1 R per projection respectively. The lesion SDNR is increased by 131.8% and 76.4% on average for 0.1 R and 1R respectively. More importantly, the contrast of the 0.1 R exposure image was boosted by denoising to almost the same performance as obtained at 1 R without denoising. This shows a great potential of the integration of patch-based denoising in low-dose DBT reconstructions for low contrast objects, such as mass tumours.

4.3.5 Reconstructed Slices of Clinical DBT Exam

To evaluate the performance of the patch-based denoising algorithm on DBT reconstruction, the proposed method has been applied to the projection images of a clinical DBT exam. The comparison images are shown side-by-side in Figure 4.8: The original reconstructed slice using raw projections is shown in Figure 4.8a, the same slice reconstructed using denoised projections is shown in Figure 4.8b, and the difference between these two is shown in Figure 4.8c.

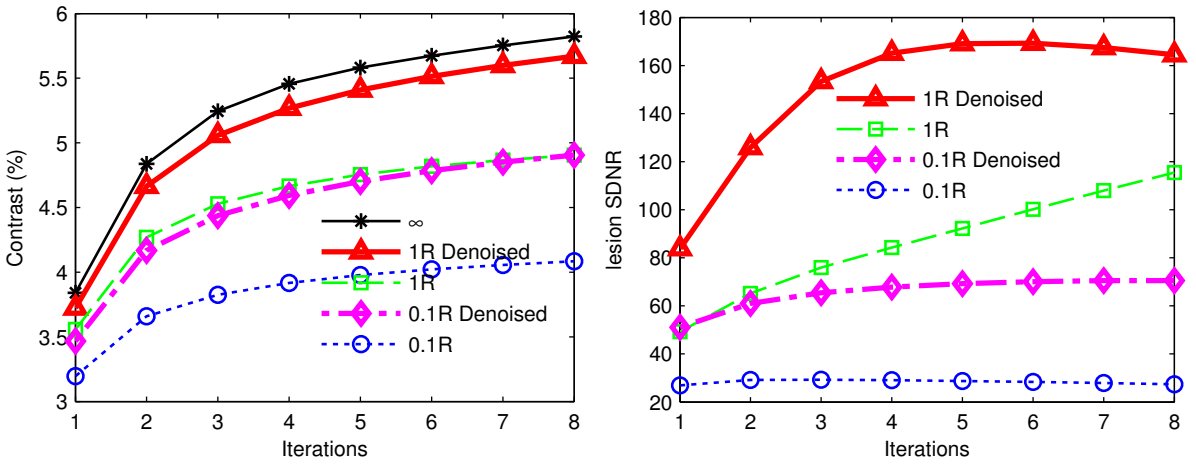

(a) (b)

Figure 4.7: Image quality of reconstructed slices in simulated uniform phantom: (a) Contrast enhanced in the reconstructed slices by the patch-based denoising tech-nique for both levels of exposure, (b) The lesion SDNRs in the reconstructed slices were increased by the denoising tech-nique for both levels of exposure.

4.4 Discussion and Conclusions

Results from the biopsy phantom, the screening mammogram and the clinical DBT projection data demonstrated that the proposed technique effectively reduces noise while preserving most fine details in DBT. The suppressed noise appears like white noise and virtually no anatomic details or microcalcifications were observed in the difference image. It also implies that our proposed patch-based denoising method could be a powerful candidate tool for flat-fielding and pre-processing projection images. The preliminary results from the simulated phantom study have demonstrated that the image quality of DBT can potentially be improved by the proposed technique by incorporating appropriate denoising into the iterative reconstruction algorithm. Further investigation will be carried on images with heterogeneous background such as anatomic clusters in both simulation phantoms and patient data in clinical DBT exams.

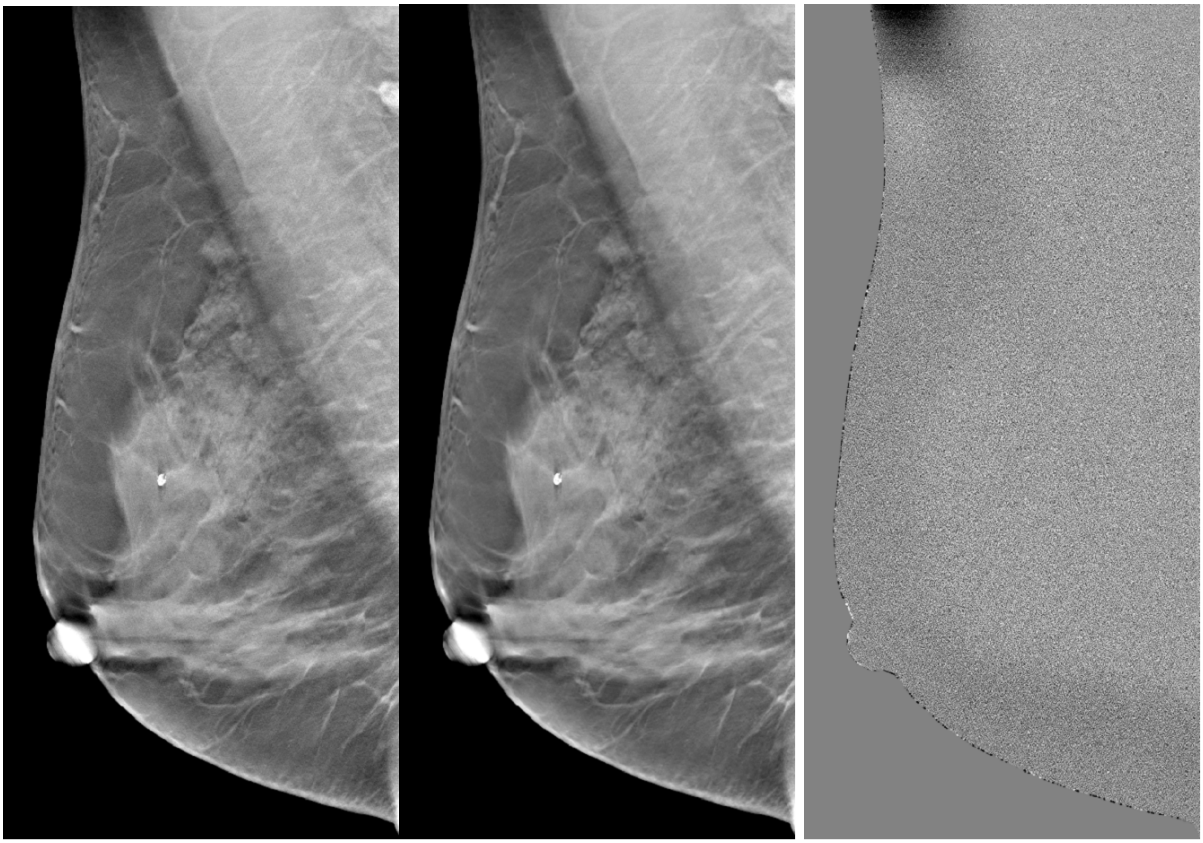

(a) (b) (c)

Figure 4.8: Reconstructed slices of a clinical DBT exam using noisy projections and denoised projections: (a) Reconstructed slice using noisy projections, (b) The same slice reconstructed using denoised projections, (c) Difference between the previous two images, displayed in the gray scale window of [-50, 50].

Chapter 5

Summary and Future Work

5.1 Summary

In this thesis, the optimization of DBT image quality has been studied in three relevant areas. First in the assessment of image quality and measurement of detectability index, the development of a better power spectrum estimator using multitaper method is demonstrated in Chapter 2. The proposed multitaper approach has been proved to be superior to the conventional single taper methods in the prevention of spectrum leakage, variance reduction, and maintenance of finer frequency precision. Therefore the multitaper method yields to a more accurate estimate of the power spectrum of image signal and background noise, and a better image quality FOM which plays an important role in later optimization.

Next in the image reconstruction of DBT, a new constrained paired-view technique has been explored in Chapter 3. The paired-view method is incorporated with iterative DBT reconstruction, which reduces reconstruction artifacts spreading to out-of-plane slices. The conspicuity of potential lesions is therefore enhanced with less distortion and improved detectability.

Later in Chapter 4 the random noise in DBT acquisition and reconstruction has been investigated. A patch-based denoising algorithm is applied on projection views before reconstruction and slices afterwards. Random noise was suppressed substantially while the anatomic details which contain relevant information were maintained. The detectability is further increased with less noise appearance.

5.2 Future Work

As discussed in Chapter 2, estimation of the image power spectrum is fundamental to the development of a figure of merit for image performance analysis. In this Chapter (section 5.3), we briefly investigate a new multitaper approach to determine power spectra, which provides a combination of low variance and high spectral resolution in the frequency range of interest. To further reduce the variance, the spectrum estimated by the proposed local spectral adaptive multitaper method (LSAMTM) is subsequently smoothed in the frequency domain by bilateral filtering, while keeping the spectral resolution intact. This tool will be especially valuable in power spectrum estimation of images that deviate significantly from uniform white noise.

The performance of this approach was evaluated in terms of spectral stability, variance reduction, bias and frequency precision. It was also compared to the conventional power spectrum method in several

typical situations, including the noise power spectra (NPS) measurements of simulated projection images of a uniform phantom and NPS measurement of real detector images of a uniform phantom for two clinical digital mammography systems.

Examination of variance reduction versus spectral resolution and bias indicates that the LSAMTM with bilateral filtering technique is superior to the conventional estimation methods in variance reduction, spectral resolution and in the prevention of spectrum leakage. It has the ability to maintain both low variance and narrow spectral linewidth in the frequency range of interest. Up to 87% more variance reduction can be achieved with proper filtration and no sacrifice of frequency precision has been observed.

The reconstruction of DBT can be further improved in two main categories: the accuracy of reconstruction and the speed of convergence. Both require more efficient algorithms to retrieve information acquired in the 2D projection views and to render into a volumetric representation of the breast. Later in this Chapter (section 5.4), we will continue our investigation on tomosynthesis reconstruction by introducing some spherically symmetric basis functions (blobs), which are alternatives to the more conventional cubic voxels for image reconstruction in breast tomosynthesis. The volume representation and its projection views (PV) are essential components of iterative algorithms for image reconstruction from data collected from an area detector. This Chapter addresses the forward projection and backprojection process of three-dimensional (3D) breast reconstruction obtained from cone-beam scans using tomosynthesis imaging equipment. The smoothness of the blob elements allows more realistic modeling of the breast, and the rotational symmetry of the elements leads to more efficient calculation of both directional projection of the represented volume, as required in iterative reconstruction techniques. The combination of blob volume elements and the projection matrix method improves tomosynthesis reconstruction in both accuracy and speed.

5.3 Local Spectral Adaptive Multitaper Method (LSAMTM)

The power spectrum of a digital mammogram provides information about the quality of the image acquisition and reconstruction, as well as properties of the breast tissue itself. It is desirable to obtain an accurate and stable spectrum, with little or no bias and small uncertainties. The multitaper method (MTM) was introduced [44] in Chapter 2 to reduce the large variance in estimation that commonly exists in conventional single taper periodograms. In that work we demonstrated that the MTM method is superior to the conventional windowed overlapping averaging (WOAP) method in terms of bias, variance and frequency precision in power spectrum estimation of breast images [40]. The variance reduction of the MTM method is achieved by averaging the periodograms of an image weighted by a series of window functions (also known as tapers). This generates a smooth final estimate with less variance than a single taper method and meanwhile reduces bias by preventing spectral leakage. Spectral leakage is the misrepresentation of components other than integer multiples of the fundamental frequency (which equals the frequency increment in the calculated spectrum). This effect is inevitable for images with limited extent and limited pixel size, but can be reduced by weighting the data with a suitable window function, which tapers the signal level at the edge of the image to zero such that when the FFT is evaluated, the edge discontinuities are minimized. These window functions do not substantially change the spectrum, but they tend to minimize the broadening of the spectrum. The application of tapers affects the bias, variance and spectral resolution of the estimates, a smooth and stable result with low bias is desirable in power spectrum estimation.

The MTM exploits a number of good leakage-resistant tapers rather than only one. The image information discarded by one taper is partially reclaimed by other tapers. However each taper is more sensitive to structures at a certain frequency, therefore, the spectral resolution is degraded in averaging and the spectral linewidth is increased with the number of tapers used. The spectral linewidth (FWHM) measures the ability of the spectrum to represent the fine structure of the frequency property of the image. Here we present a new approach to determine power spectra which combines the low variance and high spectral resolution near the frequency of interest. To further reduce the variance while keeping the frequency precision intact, the spectrum estimated by the proposed LSAMTM is subsequently smoothed in frequency domain by bilateral filtering [94].

5.3.1 Summary of Multitaper Method (MTM)

As described in Chapter 2, the multitaper method for power spectrum estimation consists of the following steps:

1. From image, I, subtract the mean or optionally detrend the image for large scale variations of higher order (*e.g.* subtract a polynomial surface)
2. Multiply the detrended image, ΔI, with multiple window function, $w_{ij}(x, y)$ to reduce spectral leakage.
3. Compute the discrete Fourier transform (DFT) for each weighted image
4. Compute the raw periodogram for each weighted image
5. Average the periodograms to get the estimated spectrum

This algorithm is summarized mathematically in Equation 2.6. Unlike Slepian tapers which are also used in some MTM methods [95], sinusoidal tapers have no optional linewidth parameter, and the linewidth of the spectral estimation is determined only by the number of tapers used.

5.3.2 Choosing Number of Tapers Adaptively

The trade-off of spectral resolution versus variance reduction shows that fewer tapers should be used when the spectrum varies more rapidly [58]. By using more or fewer tapers, a multitaper estimate with the optimal convergence properties of kernel smoothers can be constructed.

A simple and fast implementation of the LSAMTM as used in our work is described here. First, the power spectrum of the input image is estimated by the normal MTM with adequate number (*e.g.* 7×7) of tapers. This results in a power spectrum S_1, which has relatively low variance and small bias in slowly changing regions and broadened peaks with reduced heights. Meanwhile, the power spectrum of the input image can be estimated by the normal MTM with few (*e.g.* 2×2) tapers or even only 1×1 taper. This creates another power spectrum, S_2, which has overall large variance and fluctuates wildly in general, but, maintains good spectral resolution with narrow-linewidth peaks. Next, the peak regions are identified either manually or automatically with the help of an isotropic edge detection filter M_p, which is an enhanced Laplacian mask using the second order derivative of S_1. Later, a final estimation of the power spectrum is obtained as a combination of the smooth and flat part of S_1 with precise peaks from S_2, according to the segregation mask (derivatives mask M_p) of the spectrum.

5.3.3 Bilateral Filtered LSAMTM

It also has been shown that smoothing a periodogram [96] by filtering in the frequency domain is among many viable alternative methods available for spectrum estimation. However, the proper amount of smoothing depends on the characteristics of data, and the tradeoffs among smoothness, stability and resolution should be considered in selecting filtering parameters. Here we have selected bilateral filtering to further reduce variance and preserve the spectral resolution achieved in LSAMTM.

Bilateral filtering is an anisotropic edge-preserving filtering technique [97]. The intensity value at each pixel is replaced by a weighted average of intensity values from nearby pixels. It extends the traditional linear Gaussian smoothing by weighting the filter coefficients not only on spatial distance but also on the pixel intensity differences. Pixels that are very different in intensity from the central pixel are less weighted even though they may be closer to the central pixel. This preserves sharp edges by systematically iterating through each pixel and adjusting weights to the adjacent pixels accordingly. It is implemented as two Gaussian filters at a localized pixel neighborhood, one in the spatial domain, and the other in the intensity domain. A mathematic approach is given as follows:

$$BF[I]_p = \frac{1}{W_p} \sum_{q \in H} exp\Big(- \frac{\|p-q\|^2}{2\sigma_s^2} \Big) exp\left(- \frac{|I_p - I_q|^2}{2\sigma_r^2} \right), \tag{5.1}$$

where p is the coordinates of the central pixel with intensity I_p, q is the coordinates of any pixel located within a neighborhood H and has an intensity of I_q. W_p is the normalization factor, σ_s is the extent of the spatial kernel, which is the considered neighborhood and σ_r is the range of the intensity kernel, which is related to the minimum amplitude of an edge that is intended to be protected. Both σ_s and σ_r determine the level of smoothness. The spatial parameter, σ_s, is usually proportional to image size. Here, a distance of 2% of the image side-length is used. The range parameter σ_r varies with applications, and should be proportional to the amplitude of the edge to be protected.

5.3.4 Simulated X-ray Projections and Clinical QC Images

To compare the spectral resolution provided for typical MTM and our new method, grid lines in projection images were simulated with coloured noise using the same method as in Chapter 2 [40]. Those grid lines will result in a peak at 2.5 mm^{-1} in the power spectrum of the simulated image.

Quality control images were taken from two digital mammography units, one Senographe DS (GE Healthcare, Chalfont St. Giles, UK) system and one Nuance Excel (Planmed Oy, Helsinki, Finland) system, for testing the LSAMTM method in NPS measurement. The "for processing" (*i.e.* unprocessed) images were used in all cases. For both machines, a 4.4 cm thick uniform PMMA slab was imaged. Ten successive images were taken on the GE system with anode/filter combination of Rh/Rh, potential at 29 kV and 80 mAs. Another ten images were acquired on the Planmed unit with the W/Ag combination, peak voltage at 30 kV and 80 mAs.

5.3.5 Preliminary Results of LSAMTM

The comparison of NPS measurement in simulated images is depicted in Figure 5.1. The results of S_2 (one sinusoidal taper) are shown as the dotted green line, which fluctuates wildly, but does demonstrate high spectral resolution near the spike (Figure 5.1b). The results of S_1 obtained with 7×7 tapers using

standard MTM are plotted as the purple dot-dash line. These exhibit less variance but have a wider linewidth and poor recovery of the peak value. The LSAMTM results as a combination of S_1 and S_2 are shown as a dashed blue line. Compared with the first two estimations, the LSAMTM resulted in smoother calculation of NPS, better restoration of the peak value and narrow linewidth at the FWHM of the peak. The final estimate, after bilateral filtering, is presented as the solid red line. The variance in the NPS is further reduced and the estimate is very close to the truth without much cost in frequency resolution.

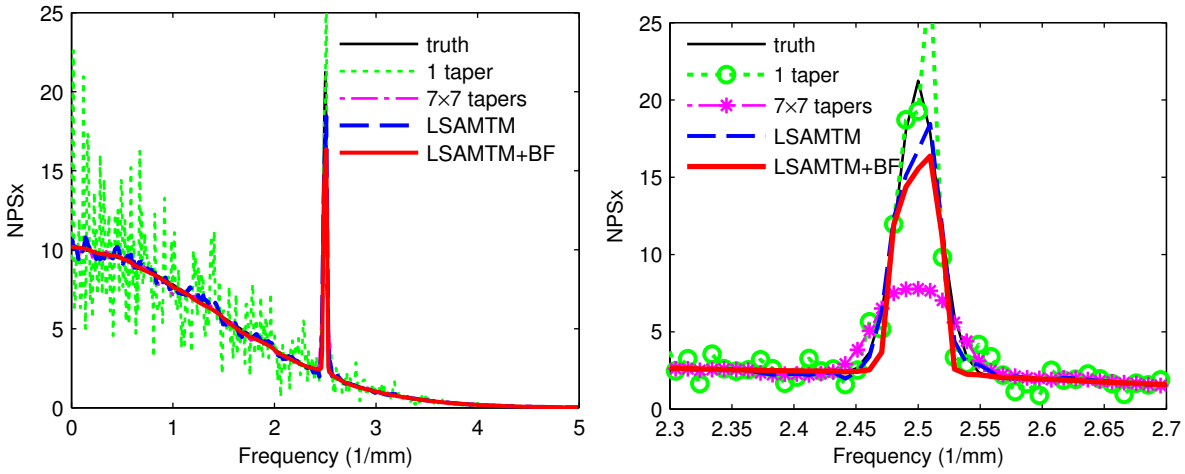

Figure 5.1: Comparison of NPS measurement in simulated images, with a peak at 2.5 mm^{-1} in coloured noise. (a) MTM results are shown as the green dot line and the purple line, LSAMTM results are plotted as a blue dashed line, and the final estimate after bilateral filtering is presented as a red solid line. (b) Zoomed view of the peak in Figure 5.1a. LSAMTM results combines the good resolution of one taper at spike and less variance in 7×7 tapers at flat areas. The variance of estimation is further reduced with additional bilateral filtering.

To investigate the performance of Bias(ϕ) and Var(ϕ) for bilateral filtering in additional to the standard MTM methods, 100 trials with coloured noise were simulated for each number of tapers ($K_x \times K_y$) used in the MTM (Equation 2.6). The number of images was varied from 20 to 100 and observed no significant changes in standard deviation. The bias and variance measured in NPS estimation by standard MTM and those filtered by BF are plotted in Figure 5.2a and Figure 5.2b, respectively; the multitaper method is plotted as a dashed line with squares and the bilateral filtering method as a solid line. In both techniques, the variance and bias of the final NPS estimation decreases as an increasing number of tapers is employed; the averaged NPS becomes smoother and more stable. With proper bilateral filtration, the variance and bias of the estimation can be further reduced. However, the bias was increased when only a small number of tapers are used as seen in Figure 5.2a. This confirmed that it is necessary to have S_1 to estimate the flat part of the spectrum. It also suggests that a reasonably large number of tapers (*e.g.* 5×5) should be used for S_1 to achieve a relatively low variance and low bias in estimation.

In Figure 5.3, the performance of spectral resolution is illustrated by the measured linewidth in the NPS estimation as a function of the number of tapers used in the multitaper method. Here, linewidth refers to the FWHM of the simulated peak in the power spectrum. When fewer tapers were used, the final

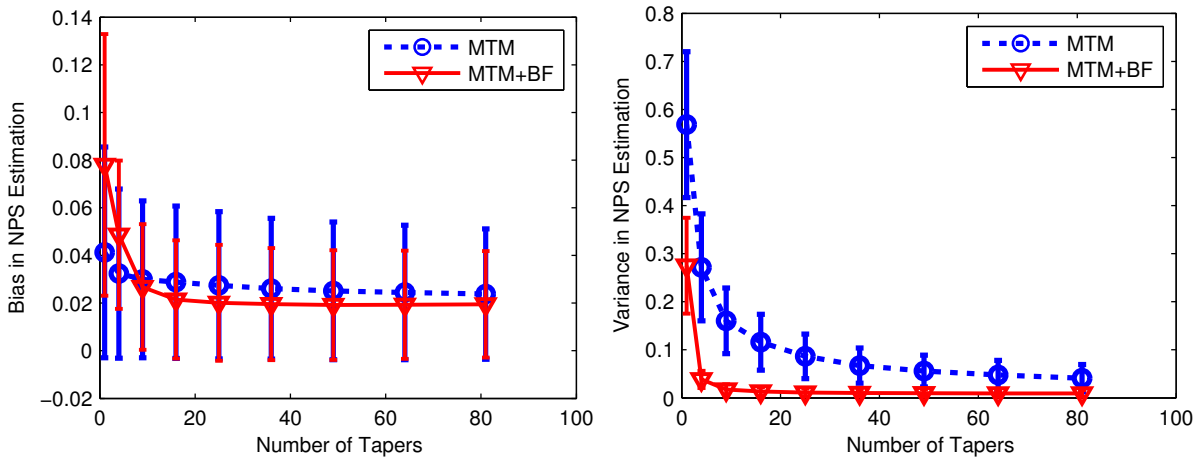

(a) (b)

Figure 5.2: (a) Comparison of the bias in NPS measurement by standard MTM with and without bilateral filtering methods. MTM results are in the blue dash line, and the final estimate after bilateral filtering is presented as a solid red line. (b) Comparison of the variance in NPS measurement by standard MTM with and without bilateral filtering methods. The variance of estimation is further reduced with additional bilateral filtering.

estimation had higher spectral resolution and less broadening of the peak. To balance the performance of variance reduction and spectral resolution in the standard MTM, more tapers should be used for a flat or smoothly changing spectrum while fewer tapers should be used for a spectrum with sharp peaks. The compromising of spectral resolution and variance reduction was largely prevented in the LSAMTM method with bilateral filtering (linewidth results are plotted as two individual error bars in Figure 5.3). The blue error bar refers to the results of 1×1 taper used in S_2, and the green one for those of 2×2 tapers. The linewidth was slightly broadened by the bilateral filtering, however, is still much narrower than for standard MTM (in which 5×5 or more tapers are commonly used).

Quality control images were acquired on a GE Tomo DS mammography unit. Ten successive images were taken in Tomo DS with anode/filter combination of Rh/Rh, potential at 29 kV and 80 mAs. The images were detrended to yield the NPS in Figure 5.4a and Figure 5.4b by subtraction from each image of the average of the ten images in the series. In power spectrum analysis, detrending is a very important operation for removing any low-frequency or gradual changes (trends) in images. If a trend is not removed properly, it will leave a high spike in the spectrum at or near zero-frequency [40]. The NPS measured by LSAMTM with bilateral filtering in the raw images is demonstrated in Figure 5.4a. The zoomed-in view of the NPS estimated by different methods in Figure 5.4b provides a more detailed look at the performance of variance reduction and spectral resolution.

In a similar manner, the NPS measured by LSAMTM with bilateral filtering in the unprocessed images acquired on a Planmed system are demonstrated in Figure 5.5a and Figure 5.5b, which is a zoomed-in view of the NPS, estimated by different methods, provides a more detailed look at the performance of variance reduction and spectral resolution. The LSAMTM with BF method is more sensitive for the spike, and tends to have less bias than the regular MTM.

In this section, we introduced a new technique to calculate power spectra of breast images. This method has the ability to provide both low variance and high spectral resolution near the frequency of

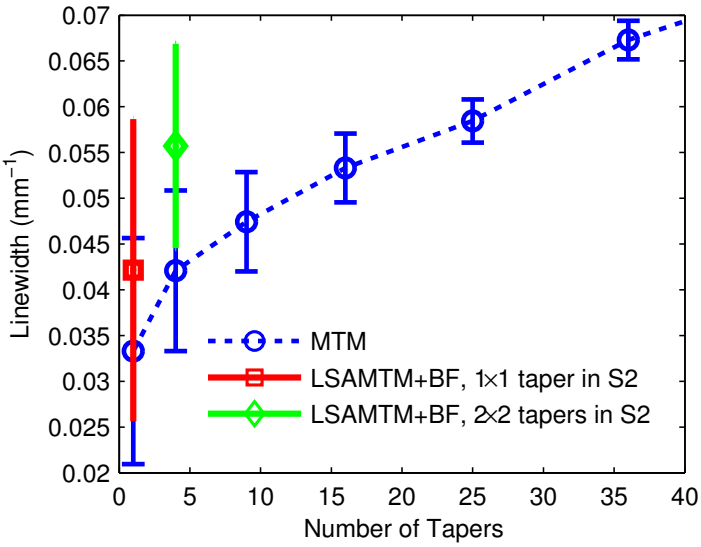

Figure 5.3: Comparison of the linewidth performance in NPS estimation by MTM and LSAMTM with BF methods. The MTM method plotted as a blue dashed line, the LSAMTM method as red and green error bars.

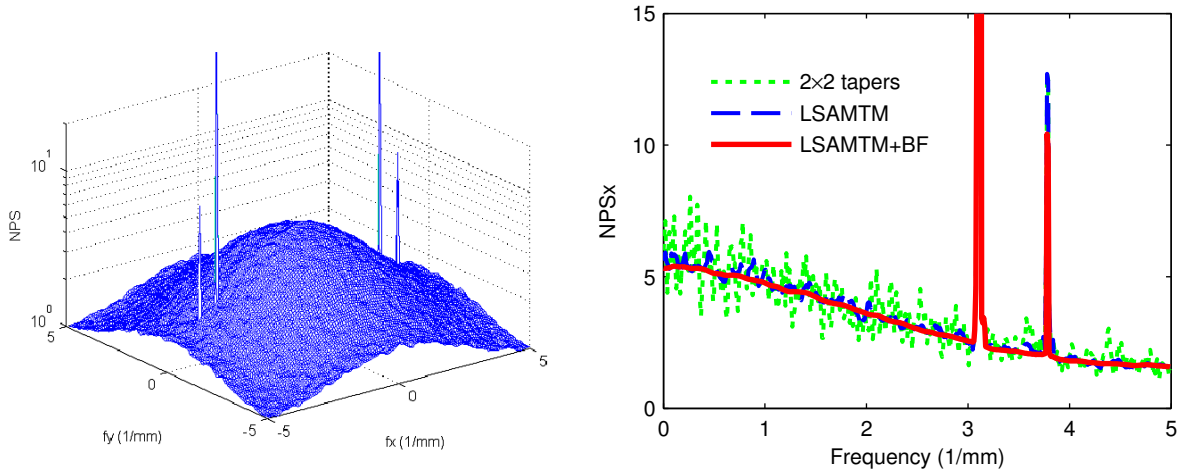

(a) (b)

Figure 5.4: (a) Measured NPS by LSAMTM with bilateral filtering in projection images, which are unprocessed images acquired in the Tomo DS system with a uniform phantom. (b) Comparison of NPS measurements. MTM results are shown as the green dotted line, LSAMTM results as a blue line and bilateral filtered results are presented as a red solid line.

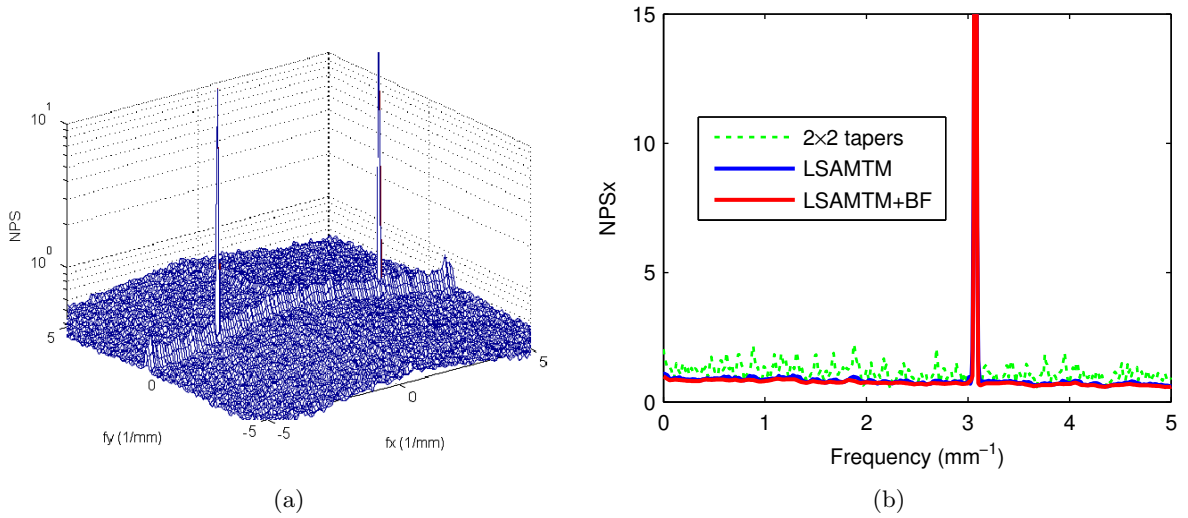

(a) (b)

Figure 5.5: (a) Measured NPS by LSAMTM with bilateral filtering in projection images, which are raw images acquired in the Planmed system with a uniform phantom. (b) Comparison of NPS measurements. MTM results are shown as the green dotted line, LSAMTM results as the blue line and bilateral filtered results are presented as a red solid line.

interest. The spectral concentration is improved due to the adaptive choice of taper number according to the flatness of the spectrum. The variance of the spectrum, estimated by LSAMTM is further reduced by bilateral filtration, without any damage of the frequency precision. The linewidth was slightly broadened by the bilateral filtering, however, is still much narrower than when the standard MTM method is used.

Because of the narrow linewidth and better prevention of spectral leakage, the signal integrity in the power spectrum of projection images is maintained even in the presence of spectral contamination due to grid-line artifacts. The proposed method is a promising technique in power spectrum analysis of radiographic images. It yields a smooth and stable estimation with both low variance and narrow linewidth, which are desirable characteristics of an ideal estimator.

5.4 Reconstruction by Blob-based Voxels

As elaborated in Chapter 3 (section 3.1), the reconstruction of a three-dimensional (3D) breast volume is challenging in DBT because the dataset may be sparse and/or noisy: only a limited number of low-dose projections are acquired over an arc. Consequently, spatial resolution through the thickness of the breast is typically inferior to the resolution within the plane of the detector (section 3.3). Iterative methods for calculating the reconstruction are preferred when projections are sparse, noisy, or when sampling is non-uniform [68]. Iterative reconstruction techniques are based on successive estimation of backprojection and forward projections of the object estimated at intermediate stages of the algorithm [98]. The computed values are based on a model of the data acquisition process which is often simplified or compromised by the need to minimize the reconstruction time. Therefore, much effort has been spent in designing fast projection techniques for reconstruction based on cubic voxels [74, 75]. There remains a need for methods that combine the speed of the fast-projection techniques with more accurate modeling. This is particularly true for DBT, where the data acquisition is inherently incomplete and the breast is under-sampled.

Conventional reconstruction methods generate breast representations that are comprised of volume elements or voxels that are generally cubic or rectangular prisms arranged on a regular Cartesian lattice. These choices, although they simplify the analysis and are computationally efficient, allow only a crude approximation of the object according to the principles of sampling theory. As an alternative, smooth 3D, spherically-symmetric volume elements known as "blobs" are proposed [99]. Blobs, like cubic voxels, are centred on a regular Cartesian grid in 3D. Unlike the contiguous cubes or prisms, however blobs overlap and have a bell-shaped weighting profile whose value tapers smoothly from unity at the centre of the blob in the radial direction to nil at the surface of the spherical "blob".

In this section, the application of smooth blob volume elements for a ray-tracing reconstruction algorithm was described, and a projection matrix was introduced. The improvements achieved in both computational speed and image fidelity was evaluated, comparing to the use of cubic voxels.

5.4.1 Breast Volume Representation by Blobs

Reconstruction in DBT yields a discrete approximation of the (continuous) distribution of breast attenuation on a grid. Image values at intermediate locations (*i.e.*, between the grid points) can be obtained by interpolation. The interpolation process consists of a convolution operation which appropriately weights and shifts copies of a voxel. Therefore, using blobs, in principle a continuous description of the object could be restored by performing these interpolations everywhere in the volume, from the finite set of stored image data. Following the approach of Lewitt [99] and Galigekere [100], a blob-based representation of image reconstruction for DBT was presented.

Let $\mathbf{Q} = (x, y, z)^T$ be the point in the object having components x, y and z along the orthogonal X-, Y- and Z-axes. The reconstruction volume $\mathbf{V}$ is a Cartesian lattice specified in terms of a reference point $\mathbf{Q}_0$ and a transposed array of index vectors $\mathbf{J} = (i, j, k)^T$ (all vectors are column vectors). Δx, Δy and Δz describe the grid resolution in the three directions, respectively. In a Cartesian grid $\mathbf{G}$, the 3D coordinates of a grid-point $\mathbf{J}$ in $\mathbf{V}$ can be expressed as vector:

$$\mathbf{G}(\mathbf{J}) = \mathbf{G}_0 + (i\Delta x, j\Delta y, k\Delta z)^T. \tag{5.2}$$

The image representation denoted by $\bar{f}$ at an arbitrary position Q within the volume is constructed as the superposition of scaled and shifted copies of the local basis function b, as follows:

$$\bar{f}(\mathbf{Q}) = \sum_J c(\mathbf{J}) b\big(\mathbf{Q} - \mathbf{G}(\mathbf{J})\big). \tag{5.3}$$

For rotational symmetric basis functions (blobs):

$$b\big(\mathbf{Q} - \mathbf{G}(\mathbf{J})\big) = b(\|\mathbf{Q} - \mathbf{G}(\mathbf{J})\|), \tag{5.4}$$

where $\|\mathbf{Q}\| = \sqrt{x^2 + y^2 + z^2}$ denotes the distance of $\mathbf{Q}$ from the origin. The general Kaiser-Bessel function is defined in the spatial domain as follows:

$$b^{(m,\alpha)}(r) = \begin{cases} \frac{1}{I_m(\alpha)} \Big(\sqrt{1-(r/a)^2}\Big)^m I_m\Big(\alpha\sqrt{1-(r/a)^2}\Big) & \text{for } 0 \le r \le a, \\ 0 & \text{otherwise.} \end{cases} \tag{5.5}$$

where a is the extent of the blob (set as 2.0), r is the distance from the centre of the blob, and α is the "taper" parameter (a property of the bell-shaped weighting profile) which should be 10.40 to obtain a high quality low-pass filter performance in the frequency domain of the basis function [98]). The function, $I_m(\cdot)$, is the modified Bessel function of the first kind with order m (set $m = 2$ to provide a continuous derivative within the blob and at the border [98]).

5.4.2 Projection Matrix

Regardless of the geometry that is chosen for image acquisition in DBT (*e.g.*, isocentric, partial isocentric or parallel), the image acquisition can be represented (in the homogeneous coordinate system) by a sequence of matrix operations. Following the rigid transformation of gantry and/or detector, the perspective view associated with each angle can be described by a single projection matrix $\mathbf{P}$. The matrix $\mathbf{P}$ can be either estimated by imaging a calibration phantom or constructed from direct specification of the acquisition geometry. We used the following geometry in our simulations: the x-ray source-to-image distance (SID) is 63 cm, and the centre of rotation is 2 cm above the detector. The detector remains stationary while the x-ray tube rotates around the pivot, and θ is the rotation angle of the x-ray tube, with zero defined as the perpendicular position of the tube with respect to the detector. The projection matrix can be calculated as:

$$\mathbf{P} = \begin{pmatrix} \mathrm{SID} & 0 & u_0 \\ 0 & \mathrm{SID} & v_0 \\ 0 & 0 & 1 \end{pmatrix} \begin{pmatrix} 1 & 0 & 0 & -\mathrm{SOD}\sin\theta \\ 0 & 1 & 0 & 0 \\ 0 & 0 & -1 & \mathrm{SOD}\cos\theta \end{pmatrix}, \tag{5.6}$$

where (u_0, v_0) are the coordinates of the perpendicular projection point of the source over the detector plane, and source-to-object distance (SOD) is the source to pivot distance. Deviations from ideal geometry can be incorporated through suitable transformation matrix applied to $\mathbf{P}$. Thus, the projection of an arbitrary grid-point $\mathbf{G}(\mathbf{J})$ in the volume to be reconstructed $\mathbf{V}$ can be computed by matrix multiplication. Several algorithms have been proposed for voxel-driven projection (VDP), based on the efficiency of matrix multiplication with $\mathbf{P}$ [100]. However, as commonly implemented, the quality of ray-driven projection (RDP) is superior to that of the VDP, especially in the case of perspective view or non-isotropic volume elements used in tomosynthesis. Here, we demonstrate the use of matrix $\mathbf{P}$ in ray-driven projection (Figure 5.6a).

5.4.3 Fast Ray Tracing Algorithm

The x-ray passing through source point $\mathbf{S} = (S_x, S_y, S_z)^T$ has a unit direction vector $\mathbf{U} = (U_x, U_y, U_z)^T$ which is determined by the destination detector element. The equation of the x-ray is specified as: $\mathbf{Q}(t) = \mathbf{S} + \mathbf{U}t$. It is possible to extract source position $\mathbf{S}$ and ray direction $\mathbf{U}$ from $\mathbf{P}$ without matrix decomposition or any explicit knowledge of the detector pixel coordinates [100]. The two most important parts in ray-driven projection (RDP) are finding the interception points of the x-ray path with the volume of interest and computing the ray-sum. First, we must choose the most efficient dimension for ray tracing, and this is usually the dimension which has the maximum absolute value in $\mathbf{U}$ components, *i.e.*, $\max(|U_x|, |U_y|, |U_z|)$. For illustration we consider the Z-axis; similar equations apply to other directions.

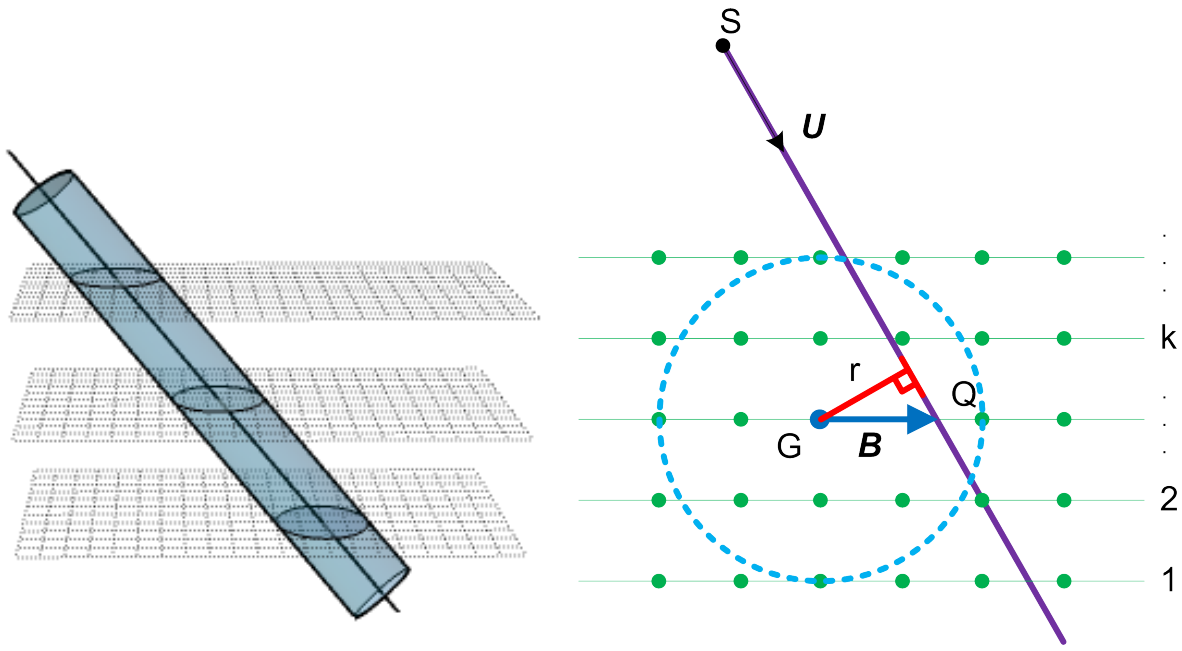

(a) (b)

Figure 5.6: (a) Ray tracing with computation of distances from the x-ray to centres of blobs encountered in transit determine the active region of neighboring grid points. (b) Distance from an x-ray to the centre of a blob on any grid lattice.

The points intercepted with each (k^{th}) grid plane along the chosen direction can be determined by:

$$\mathbf{Q}(t_k) = \mathbf{S} + \mathbf{U}t_k = \begin{pmatrix} S_x + U_x(G_{0z} - S_z + k\Delta z)/U_z \\ S_y + U_y(G_{0z} - S_z + k\Delta z)/U_z \\ G_{0z} - S_z + k\Delta z \end{pmatrix}. \tag{5.7}$$

The square distance from any grid point on the k^{th} plane to the x-ray therefore can be expressed as $r^2 = \|(\mathbf{Q}(t_k) - \mathbf{G}(\mathbf{J})) \times \mathbf{U}\|^2$, as shown in Figure 5.6b, which expands to simpler formula compared to other general ray-tracing algorithms [101]. Let $\mathbf{B} = \mathbf{Q}(t_k) - \mathbf{G}(\mathbf{J})$,

$$\mathbf{B} = \mathbf{Q}(t_k) - \mathbf{G}(\mathbf{J}) = \begin{pmatrix} S_x - G_{0x} + \frac{(G_{0z} - S_z)U_x}{U_z} + \frac{k\Delta z U_x}{U_z} - i\Delta x \\ S_y - G_{0y} + \frac{(G_{0z} - S_z)U_y}{U_z} + \frac{k\Delta z U_y}{U_z} - i\Delta y \\ 0 \end{pmatrix}. \tag{5.8}$$

Because the third component of $\mathbf{B}$ in the above Equation 5.8 equals zero, the time required to compute the square distance is reduced by one-third. Furthermore, other two components of $\mathbf{B}$ are comprised of a constant part and an incremental part when moving from one grid position to next along the chosen direction.

The acquisition of data for digital breast tomosynthesis (DBT) was simulated for a partial isocentric geometry. The detector was stationary while the x-ray tube rotated around a pivot point. Eleven (11) projections were taken at different angles from $-20°$ to $20°$, with $4°$ increments, using monoenergetic (20 keV) x-rays. Two mathematical phantoms were created representing the compressed breast, Phantom

A and Phantom B. Phantom A has a uniform distribution of 50% fibroglandular and 50% adipose tissue as background. Although Phantom A provides a good model of the artifacts inherent in DBT, its uniform background is an oversimplification of the complex detection task in clinical breast screening and diagnosis. Anatomic structures in the normal breast, particularly in the dense breast (which contains a high proportion of fibroglandular tissue), present a "cluttered" background which may confound image interpretation. Phantom B was designed based on volumetric tissue attenuation data obtained from a clinical breast tomosynthesis examination and, therefore, has a depth-dependent structure. Both mathematical phantoms are rectangular prisms in shape and each contains a simulated small tumour (4 mm $\times$ 4 mm $\times$ 2 mm) at the centre. The attenuation coefficients of the simulated tumour are equivalent to those measured for infiltrating ductal carcinoma (IDC) [11].

An iterative reconstruction method, simultaneous algebraic reconstruction technique (SART) has been implemented in Matlab and C++ to evaluate the performance of reconstruction algorithms which use blob voxels. The conventional cubic voxel reconstructions are also used to compare the resulting image quality.

5.4.4 Results of Reconstruction by Blob-based Voxels

For the uniform phantom (Phantom A), reconstructions based on cubic and blob voxels resulted in almost exactly the same image slices, except that the blob-voxel reconstruction tended to show more artifacts near the edge of the phantom if the boundary geometry is not correctly specified in the configuration.

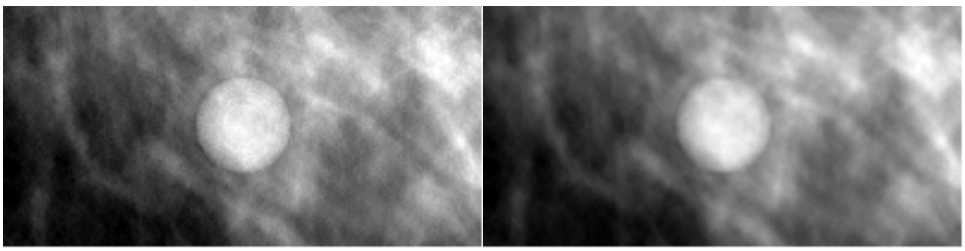

(a) (b)

Figure 5.7: The central slice of the tumour after two iterations of SART reconstruction for Phantom B, shown in X-Y plane, in comparison of two different voxel types: (a) regular cubic voxels, (b) spherical blob voxels.

The central slices of the reconstructed volumes of Phantom B were compared between cubic and blob RDP methods, in the neighborhood of the simulated tumour as shown in Figure 5.7. The two images are displayed with the same grayscale window and centred at the same level. The blob-voxel reconstruction resulted in a less noisy but more blurry image compared to the cubic voxels. The cubic-voxel reconstruction is noisier and has more intensity fluctuations in the background tissue and the tumour, which introduce some ring-like artifacts in the tumour area. This is also demonstrated in the profile through the centre of the tumour for Phantom B, as shown in Figure 5.8.

With respect to the speed of the reconstruction algorithm, it has been observed that the computation time using blobs as voxel elements is comparable to that achieved using cubic voxels, when fast ray-tracing techniques are not applied in both cases. With the projection matrix based ray-tracing, we achieved enhancement in speed by factors of 6.5, and 4 for projection simulations and reconstruction respectively for blob-voxels.

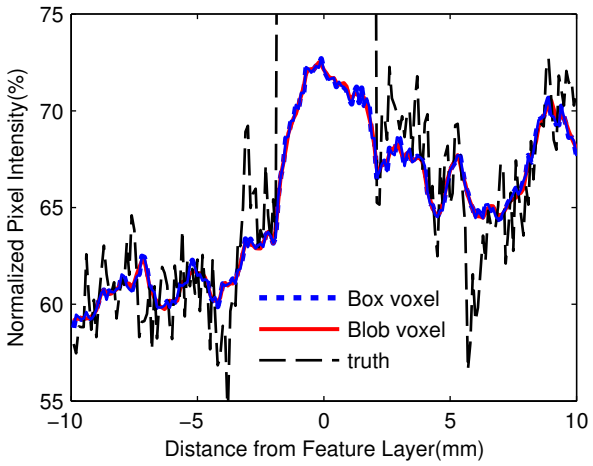

Figure 5.8: Profiles through the centre of the tumour for Phantom B. Dotted line corresponds to cubic voxel and the bold line correspond to blob-voxel. Dash line represents the truth value in the phantom.

The speed of the algorithm is determined by the number of volume elements that are traversed by the ray. When higher accuracy is desired, the size of detector elements must be reduced or the overlapping of the blobs increased and this increases computation time. As shown by Popescu *et. al.* [101], computational speed measured as a function of the number of volume elements traversed per unit time is comparable when ray tracing is performed using blobs or cubic voxels.

Using blobs on a regular grid enables a convenient and flexible model of the forward and backprojection in DBT. The smoother, continuous representation of the sampled signal may yield a more accurate result but this is the subject of future work. Ray-tracing procedures based on the method described here have been implemented and tested, demonstrating flexibility for iterative image reconstruction for DBT. Evaluation of image quality (*e.g.*, edge artifacts and the spread of intensity profiles in a region of interest (*e.g.*, tumour) will be addressed in further study comparing the performance of blobs and cubic voxels.

Bibliography

[1] E. D. Pisano, C. Gatsonis, E. Hendrick, M. Yaffe, J. K. Baum, S. Acharyya, E. F. Conant, L. L. Fajardo, L. Bassett, C. D'Orsi, *et al.*, "Diagnostic performance of digital versus film mammography for breast-cancer screening," *New England Journal of Medicine*, vol. 353, no. 17, pp. 1773–1783, 2005. 3

[2] R. Siegel, D. Naishadham, and A. Jemal, "Cancer statistics, 2013," *CA: A Cancer Journal for Clinicians*, vol. 63, no. 1, pp. 11–30, 2013. 4

[3] C. C. S. S. C. on Cancer Statistics, "Canadian cancer statistics 2012," tech. rep., Canadian Cancer Society, Toronto ON., May 2012. 4

[4] N. Howlader, A. Noone, M. Krapcho, N. Neyman, *et al.*, "Seer cancer statistics review, 1975-2009 (vintage 2009 populations), national cancer institute. bethesda, md," April 2012. 4

[5] D. L. Page, W. D. Dupont, L. W. Rogers, R. A. Jensen, and P. A. Schuyler, "Continued local recurrence of carcinoma 15–25 years after a diagnosis of low grade ductal carcinoma in situ of the breast treated only by biopsy," *Cancer*, vol. 76, no. 7, pp. 1197–1200, 1995. 4

[6] C. Schairer, P. J. Mink, L. Carroll, and S. S. Devesa, "Probabilities of death from breast cancer and other causes among female breast cancer patients," *Journal of the National Cancer Institute*, vol. 96, no. 17, pp. 1311–1321, 2004. 4

[7] I. Khalkhali and H. I. Vargas, "The role of nuclear medicine in breast cancer detection: functional breast imaging," *Radiologic Clinics of North America*, vol. 39, no. 5, pp. 1053–1068, 2001. 4

[8] L. Tabar, M.-F. Yen, B. Vitak, H. Chen, R. A. Smith, S. W. Duffy, *et al.*, "Mammography service screening and mortality in breast cancer patients: 20-year follow-up before and after introduction of screening," *Lancet*, vol. 361, no. 9367, p. 1405, 2003. 4

[9] L. L. Humphrey, M. Helfand, B. K. Chan, and S. H. Woolf, "Breast cancer screening: summary of the evidence," *Ann Intern Med*, vol. 137, no. 5 part 1, pp. 347–360, 2002. 4

[10] L. Tabár, B. Vitak, H.-H. T. Chen, M.-F. Yen, S. W. Duffy, and R. A. Smith, "Beyond randomized controlled trials," *Cancer*, vol. 91, no. 9, pp. 1724–1731, 2001. 4

[11] P. Johns and M. Yaffe, "X-ray characterisation of normal and neoplastic breast tissues," *Physics in medicine and biology*, vol. 32, no. 6, p. 675, 1987. 5, 33, 52, 71

[12] N. Boyd, J. Byng, R. Jong, E. Fishell, L. Little, A. Miller, G. Lockwood, D. Tritchler, and M. J. Yaffe, "Quantitative classification of mammographic densities and breast cancer risk: results from the canadian national breast screening study," *Journal of the National Cancer Institute*, vol. 87, no. 9, pp. 670–675, 1995. 5

[13] J. N. Wolfe, "Risk for breast cancer development determined by mammographic parenchymal pattern," *Cancer*, vol. 37, no. 5, pp. 2486–2492, 1976. 5

[14] G. T. Barnes, "Mammography imaging physics: x-ray equipment considerations," *RSNA Categorical course in breast imaging*, vol. 1999, pp. 41–57, 1999. 6

[15] E. Pisano and M. Yaffe, "Digital mammography," *Radiology*, vol. 234, no. 2, p. 353, 2005. 6

[16] R. Schulz-Wendtland, M. Fuchsjäger, T. Wacker, and K.-P. Hermann, "Digital mammography: an update," *European journal of radiology*, vol. 72, no. 2, pp. 258–265, 2009. 6

[17] J. T. Dobbins III and D. J. Godfrey, "Digital x-ray tomosynthesis: current state of the art and clinical potential," *Physics in medicine and biology*, vol. 48, no. 19, p. R65, 2003. 6, 7, 32

[18] T. Mertelmeier, J. Orman, W. Haerer, and M. K. Dudam, "Optimizing filtered backprojection reconstruction for a breast tomosynthesis prototype device," in *Proc. SPIE, Medical Imaging*, p. 61420F, International Society for Optics and Photonics, 2006. 8

[19] J. Zhou, B. Zhao, and W. Zhao, "A computer simulation platform for the optimization of a breast tomosynthesis system," *Medical Physics*, vol. 34, pp. 1098–1109, 2007. 8

[20] B. Zhao and W. Zhao, "Three-dimensional linear system analysis for breast tomosynthesis," *Medical Physics*, vol. 35, pp. 5219–5232, 2008. 8, 32

[21] B. Zhao, J. Zhou, Y.-H. Hu, T. Mertelmeier, J. Ludwig, and W. Zhao, "Experimental validation of a three-dimensional linear system model for breast tomosynthesis," *Medical Physics*, vol. 36, pp. 240–251, 2009. 8

[22] X. Wang, J. G. Mainprize, G. Wu, and M. J. Yaffe, "Task-based evaluation of image quality of filtered back projection for breast tomosynthesis," in *Proc. 10th International Workshop on Digital Mammography*, pp. 106–113, Springer, 2010. 8

[23] X. Wang, J. G. Mainprize, G. Wu, and M. J. Yaffe, "Wiener filter for filtered back projection in digital breast tomosynthesis," in *SPIE Medical Imaging*, p. 83134Z, International Society for Optics and Photonics, 2012. 8

[24] R. Gordon, R. Bender, and G. T. Herman, "Algebraic reconstruction techniques (art) for three-dimensional electron microscopy and x-ray photography," *Journal of Theoretical Biology*, vol. 29, no. 3, pp. 471–481, 1970. 8

[25] P. Gilbert, "Iterative methods for the three-dimensional reconstruction of an object from projections," *Journal of Theoretical Biology*, vol. 36, no. 1, pp. 105–117, 1972. 8

[26] A. Andersen and A. Kak, "Simultaneous algebraic reconstruction technique (sart): a superior implementation of the art algorithm," *Ultrasonic imaging*, vol. 6, no. 1, pp. 81–94, 1984. 8, 35

[27] Y. Lu, H.-P. Chan, J. Wei, and L. M. Hadjiiski, "Selective-diffusion regularization for enhancement of microcalcifications in digital breast tomosynthesis reconstruction," *Medical physics*, vol. 37, pp. 6003–6014, 2010. 8

[28] Y. Lu, H.-P. Chan, J. Wei, L. Hadjiiski, and C. Zhou, "Multiscale regularized reconstruction for enhancing microcalcification in digital breast tomosynthesis," in *SPIE Medical Imaging*, pp. 831322–831329, International Society for Optics and Photonics, 2012. 8

[29] L. A. Shepp and Y. Vardi, "Maximum likelihood reconstruction for emission tomography," *Medical Imaging, IEEE Transactions on*, vol. 1, no. 2, pp. 113–122, 1982. 8

[30] K. Lange, R. Carson, *et al.*, "Em reconstruction algorithms for emission and transmission tomography," *J. Comput. Assist. Tomogr*, vol. 8, no. 2, pp. 306–316, 1984. 8

[31] K. Lange and J. A. Fessler, "Globally convergent algorithms for maximum a posteriori transmission tomography," *Image Processing, IEEE Transactions on*, vol. 4, no. 10, pp. 1430–1438, 1995. 8, 36, 37, 49

[32] T. Wu, A. Stewart, M. Stanton, T. McCauley, W. Phillips, D. B. Kopans, R. H. Moore, J. W. Eberhard, B. Opsahl-Ong, L. Niklason, *et al.*, "Tomographic mammography using a limited number of low-dose cone-beam projection images," *Medical physics*, vol. 30, pp. 365–380, 2003. 8

[33] T. Wu, J. Zhang, R. Moore, E. Rafferty, D. Kopans, W. Meleis, and D. Kaeli, "Digital tomosynthesis mammography using a parallel maximum-likelihood reconstruction method," in *Proceedings of SPIE*, vol. 5368, pp. 1–11, 2004. 8

[34] I. Goddard, T. Wu, S. Thieret, A. Berman, and H. Bartsch, "Implementing an iterative reconstruction algorithm for digital breast tomosynthesis on graphics processing hardware," in *Proceedings of SPIE*, vol. 6142, pp. 61424V–61427V, 2006. 8

[35] M. Chesters, "Perception and evaluation of images," *Scientific basis of medical imaging*, pp. 237–280, 1982. 9

[36] A. E. Burgess, F. L. Jacobson, and P. F. Judy, "Human observer detection experiments with mammograms and power-law noise," *Medical physics*, vol. 28, pp. 419–437, 2001. 10, 20, 30, 33

[37] J. Siewerdsen, I. Cunningham, and D. Jaffray, "A framework for noise-power spectrum analysis of multidimensional images," *Medical physics*, vol. 29, pp. 2655–2671, 2002. 10, 13, 15

[38] G. Gang, D. Tward, J. Lee, and J. Siewerdsen, "Anatomical background and generalized detectability in tomosynthesis and cone-beam ct," *Medical physics*, vol. 37, p. 1948, 2010. 10, 13, 39

[39] P. Sharp *et al.*, "Icru report 54 international commission on radiation unit," *Medical ImagingThe Assessment of Image Quality*, p. 15, 1995. 11

[40] G. Wu, J. G. Mainprize, and M. J. Yaffe, "Spectral analysis of mammographic images using a multitaper method," *Medical Physics*, vol. 39, pp. 801–810, 2012. 13, 33, 39, 54, 55, 61, 63, 65

[41] G. J. Gang, J. Lee, J. W. Stayman, D. J. Tward, W. Zbijewski, J. L. Prince, and J. H. Siewerdsen, "Analysis of fourier-domain task-based detectability index in tomosynthesis and cone-beam ct in relation to human observer performance," *Medical Physics*, vol. 38, pp. 1754–1768, 2011. 14

[42] Y. Bard, *Nonlinear parameter estimation*, vol. 477. Academic Press New York, 1974. 14

[43] D. B. Percival and A. T. Walden, *Spectral analysis for physical applications*. Cambridge University Press, 1993. 14, 16

[44] D. J. Thomson, "Spectrum estimation and harmonic analysis," *Proceedings of the IEEE*, vol. 70, no. 9, pp. 1055–1096, 1982. 14, 16, 61

[45] M. Daquah and I. Zabalawi, "An almost noise-free power estimation method in maximum entropy spectral analysis," *Eng. Sci*, vol. 5, pp. 45–59, 1993. 14

[46] J. P. Burg, *Maximum entropy spectral analysis*. PhD thesis, Stanford University, 1975. 14

[47] A. T. Walden, D. B. Percival, and E. J. McCoy, "Spectrum estimation by wavelet thresholding of multitaper estimators," *Signal Processing, IEEE Transactions on*, vol. 46, no. 12, pp. 3153–3165, 1998. 14

[48] M. K. van Vugt, P. B. Sederberg, and M. J. Kahana, "Comparison of spectral analysis methods for characterizing brain oscillations," *Journal of neuroscience methods*, vol. 162, no. 1, pp. 49–63, 2007. 14, 30

[49] K. S. Riedel, A. Sidorenko, and D. J. Thomson, "Spectral estimation of plasma fluctuations. i. comparison of methods," *Physics of plasmas*, vol. 1, pp. 485–500, 1994. 14, 16

[50] J. Park, C. R. Lindberg, and F. L. Vernon, "Multitaper spectral analysis of high-frequency seismograms," *Journal of Geophysical Research: Solid Earth (1978–2012)*, vol. 92, no. B12, pp. 12675–12684, 1987. 14

[51] J. T. Serences, "A comparison of methods for characterizing the event-related bold timeseries in rapid fmri," *Neuroimage*, vol. 21, no. 4, pp. 1690–1700, 2004. 14

[52] M. A. Wieczorek and F. J. Simons, "Minimum-variance multitaper spectral estimation on the sphere," *Journal of Fourier Analysis and Applications*, vol. 13, no. 6, pp. 665–692, 2007. 14

[53] A. T. Walden, E. McCoy, and D. B. Percival, "The variance of multitaper spectrum estimates for real gaussian processes," *Signal Processing, IEEE Transactions on*, vol. 42, no. 2, pp. 479–482, 1994. 14

[54] E. J. McCoy, A. T. Walden, and D. B. Percival, "Multitaper spectral estimation of power law processes," *Signal Processing, IEEE Transactions on*, vol. 46, no. 3, pp. 655–668, 1998. 14

[55] E. Samei, N. T. Ranger, J. T. Dobbins III, and Y. Chen, "Intercomparison of methods for image quality characterization. i. modulation transfer function," *Medical physics*, vol. 33, pp. 1454–1475, 2006. 15

[56] I. E. Commission *et al.*, "Medical electrical equipment: characteristics of digital x-ray imaging devicespart 1: determination of the detective quantum efficiency," *International Standard IEC62220-1, Geneva*, 2003. 15

[57] D. Slepian, "Prolate spheroidal wave functions, fourier analysis, and uncertainty. v-the discrete case," *AT T Technical Journal*, vol. 57, pp. 1371–1430, 1978. 16

[58] K. S. Riedel and A. Sidorenko, "Minimum bias multiple taper spectral estimation," *Signal Processing, IEEE Transactions on*, vol. 43, no. 1, pp. 188–195, 1995. 16, 18, 30, 62

[59] I. Cunningham, M. Westmore, and A. Fenster, "A spatial-frequency dependent quantum accounting diagram and detective quantum efficiency model of signal and noise propagation in cascaded imaging systems," *Medical physics*, vol. 21, pp. 417–427, 1994. 20

[60] I. Cunningham, J. Yao, and V. Subotic, "Cascaded models and the dqe of flat-panel imagers: noise aliasing, secondary quantum noise and reabsorption," in *Proceedings of SPIE*, vol. 4682, pp. 61–72, 2002. 20

[61] A. E. Burgess, "Mammographic structure: Data preparation and spatial statistics analysis," in *Proc. SPIE*, vol. 3661, pp. 642–653, 1999. 21, 29

[62] O. Alonzo-Proulx, J. G. Mainprize, N. J. Packard, J. M. Boone, A. Al-Mayah, K. Brock, and M. J. Yaffe, "Development of a peripheral thickness estimation method for volumetric breast density measurements in mammography using a 3d finite element breast model," in *Digital Mammography*, pp. 467–473, Springer, 2010. 27

[63] A. E. Burgess, "Visual signal detection with two-component noise: low-pass spectrum effects," *JOSA A*, vol. 16, no. 3, pp. 694–704, 1999. 27

[64] I. Reiser, S. Lee, and R. Nishikawa, "On the orientation of mammographic structure," *Medical Physics Letter*, vol. 38, pp. 5303–5306, 2011. 30

[65] E. Engstrom, I. Reiser, and R. Nishikawa, "Comparison of power spectra for tomosynthesis projections and reconstructed images," *Medical physics*, vol. 36, pp. 1753–1758, 2009. 30

[66] A. E. Burgess, F. L. Jacobson, and P. F. Judy, "On the detection of lesions in mammographic structure," in *Proc. SPIE*, vol. 3663, pp. 304–315, 1999. 30

[67] G. Wu, J. G. Mainprize, and M. J. Yaffe, "Characterization of a constrained paired-view technique in iterative reconstruction for breast tomosynthesis," *Medical Physics*, vol. 40, pp. 101901–1–12, 2013. 31

[68] T. Wu, R. H. Moore, E. A. Rafferty, and D. B. Kopans, "A comparison of reconstruction algorithms for breast tomosynthesis," *Medical physics*, vol. 31, pp. 2636–2647, 2004. 32, 35, 36, 40, 67

[69] Y. Zhang, H.-P. Chan, B. Sahiner, J. Wei, M. M. Goodsitt, L. M. Hadjiiski, J. Ge, and C. Zhou, "A comparative study of limited-angle cone-beam reconstruction methods for breast tomosynthesis," *Medical physics*, vol. 33, pp. 3781–3795, 2006. 32

[70] G. T. Herman and L. B. Meyer, "Algebraic reconstruction techniques can be made computationally efficient [positron emission tomography application]," *Medical Imaging, IEEE Transactions on*, vol. 12, no. 3, pp. 600–609, 1993. 32

[71] H. Guan and R. Gordon, "A projection access order for speedy convergence of art (algebraic reconstruction technique): a multilevel scheme for computed tomography," *Physics in medicine and biology*, vol. 39, no. 11, pp. 2005–2022, 1994. 32

[72] H. Guan, R. Gordon, and Y. Zhu, "Combining various projection access schemes with the algebraic reconstruction technique for low-contrast detection in computed tomography," *Physics in medicine and biology*, vol. 43, no. 8, p. 2413, 1998. 32

[73] G. Wu, J. Mainprize, and M. Yaffe, "Characterization of projection ordering in iterative reconstruction methods for breast tomosynthesis," in *Digital Mammography*, pp. 601–605, Springer, 2008. 32

[74] R. L. Siddon, "Fast calculation of the exact radiological path for a three-dimensional ct array," *Medical physics*, vol. 12, pp. 252–255, 1985. 33, 67

[75] F. Jacobs, E. Sundermann, B. De Sutter, M. Christiaens, and I. Lemahieu, "A fast algorithm to calculate the exact radiological path through a pixel or voxel space," *Journal of computing and information technology*, vol. 6, no. 1, pp. 89–94, 1998. 33, 67

[76] J. M. Boone, "Normalized glandular dose (dgn) coefficients for arbitrary x-ray spectra in mammography: Computer-fit values of monte carlo derived data," *Medical physics*, vol. 29, pp. 869–875, 2002. 33

[77] I. Reiser and R. Nishikawa, "Task-based assessment of breast tomosynthesis: Effect of acquisition parameters and quantum noise," *Medical physics*, vol. 37, p. 1591, 2010. 33, 34

[78] I. Sechopoulos and C. Ghetti, "Optimization of the acquisition geometry in digital tomosynthesis of the breast," *Medical physics*, vol. 36, p. 1199, 2009. 33

[79] G. Wu, J. G. Mainprize, and M. J. Yaffe, "Breast tomosynthesis reconstruction using a grid of blobs with projection matrices," in *Digital Mammography*, pp. 243–250, Springer, 2010. 35

[80] K. Mueller, R. Yagel, and J. J. Wheller, "Anti-aliased three-dimensional cone-beam reconstruction of low-contrast objects with algebraic methods," *Medical Imaging, IEEE Transactions on*, vol. 18, no. 6, pp. 519–537, 1999. 35, 36

[81] A. H. Andersen, "Algebraic reconstruction in ct from limited views," *Medical Imaging, IEEE Transactions on*, vol. 8, no. 1, pp. 50–55, 1989. 36

[82] T. Wu, R. H. Moore, and D. B. Kopans, "Voting strategy for artifact reduction in digital breast tomosynthesis," *Medical physics*, vol. 33, pp. 2461–71, 2006. 36, 37

[83] S. Abdurahman, A. Jerebko, T. Mertelmeier, T. Lasser, and N. Navab, "Out-of-plane artifact reduction in tomosynthesis based on regression modeling and outlier detection," in *Breast Imaging*, pp. 729–736, Springer, 2012. 37

[84] H. M. Hudson and R. S. Larkin, "Accelerated image reconstruction using ordered subsets of projection data," *Medical Imaging, IEEE Transactions on*, vol. 13, no. 4, pp. 601–609, 1994. 37

[85] M. Jiang and G. Wang, "Convergence studies on iterative algorithms for image reconstruction," *Medical Imaging, IEEE Transactions on*, vol. 22, no. 5, pp. 569–579, 2003. 37, 49

[86] K. Lange, "Convergence of em image reconstruction algorithms with gibbs smoothing," *Medical Imaging, IEEE Transactions on*, vol. 9, no. 4, pp. 439–446, 1990. 37, 49

[87] A. E. Burgess, "The rose model, revisited," *JOSA A*, vol. 16, no. 3, pp. 633–646, 1999. 39

[88] A. E. Burgess, F. L. Jacobson, and P. F. Judy, "Lesion detection in digital mammograms," in *Proc. SPIE, Medical Imaging 2001*, pp. 555–560, International Society for Optics and Photonics, 2001. 39

[89] A. D. Maidment, R. Fahrig, and M. J. Yaffe, "Dynamic range requirements in digital mammography," *Medical physics*, vol. 20, p. 1621, 1993. 39

[90] S. Richard and J. H. Siewerdsen, "Comparison of model and human observer performance for detection and discrimination tasks using dual-energy x-ray images," *Medical physics*, vol. 35, p. 5043, 2008. 39

[91] ICRU, "Medical imaging-the assessment of image quality," Tech. Rep. ICRU Report No. 54, International Commission on Radiation Units and Measurements, Bethesda, MD, 1996. 39

[92] E. Y. Sidky, X. Pan, I. S. Reiser, R. M. Nishikawa, R. H. Moore, and D. B. Kopans, "Enhanced imaging of microcalcifications in digital breast tomosynthesis through improved image-reconstruction algorithms," *Medical physics*, vol. 36, p. 4920, 2009. 50, 51

[93] A. Buades, B. Coll, and J.-M. Morel, "A non-local algorithm for image denoising," in *Computer Vision and Pattern Recognition, CVPR2005. IEEE Computer Society Conference on*, vol. 2, pp. 60–65, IEEE, 2005. 52

[94] M. Elad, "On the origin of the bilateral filter and ways to improve it," *Image Processing, IEEE Transactions on*, vol. 11, no. 10, pp. 1141–1151, 2002. 62

[95] A. Walden, E. McCoy, and D. Percival, "The effective bandwidth of a multitaper spectral estimator," *Biometrika*, vol. 82, no. 1, pp. 201–214, 1995. 62

[96] P. Bloomfield, *Fourier analysis of time series: an introduction*. Wiley-Interscience, 2004. 63

[97] D. Barash, "Fundamental relationship between bilateral filtering, adaptive smoothing, and the nonlinear diffusion equation," *Pattern Analysis and Machine Intelligence, IEEE Transactions on*, vol. 24, no. 6, pp. 844–847, 2002. 63

[98] K. Mueller, R. Yagel, and J. J. Wheller, "Fast implementations of algebraic methods for three-dimensional reconstruction from cone-beam data," *Medical Imaging, IEEE Transactions on*, vol. 18, no. 6, pp. 538–548, 1999. 67, 69

[99] R. M. Lewitt, "Alternatives to voxels for image representation in iterative reconstruction algorithms," *Physics in Medicine and Biology*, vol. 37, no. 3, pp. 705–716, 1992. 68

[100] R. R. Galigekere, K. Wiesent, and D. W. Holdsworth, "Cone-beam reprojection using projection-matrices," *Medical Imaging, IEEE Transactions on*, vol. 22, no. 10, pp. 1202–1214, 2003. 68, 69

[101] L. M. Popescu and R. M. Lewitt, "Ray tracing through a grid of blobs," in *Nuclear Science Symposium Conference Record, 2004 IEEE*, vol. 6, pp. 3983–3986, IEEE, 2004. 70, 72